

COOLANT PASSAGE SEGMENTATION INFLUENCE  
ON REGENERATIVE-COOLING EFFECTIVENESS  
FOR SMALL SPACECRAFT THRUSTERS

By

LUCAS UTLEY

Bachelor of Science in Mechanical & Aerospace

Engineering

Oklahoma State University

Stillwater, OK

2018

Submitted to the Faculty of the  
Graduate College of the  
Oklahoma State University  
in partial fulfillment of  
the requirements for  
the Degree of  
MASTER OF SCIENCE  
May, 2020

COOLANT PASSAGE SEGMENTATION  
INFLUENCE ON REGENERATIVE-COOLING  
EFFECTIVENESS FOR SMALL SPACECRAFT  
THRUSTERS

Thesis Approved:

Kurt Rouser, PhD.

---

Thesis Adviser

Jamey Jacob, PhD.

---

Sandip Harimkar, PhD.

---

## ACKNOWLEDGEMENTS

I would like to thank my committee members: Dr. Kurt Rouser, Dr. Jamey Jacob, and Dr. Sandip Harimkar for their advisement and support in making this thesis possible; I loved the continued opportunity to study rocket propulsion here at OSU. Thank you to my parents for their support throughout my undergraduate and graduate studies, as none of this would have been possible without them. I would like to thank Kylar Moody, Connor McCain, and Nick Foster for their help throughout my experimental design, Chris Huckabay for lending me his laptop on which this thesis was written, and Wendy Hall for her help in printing the nozzles when the university began to close this semester amid COVID19. Finally, I want to thank Samantha Huckabay for her continued support and encouragement during these two years of grad school.

Name: LUCAS UTLEY

Date of Degree: MAY, 2020

Title of Study: COOLANT PASSAGE SEGMENTATION INFLUENCE ON  
REGENERATIVE-COOLING EFFECTIVENESS FOR SMALL  
SPACECRAFT THRUSTERS

Major Field: MECHANICAL AND AEROSPACE ENGINEERING

Abstract: The purpose of this thesis is to examine the effect of varying the number of cooling passages in a regeneratively-cooled rocket combustion chamber and nozzle analog for a small spacecraft thruster producing 22N (5lbf) thrust. Most chemical rocket satellite thrusters are radiation-cooled and utilize toxic monopropellant hydrazine, but the emergence of low-toxicity, higher-performance green propellants is reducing system costs of pre-launch loading procedures. Due to their high water content, green propellants necessitate large on-board power requirements to ignite. Additionally, they burn at elevated flame temperatures compared to conventional hydrazine, requiring more exotic refractory metals to comprise the catalyst bed and thrust chamber for withstanding decomposition temperatures. By utilizing regenerative cooling, not only can the propellants become preheated, thereby reducing ignition power requirements, but the lower thrust chamber temperatures maintained allow for less expensive metal alloys. In this study, additive manufacturing was used for developing the thrust chamber, and atomic diffusion additive manufacturing formed the stainless steel test hardware. Testing involved firing solid propellant rocket motors as a gas generator to replicate elevated-pressure, high-temperature environments characteristic of chemical rocket propulsion systems to understand thermal changes in the coolant flow and nozzle surface temperatures. A single annular cooling passage was segmented by 4, 8, and 12 walls to determine cooling effectiveness for each configuration by measuring water coolant temperature rise and external surface temperature at the nozzle throat. An analytical heat transfer model was also developed to calculate these temperatures and heat flux for comparison to the experimental study. Results indicate that fewer, wider cooling passages were more effective at cooling the thrust chamber, with a single, unsegmented annulus being the most effective for heat transfer to the cooling fluid. A single cooling passage resulted in 55% cooling effectiveness, while 12 segmented passages had just 46%. By integrating few cooling passages in junction with additive manufacturing for small-scale rocket thrust chambers, higher flame temperatures may be sustained, and favorable potential is shown for utilizing non-refractory alloys with green propellants to achieve lower costs for in-space propulsion systems.

## TABLE OF CONTENTS

Chapter	Page
I. INTRODUCTION.....	1
1.1. Motivation.....	1
1.2. Goals and Objectives .....	4
1.3. Thesis Outline .....	5
II. BACKGROUND.....	6
2.1 Overview of Small Spacecraft Propulsion.....	6
2.2. Rocket Propulsion Principals.....	8
2.2.1 Rocket and Nozzle Performance.....	8
2.2.2 Solid Rocket Propellants.....	11
2.3. Thermal Management in Combustion Chambers .....	13
2.4. Heat Transfer Principals .....	15
2.5. Green Propellant Background.....	18
2.6. Current State of Green 22N Thrusters .....	19
2.7. Additive Manufacturing Overview .....	22
III. EXPERIMENTAL STUDY.....	26
3.1. Test Bed Design.....	26
3.1.1. Thruster Benchmarking .....	27
3.1.2. Converging-Diverging Nozzle Geometry.....	29
3.1.3. Motor Integration and Cooling Channel Geometry Design.....	32
3.1.4. Solid Propellant Rocket Motor/Gas Generator .....	39
3.1.5. Test Setup Integration .....	41
3.1.6. Instrumentation .....	42
3.2 Hotfire Testing Procedures .....	46
3.3 Analytical Model .....	47

Chapter	Page
IV. RESULTS .....	51
4.1 Motor Performance .....	51
4.2 Thermal Evaluation.....	53
4.2.1 Leakage Between Nozzle Walls .....	59
4.2.2 Influence of Segmented Cooling Passages .....	61
4.3 Analytical Model Results.....	63
4.4 Summary of Experimental Results .....	69
V. UNCERTAINTY ANALYSIS .....	71
VI. CONCLUSIONS .....	75
6.1 Conclusions from Experimental and Analytical Results .....	75
6.2 Recommendations for Future Work.....	76
REFERENCES .....	78
APPENDICES .....	81

## LIST OF TABLES

Table	Page
1. Summary of common additive manufacturing techniques .....	24
2. Summary of 3D-printed rocket engines in development or production .....	26
3. Exhaust gas comparison of KNSB to liquid monopropellants .....	28
4. 22N Thrusters in development or in production .....	28
5. Gas generator and KNSB grain design quantities.....	30
6. Coolant flow area changes throughout nozzle .....	39
7. Average chamber pressure and standard deviation for 4 firings.....	53
8. Propellant burn time and mass flow rate during motor burn .....	54
9. Summarized thermal data .....	62
10. Heat transfer coefficients at 3 nozzle locations .....	66
11. Overall heat flux at 3 nozzle locations.....	67
12. Analytical model comparison to analytical results .....	70
13. Liquid temperature change and averaged cooling effectiveness .....	70
14. Gas generator repeatability study.....	76

## LIST OF FIGURES

Figure	Page
1. Size comparison of several types of satellites.....	2
2. Regenerative cooling schematic of fluid flow paths.....	4
3. Historical nano/microsatellites launched from 2000 to 2015 .....	7
4. Graphic of nozzle expansion ratio .....	10
5. Nozzle expansion configurations.....	10
6. MR-106L thruster with large bell nozzle for expanding to vacuum conditions .....	11
7. Example solid propellant grain geometries and burn profiles .....	12
8. RS-25 wall heat flux vs axial location .....	13
9. Types of regen jacket channel designs.....	14
10. Heat transfer modes in a regen jacket .....	15
11. Integration of the (5) 1-N GR-1 thrusters to NASA's GPIM satellite .....	19
12. TZM thruster (left) vs iridium thruster (right) used by McGee with AF-M315E .....	21
13. ADAM-printed part with 0.125 layer height .....	25
14. Burn rate behavior for KNSB propellant.....	29
15. MotorSim screenshot of 6 inch-long propellant grain .....	31
16. MotorSim simulation results for thrust and pressure during the 18s burn time.....	32
17. Uncooled converging-diverging nozzle profile .....	33
18. Nozzle cross section with coolant passage .....	34
19. Coolant (blue) and exhaust gas (orange) flow paths.....	35
20. Test part to ensure even coolant inlet flow distribution within the nozzle .....	36
21. Final nozzle design in various orientations.....	36
22. Channel wall dimensions within coolant flow passage cross section.....	37
23. Nozzle configurations at several cross sections.....	38
24. AM considerations for printing internal passages without support material .....	39
25. 3D-printed nozzles from ADAM throughout the processing stages.....	40
26. Components of the assembled gas generator .....	41
27. Gas generator components prior to assembly .....	42
28. Water coolant flow setup prior to motor firing (left) and flow rate validation (right)	43
29. Thermocouples installed onto nozzle for firing .....	44
30. Thrust stand instrumentation and data acquisition components .....	45
31. Thrust stand component schematic and flowchart.....	46



Figure	Page
32. LabVIEW VI interfaces for the thrust stand (left) and thermocouples (right) .....	47
33. Single cooling passage nozzle during firing .....	48
34. Calculated coolant passage geometry cross section at nozzle throat .....	49
35. Analytical model iteration schematic.....	50
36. Combined pressure data for 4 firings.....	53
37. Overall temperature plot – 1 channel.....	55
38. Water behavior after flow shutoff.....	56
39. Overall temperature plot for 4 channels.....	57
40. Overall temperature plot for 8 channels.....	57
41. Overall temperature plot for 12 channels.....	59
42. KNSB residue accumulation (left) and eventual casing burn-through (right).....	60
43. Water leakage through gas flow passage .....	61
44. Air bubble formation through nozzle wall indicating leakage.....	61
45. Analytical spreadsheet model snapshot .....	64
46. Gas convection heat transfer coefficient for 1 passage.....	65
47. Heat flux for 1 passage .....	65
48. Liquid cooling convective heat transfer coefficient for 1 passage .....	66
49. Liquid heat transfer coefficient for all nozzle configurations.....	67
50. Heat flux for various nozzle configurations.....	68
51. Gas generator performance validation test .....	73
52. Instrumented motor assembly for repeatability testing.....	74
53. Thrust data for repeatability study .....	75
54. Chamber pressure data for repeatability study.....	75
55. Temperature data during motor burn - 1 channel .....	87
56. Temperature data during motor burn - 4 channels.....	87
57. Temperature data during motor burn - 8 channels.....	88
58. Temperature data during motor burn - 12 channels.....	88
59. Analytical model - 1 channel part 1 .....	89
60. Analytical model - 1 channel part 2.....	90
61. Analytical model - 1 channel part 3.....	91
62. Analytical model - 4 channels part 1 .....	92
63. Analytical model - 4 channels part 2 .....	93
64. Analytical model - 4 channels part 3 .....	94
65. Analytical model - 8 channels part 1 .....	95
66. Analytical model - 8 channels part 2 .....	96
67. Analytical model - 8 channels part 3 .....	97
68. Analytical model - 12 channels part 1 .....	98
69. Analytical model - 12 channels part 2 .....	99
70. Analytical model - 12 channels part 3 .....	100

## CHAPTER I

### INTRODUCTION

#### 1.1 Motivation

Small spacecraft are satellites and space probes weighing less than 180kg and exist as an alternative to large, expensive spacecraft that takes years to develop by government, military, or communications institutions. They can be developed and launched affordably and quickly in great numbers, enabling the feasibility of satellite constellations orbiting Earth, providing internet access or surveillance with thousands of small spacecrafts offering coverage to the entirety of Earth's surface.

Like their larger counterparts, many small spacecraft require on-board propulsion systems for orbital adjustments, maneuvering, orientation corrections, and deorbit burns at the end of their life to reduce space debris. With the rise of popularity in small spacecraft, additional research is being conducted into propulsion systems on this scale that historically hasn't been as necessary for larger space payloads. Many small spacecraft propulsion systems have emerged including electrothermal, electrostatic, electromagnetic, and chemical propulsion. This study will focus on the small spacecraft application of chemical propulsion which is most often used for launch vehicles or propelling large spacecraft. A comparison of the scales of satellites is shown below in Figure 1.

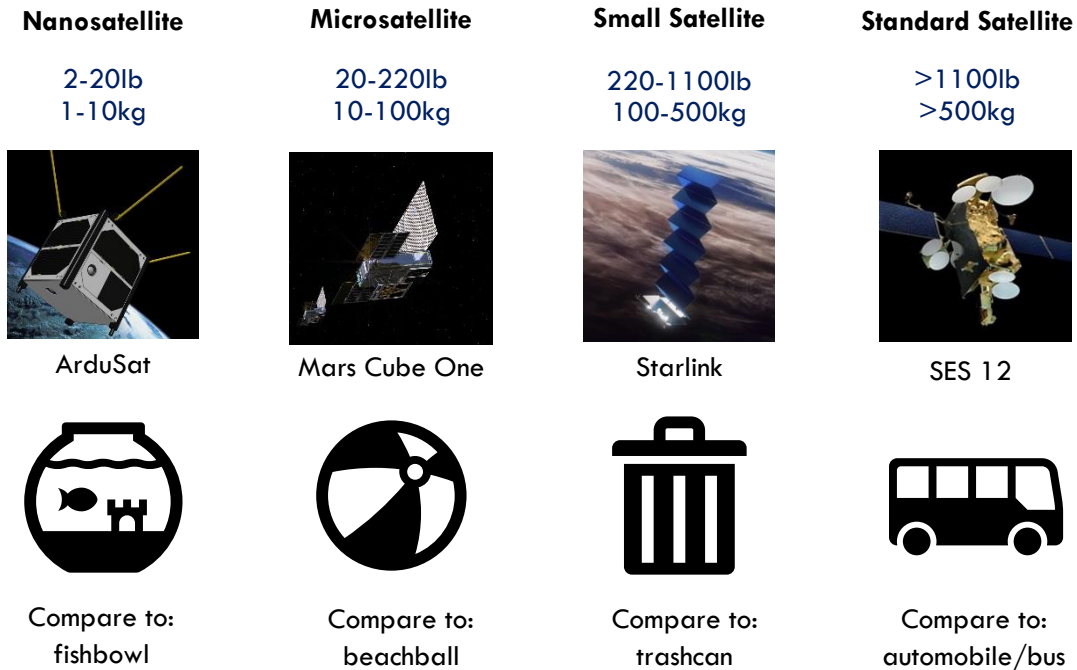


**Figure 1: Size comparison of several types of satellites [1-4]**

Chemical rocket propulsion systems utilize bipropellants or monopropellants that release energy through a combustion or decomposition reaction. Monopropellants are popular for spacecraft propulsion due to their simplicity and weight savings over higher performance bipropellants. Historically, hydrazine has been the primary monopropellant of choice due to its reasonable performance, storability, and frequent use in spacecraft. However, its toxicity complicates preflight propellant loading, making it expensive for primary payloads, and prohibitively impractical for secondary payloads which small spacecraft often are. This is especially true as spaceflight procedures are shifting from government institutions to private organizations [5]. Recently, the introduction of ionic liquid “green” propellants has generated interest as a spacecraft monopropellant for its improved performance over hydrazine, minimal toxicity, and therefore, lower costs during handling and preflight loading. However, as an emerging technology, green propellants are not yet as well understood and feature some design challenges including ignition difficulty due to high water content and higher flame temperatures than hydrazine. The ignition difficulty necessitates large power requirements on-board the

spacecraft, and this is a particularly complex issue for small satellite systems in which electrical power availability is small. Additionally, the already high flame temperatures of decomposing hydrazine require stainless steels or even refractory metal alloys to withstand the heat of decomposition in the thrust chamber. Green propellants have even higher flame temperatures, thus furthering the need for expensive alloys to comprise the thrust chambers.

Cooling satellite thrusters is most often accomplished via radiation cooling in which the heat from the combusting or decomposing propellant is radiated through the metal thrust chamber into the vacuum of space. Special thermal standoff is sometimes required to prevent heat soak back into the spacecraft [6] and special mounting considerations may be necessary to ensure the thrust chamber has sufficient exposure external to the craft to protect payload electronics and structure. Regenerative cooling is another thermal management approach to rocket engines that sees greater use for bipropellant launch vehicle propulsion systems in which the greatest thermal loads exist. The liquid fuel, or oxidizer in some cases, circulates around the chamber through special wall passages, injects into the chamber, and mixes with the other propellant for combustion as shown in Figure 2. The benefit is twofold: adequate cooling of the thrust chamber as well as fuel preheating that improves performance by increasing the exhaust velocity up to 1.5% [7].

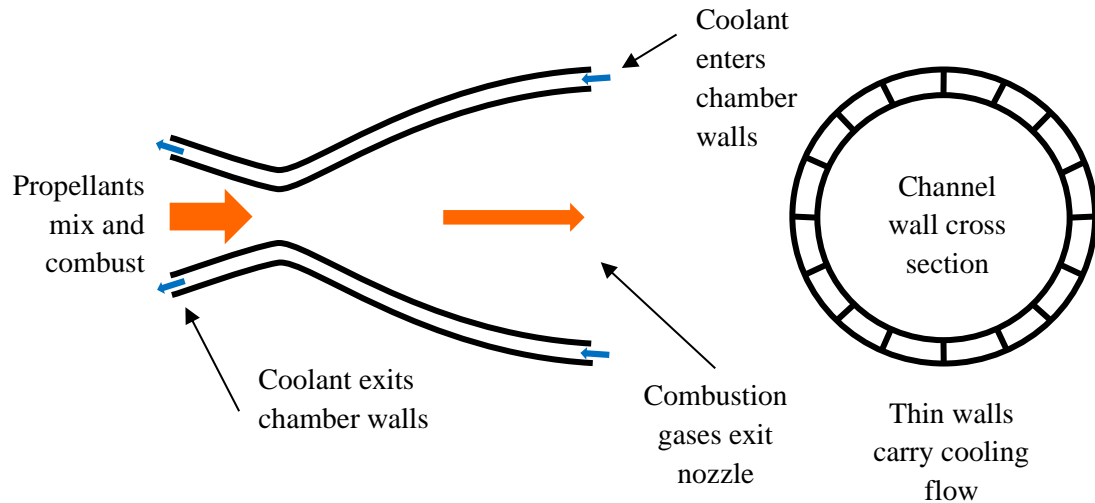


**Figure 2: Regenerative cooling schematic of fluid flow paths**

Traditional regenerative cooling manufacturing techniques become impractical at the scale of small satellite propulsion, and therefore additive manufacturing shows favorable potential for integrating cooling passages directly into the thrust chamber part. Unique shapes are enabled, especially those that utilize intricate internal flow paths which is ideally suited to multi-path flow profiles such as featured in this study. However, additive manufacturing comes with its own design considerations and must be accounted for during development.

In this study, regenerative cooling is proposed as a thermal management technique for green monopropellant thrusters to not only assist with the high flame temperatures encountered in the thrust chamber, but to also reduce power requirements needed for decomposition, as the propellant will become preheated during circulation about the thrust chamber. This thrust chamber geometry will utilize integrated cooling channels as a result of additive manufacturing techniques.

## 1.2 Goals and Objectives

The goal of this work is to study how varying the number of regenerative cooling passages influences cooling effectiveness for small satellite rocket thrust chambers. It will also

determine whether regenerative cooling is feasible for augmenting performance of green monopropellant thrusters by raising the liquid fuel temperature prior to decomposition or combustion. A thrust chamber of similar dimensions to common 22N chemical thrusters will be designed and tested with solid propellant serving as a high-pressure, hot gas generator to evaluate cooling effectiveness. The number of cooling passages is varied from 1-12 to evaluate changes in coolant temperature, and how other heat transfer parameters are affected from segmented flow geometry. With this knowledge, the feasibility of regeneratively-cooling small satellite green propellant thrusters is evaluated as an alternative to radiation-cooled, expensive refractory alloy thrust chambers.

### 1.3 Thesis Outline

Background and relevant literature of past studies on rocket thrust chambers, nozzles, heat transfer, thermal management in rocket engines, additive manufacturing, and green propellants are provided in Chapter 2. Chapter 3 discusses test bed design, experimental procedures, and development of an analytical model to study heat transfer for this design. Chapter 4 provides the thermal data and results of this study along with analysis of results and observations. Uncertainty analysis is described in Chapter 5. Conclusions and recommendations for future work are summarized in Chapter 6.

## CHAPTER II

### BACKGROUND

#### 2.1 Overview of Small Spacecraft Propulsion

Small spacecraft comprise satellites and space probes weighing less than 180kg for civil, government, defense, and commercial applications. They fulfill various purposes from communication and Earth observation to technology development/demonstration and science missions that collect space-based data [8]. The number of nano/microsatellites has largely seen increases year to year as shown in Figure 3. The small satellite market is being further enabled by more launch vehicles tailored to small spacecraft such as Rocket Lab's Electron, LauncherOne by Virgin Orbit, Terran 1 by Relativity, and Firefly Alpha by Firefly Aerospace. These vehicles are will further enable access to space for small payloads, reducing the cost, and improving schedules.

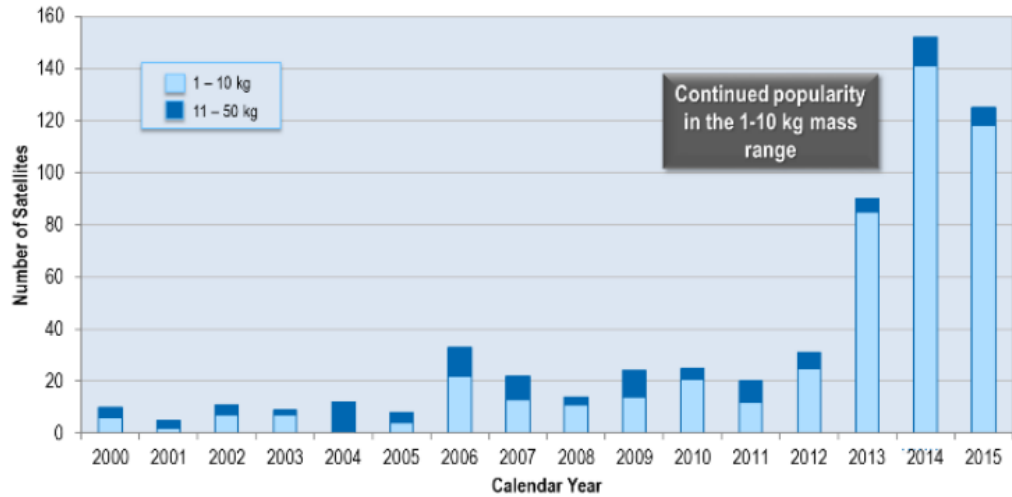


**Figure 3: Historical nano/microsatellites launched from 2000 to 2015 [8]**

Additionally, SpaceX has begun launching Starlink, the first commercial small satellite constellation to provide internet access from LEO, representing as many as 42,000 satellites [9]. While Starlink satellites feature Hall-effect thrusters rather than chemical thrusters as described in this study, other companies such as OneWeb and Amazon are also developing similar constellations [10] that represent the increased potential for small-scale chemical propulsion.

Wong et al. of Arizona State University and Air Force Research Laboratory identified several current issues with chemical micropropulsion including propellant compatibility with thruster hardware, exhaust contamination of the satellite, and manufacturing and integration complexity [11]. Leakage of microvalves and passage clogging were also identified as considerations for their microsatellite propulsion testbed. Such factors are similarly prevalent in this study, especially passage clogging of microchannels and small flow areas.

For micro, nano, and picosatellites, micro-electromechanical system (MEMS) technology is being studied for developing ultra-small propulsion systems. Schilling et al. considered various micropropulsion systems including chemical, electromagnetic, and electrostatic for the TechSat21 formation-flying satellite system. At the smallest end of chemical propulsion, MEMS is an enabling technology that “uses semiconductor manufacturing techniques to etch thousands of



extremely small ( $\sim 500\mu\text{m}$ ) nozzles and cavities into a silicon wafer” and can be scaled to small sizes at the expense of specific impulse and propellant mass fraction [12]. The author’s survey study ultimately identified a hydrazine monopropellant thruster and a pulsed plasma thruster as most suitable for their demonstration mission due to technological readiness and availability for their 2003 launch. MEMS was not necessary for their scale and hadn’t reached a demonstrated technological readiness status at the time. Further research in MEMS thrusters is being conducted, including the double-base and black powder solid propellant microthruster array studied by Challane et al. in 2015 [13]. Their microthruster featured a  $100\mu\text{m}$ -diameter nozzle throat and produced thrust ranging from 0.1 to 3.5mN. MEMS is smaller than the scale explored in this study, but it offers a technological alternative should manufacturing become a prohibitive issue at the scale of this study’s work. Regardless of size, scale, or manufacturing technique, underlying rocket propulsion mechanics are the same and applied to all types of chemical propulsion.

## 2.2 Rocket Propulsion Principals

### 2.2.1. *Rocket and Nozzle Performance*

Rocket nozzle performance is typically evaluated in many ways, from measured quantities such as thrust and pressure, to calculated quantities of exhaust velocities and specific impulse. Rocket thrust,  $F$ , is the sum of two terms: momentum thrust and pressure thrust as seen in Equation 1. This equation originates from Newton’s second law where  $\dot{m}$  is mass flow rate,  $v_e$  is exhaust gas velocity at the nozzle exit,  $g_c$  is the gravitational proportionality constant,  $p_e$  is pressure at the nozzle exit,  $p_{atm}$  is atmospheric or ambient pressure outside the nozzle, and  $A_e$  is the nozzle exit area. This equation assumes each term remains constant with time. The first term is particularly relevant to this study as the mass flow rate is of particular interest in sizing the

designed nozzle to align with the geometry of similar thrusters. This is discussed further in Chapter III.

$$F = \frac{\dot{m}v_e}{g_c} + (p_e - p_{atm})A_e \quad (1)$$

Specific impulse,  $I_{sp}$ , is a measure of how efficiently thrust is generated for a given mass flow rate of exhaust gases and is independent of the size of propulsion system. Therefore, it is a useful metric of a system's efficiency, regardless of its scale. This parameter is often a function of the propellants utilized and for chemical rockets is greatest for bipropellant liquid propellants, moderate for solids and monopropellants, and low for cold gas thrusters. It is defined in Equation 3 where  $g_0$  is gravitational acceleration.

$$I_{sp} = \frac{F}{\dot{m}g_0} \quad (2)$$

An important metric of nozzle geometry is described by expansion ratio,  $\epsilon$ , that defines the area enlargement from the nozzle throat to exit. Conceptually, a nozzle converts the high pressure and temperatures of rocket combustion products into kinetic energy by means of high exit velocity. From Equation 1, thrust is generated as the product of this high exit velocity gas and the corresponding mass flow rate. It is desirable that as a nozzle expands the gases through the diverging section, the exit pressure match ambient pressures for perfect nozzle expansion. The amount of expansion accomplished by a nozzle is defined by  $\epsilon$  and is illustrated in Figure 4. The term on the righthand side of the equation stems from isentropic nozzle flow relations and is for achieving perfect expansion.  $\gamma$  is the ratio of specific heats for the exhaust gas, and  $p_c$  is the internal chamber pressure.

$$\epsilon = \frac{A_e}{A_t} = \left( \left( \frac{\gamma+1}{2} \right)^{\frac{1}{\gamma-1}} \left( \frac{p_c}{p_e} \right)^{\frac{1}{\gamma}} \sqrt{\left( \frac{\gamma+1}{\gamma-1} \right) \left[ 1 - \left( \frac{p_e}{p_c} \right)^{\frac{\gamma-1}{\gamma}} \right]} \right)^{-1} \quad (3)$$

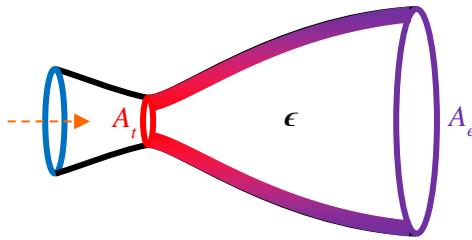


**Figure 4: Graphic of nozzle expansion ratio**

For perfect expansion to ambient pressure within the atmosphere, lower expansion ratios are needed because the exit pressure must only drop to those atmospheric levels. However, for in-space chemical propulsion systems, much larger expansion ratios are necessary to expand the high chamber pressure to vacuum or near-vacuum conditions. The challenge is twofold: a large area nozzle can become prohibitively heavy, and if expansion happens too rapidly, flow separation at the nozzle wall can occur. A longer nozzle will reduce flow separation and maximize efficiency, but also comes at the cost of a large, heavy nozzle. This tradeoff is illustrated below in Figure 5. Expansion ratio is a critical parameter to consider for this study as the nozzles here will only expand to atmospheric conditions 1000ft (305m) above sea level, but flight worthy in-space nozzles would be designed with larger expansion ratios to vacuum conditions.

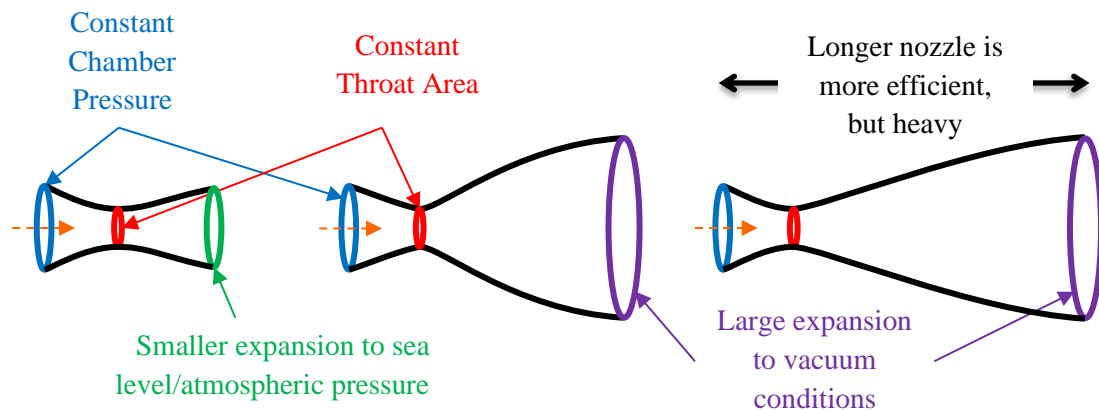


**Figure 5: Nozzle expansion configurations**

For example, the Aerojet Rocketdyne MR-106L 22N hydrazine thruster is an in-space propulsion unit featuring an expansion ratio of 60 and is shown in Figure 6. Other thrusters can feature expansion ratios of 100 or more.

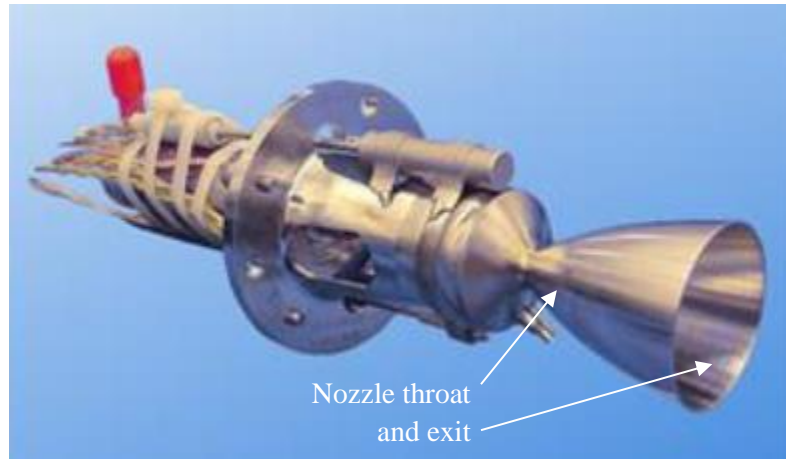


**Figure 6: MR-106L thruster with large bell nozzle for expanding to vacuum conditions [14]**

### 2.2.2. *Solid Rocket Propellants*

In this study, solid rocket propellant is used as a hot gas generator with combustion gases from the burning propellant exiting through a nozzle. A propellant grain, shown from Figure 7 in grey, is a segment of the solid propellant shaped in such a way to dictate a desired burn behavior. Solid propellant burns perpendicular to all exposed surfaces, and as a result, certain grain geometries exist to control a designed burn profile. Examples of grain geometry and their respective thrust curves are shown below in

Figure 7. This study will feature a neutral-burning grain in the shape of a cylindrical “endburner” to sustain a lengthy burn time as the flame front moves from one end to the other.

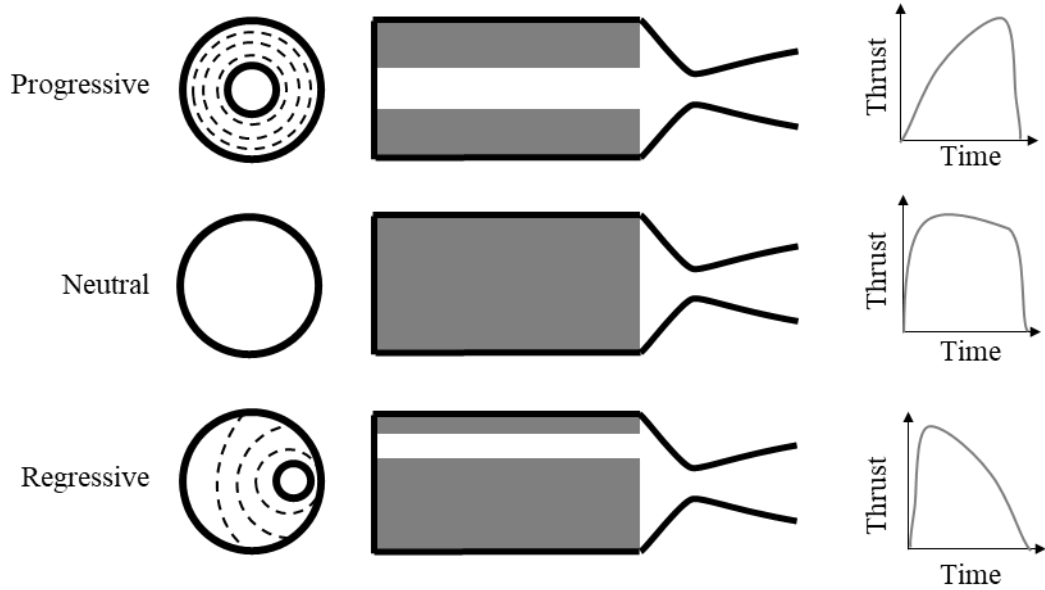


**Figure 7: Example solid propellant grain geometries and burn profiles**

The propellant consumption during combustion can be calculated as a function of the grain geometry, burn rate, and propellant density. Equation 4 allows for tuning of propellant grain geometry by fixing a desired mass flow rate.  $A_b$  is the area of exposed burning propellant,  $r$  is the propellant burn rate, and  $\rho_b$  is the propellant density prior to combustion. In this study, a target mass flow rate will be established and using Equation 4, the propellant grain dimensions will result. This process is described in detail in Chapter III.

$$\dot{m} = A_b r \rho_b \quad (4)$$

Propellant burn rate,  $r$ , is a function of chamber pressure as seen in Equation 5. It relies on a temperature coefficient,  $a$ , and burning rate exponent,  $n$ , that vary for different propellants and even for different batches of the same propellant. Characterization of a propellant batch is beyond the scope of this study, but the variation of burn rate with temperature is accounted for when designing the solid propellant grain later in this study.

$$r = a p_c^n \quad (5)$$

With combustion of solid or liquid propellants, very high gas temperatures occur, many above the melting temperatures of most metals. As a result, thermal management techniques are required.

### 2.3. Thermal Management in Combustion Chambers

Rocket combustion chambers and nozzles withstand combustion temperatures in a variety of ways. Some are active thermal management techniques, capable of operating at steady state for minutes at a time, even 8 minutes for the RS-25 Space Shuttle Main Engine, while others are more limited by material ablation or single-use insulating components like liners or nozzle throat inserts. A plot of wall heat flux vs axial location through the RS-25 engine is shown below in Figure 8. The greatest heat flux occurs near the nozzle throat, hence cooling is especially critical for this region.

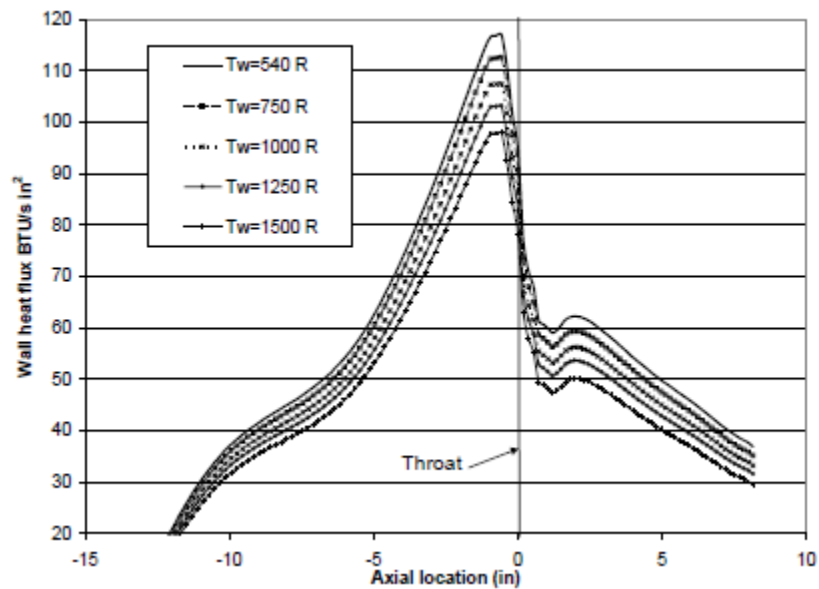


**Figure 8: RS-25 wall heat flux vs axial location [15]**

Radiation cooling is the simplest cooling technique in which the thrust chamber and nozzle radiate heat away into ambient conditions. The materials for withstanding the heat are often refractory metals, alloys, or composites. These can be expensive and heavy but offer the

greatest simplicity. This cooling strategy is most commonly used with small in-space thrusters such as the ones compared to in this study. Ablation is another simple method of cooling where a material inside the combustion chamber or nozzle is designed to erode or ablate away during the firing, thus removing heat with it. This is similar to a heat shield withstanding spacecraft reentry from orbit. A disadvantage is the changing nozzle geometry that can limit reuse or extended use. A more complex cooling strategy is film cooling, in which a thin layer of cool propellant or cycle exhaust gas provides a protective film of cooler fluid contacting the thrust chamber wall. Some propellant may not reach complete combustion and proper injection must be considered.

The final major thermal management technique is regenerative cooling. Prior to injection and combustion, a liquid propellant is circulated around the rocket's combustion chamber-nozzle assembly (referred to as a thrust chamber) through small passages, extracting heat to cool the chamber, and are then still utilized for combustion. These passages are subject to a range of design types that have changed with improving manufacturing, such as additive manufacturing, and advanced materials to include new superalloys and other metals. Three such passage types are shown below in Figure 9. This study will examine a coaxial shell geometry (one annular flow passage), and three types of channel designs with 4, 8, and 12 segmented passages. It is the goal of this study to quantify cooling effectiveness for these four designs and evaluate their application to small satellite propulsion scales.

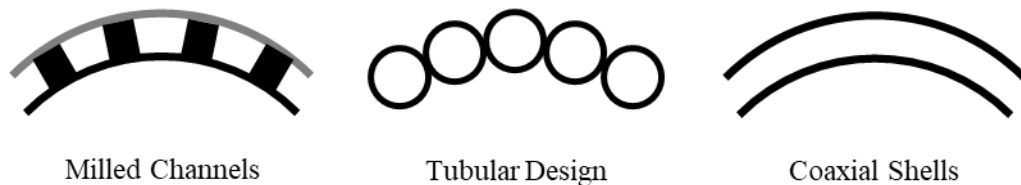


**Figure 9: Types of regen jacket channel designs**

A regenerative cooling jacket is complex to design and analyze due to high velocity, high temperature convective exhaust gases, thin wall heat conduction, a layer of liquid propellant that

cools by convection, another conductive wall, radiation into ambient conditions, pressure drops in the coolant passages, varying geometry along the converging-diverging nozzle profile, and gas and liquid boundary layer effects throughout. These varying materials and heat transfer modes are illustrated below in Figure 10. Discussion of these heat transfer principals and how they pertain to a regenerative cooling jacket are described in the following section.

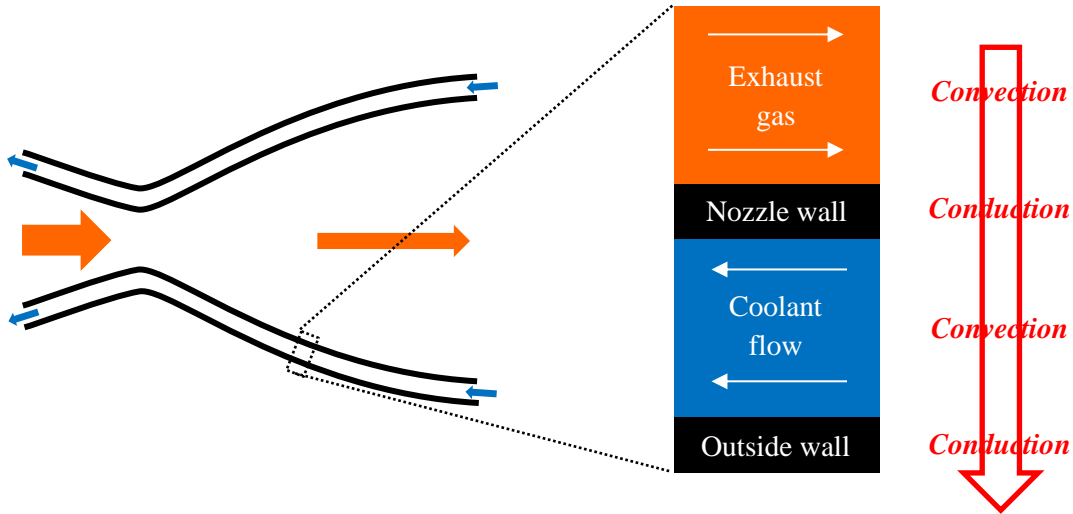


**Figure 10: Heat transfer modes in a regen jacket**

Advantages to regenerative cooling are that no thermal energy is lost from the system, and the preheated propellant augments exhaust velocity and performance slightly. It is the motivation of this study to examine the scope of preheat propellant temperatures achievable from a regeneratively-cooled small satellite-scale thruster and determine the effect of segmenting that cooling passage into multiple channels.

#### 2.4. Heat Transfer Principals

The two primary modes of heat transfer in regeneratively-cooled systems are convection and conduction. Heat flux,  $\dot{q}$ , by convection is described in Equation 6 where  $h_g$  is the gas-side heat transfer coefficient,  $T_r$  is the recovery temperature as it pertains to compressible boundary layers and is used instead of the gas' stagnation temperature driving heat transfer, and



$T_{wg}$  is the wall temperature of the gas-side. For steady state heat transfer through a nozzle wall, gas-side heat transfer is set equal to the cooling liquid heat transfer.  $h_l$  is the convection heat transfer coefficient of the liquid,  $T_{wl}$  is the liquid-side wall temperature, and  $T_l$  is the liquid bulk temperature.

$$\dot{q} = h_g(T_r - T_{wg}) = h_l(T_{wl} - T_l) \quad (6)$$

Conduction through the nozzle wall is expressed by Equation 7 where  $k$  is the thermal conductivity of the wall,  $t_w$  is the wall thickness,  $T_{wg}$  is the wall temperature of the gas side, and  $T_{wl}$  is the wall temperature of the liquid coolant side.

$$\dot{q} = \frac{k}{t_w}(T_{wg} - T_{wl}) \quad (7)$$

It is the goal of the analytical model to use Equations 6 and 7 to calculate heat transfer through the nozzle wall and cooling liquid to determine the liquid temperature at the exit. This is indicative of how much heat was extracted by the water and will determine cooling effectiveness for a range of cooling passages.

Calculation of the gas-side heat transfer coefficient is done using the Bartz correlation in Equation 8 and is one of the most common methods for estimating convective heat transfer of the exhaust gas flow to the nozzle wall in regen jacket analysis.  $D_t$  is the nozzle throat diameter,  $\mu$  is the gas viscosity,  $c_p$  is the specific heat,  $Pr$  is Prandtl number,  $g$  is gravitational acceleration,  $c^*$  is the characteristic exhaust velocity,  $R$  is the nozzle throat radius blend,  $A$  is the local segment area of the nozzle,  $\gamma$  is the ratio of specific heats, and  $M$  is local Mach number within the nozzle segment. The subscript *tot* indicates total or stagnation values for the gas. The quantities evaluated throughout each nozzle segment are characteristic of the exhaust flow and result from outputs of a chemical equilibrium calculator such as NASA Chemical Equilibrium with

Applications (CEA) or Rocket Propulsion Analysis (RPA), the latter of which is used in this study to obtain combustion and nozzle performance values in Chapter III.

$$h_g = \frac{\frac{0.026 \left( \frac{\mu^{0.2} c_p}{Pr^{0.6}} \right)_{tot} \left( \frac{p_{ctotg}}{c^*} \right)^{0.8} \left( \frac{D_t}{R} \right)^{0.1} \left( \frac{A_t}{A} \right)^{0.9}}{\left[ 0.5 \frac{T_{wg}}{T_{ctot}} \left( 1 + \frac{\gamma-1}{2} M^2 \right) + 0.5 \right]^{0.68} \left[ 1 + \frac{\gamma-1}{2} M^2 \right]^{0.12}} \quad (8)$$

Because of the low coolant flow velocities and small flow areas present in this study, calculation of the liquid heat transfer coefficient is done using Equation 9 for laminar flow and large surface temperature to liquid bulk temperature differences. This correlation derived from Sieder and Tate accounts for variation of viscosity as a result of this large temperature gradient between wall temperature and cooling temperature [16].  $D$  is the hydraulic diameter for non-circular channels,  $L$  is the length of flow segment,  $\mu$  is the bulk liquid viscosity, and  $\mu_{wl}$  is the fluid viscosity evaluated at the liquid wall temperature.

$$Nu = \frac{h_l D}{k} = 1.86 \left( \frac{Re Pr D}{L} \right)^{\frac{1}{3}} \left( \frac{\mu}{\mu_{wl}} \right)^{0.14} \quad (9)$$

To quantify the cooling effectiveness accomplished by the coolant liquid, Equation 10 is used. Cooling effectiveness  $\Phi$ , is often used for cooling of turbine blades and will also be used to determine the cooling accomplished in this study.  $T_g$  is the hot gas temperature,  $T_m$  is the average metal surface temperature between  $T_{wg}$  and  $T_{wl}$ , and  $T_c$  is the cooling liquid temperature.

$$\Phi = \frac{T_g - T_m}{T_g - T_c} \quad (10)$$

These equations dictating heat transfer are used to study the cooling channel segmentation effects and are especially pertinent for the unusually hot decomposition temperatures of green propellants.

## 2.5. Green Propellant Background

Green propellants, while of particular interest in the present, have actually been studied since the late 20<sup>th</sup> century. They are aqueous solutions of ionic liquids that are water-soluble ammonium salts [5]. These solutions are far less toxic than hydrazine, and reduced PPE and handling complexities lead to lower costs prior to launch. Additionally, performance improvements exist, not only yielding higher specific impulse, but also greater densities than hydrazine which enables more propellant mass to be carried for a mission utilizing the same tank volume. Three main reasons green monopropellants such as AF-M315E and LMP-103S haven't seen greater use on space missions include the well understood nature and experiences of handling hydrazine, higher combustion temperatures requiring new materials [12], and the large power requirement for ignition that is "infeasible to use in small spacecraft with limited power" [5]. The preheat temperature of green monopropellants can be significantly higher than the typical 120-150°C for hydrazine thrusters which translates into twice the necessary preheat power required on-board the spacecraft [17]. This study aims to determine if heat generated from the chamber could boost the green propellant temperature so as to reduce on-board electrical power needed for preheating.

For the TechSat-21 mission, the RK-315A green propellant was considered, but thrusters were budgeted to weigh 25% more than comparable hydrazine thrusters due to design requirements stemming from the high chamber temperature [12]. While a regeneratively-cooled thrust chamber may come at a weight expense for the added material of flow passages, weight savings could exist in the form of batteries or reduction in on-board electrical power generation if lower preheating energy requirements can be obtained from an actively-cooled chamber.

Unlike hydrazine which requires heating even during inactive coast periods in space to prevent freezing, AF-M315E undergoes glass transition at -80°C and may be allowed to fall to

low temperatures when not in use [6]. This reduces the system complexity necessary for heating the propellants during coast periods, but the cooled propellant must be reheated prior to decomposition. Circulating the propellant about the thrust chamber during operation with regenerative cooling could reduce the reheat energy requirements normally needed following startup.

## 2.6. Current State of Green 22N Thrusters

To provide background on 22N thrusters and those using green propellants, this section discusses the current status of the technology and where areas for improvement could exist. The NASA Green Propellant Infusion Mission (GPIM) satellite shown in Figure 11 launched in 2019 and is the first in-space demonstration of the AF-M315E green monopropellant. It utilized the Aerojet Rocketdyne GR-1 thruster (1N thrust) that was developed in parallel with the GR-22 thruster (22N thrust) that was not included in the on-orbit demonstration. These thrusters underwent testing and improvements including a manufacturability improvement of the GR-1 thruster promising a 50% cost reduction [18].



**Figure 11: Integration of the (5) 1-N GR-1 thrusters to NASA's GPIM satellite [19]**

The GR-1 and GR-22 thrusters incorporate “a number of optimizations specific to the increased thermal management requirements of high-performance (and higher flame temperature) advanced monopropellants” including stand-off structures for thermal isolation purposes. After testing of the GR-22, cracking of the chamber body was determined to be the result of thermal fatigue due to “steep temperature gradients in the vicinity of injectant impingement points along the chamber wall.” Despite the use of refractory alloys and radiation cooling, thermal failure still occurred at this point late in the thruster’s development.

The elevated temperatures from green propellant decomposition can also overheat upstream flow passages causing fouling and plugging of feed tubes and valves due to deposition of nonvolatile residue dissolved in the propellant [17]. Regenerative cooling could thus fulfill a critical need in reducing thermal extremes present during operation.

The GR-1 faces high production costs due to the refractory metal construction to withstand the elevated flame temperatures [18]. Aerojet Rocketdyne is considering modifying the thrust chamber support structure to use cheaper raw materials while also requiring less machining. This study takes a similar approach to utilize an alternative cooling approach, thus enabling cheaper metals to become suitable. Wilson of Aerojet Rocketdyne performed flight qualification testing on their MR-106L hydrazine thruster, and extensive hotfires and full duty cycle tests revealed small chamber cracks, likely due to creep deformation. While not concerning to the success of the lifetest, Wilson suggests increasing the wall thickness [20] rather than pursuing an alternative cooling approach for this radiation-cooled thrust chamber. A similar chamber utilizing regenerative cooling may eliminate such failures outright.

During testing of a 1N AF-M315E thruster, McGee utilized a TZM (titanium, zinc, and molybdenum) to preserve a more expensive iridium thruster that would be used for optimum performance [21]. These are shown in Figure 12. The author’s study examined testing and

performance of the thruster itself, and it was determined that the thruster's positive performance depended heavily on an elevated catalyst temperature. For a future study, "the next iteration of this test setup will have a focus on thermally insulating the thrust and catalysts from the thruster valve and test stand, thus alleviating the need to worry about heat being conducted away from the catalysts." A strong advantage to regenerative cooling is that the heat extracted by the circulating propellant remains within the system and the thermal energy absorbed is added during decomposition to augment performance.



**Figure 12: TZM thruster (left) vs iridium thruster (right) used by McGee with AF-M315E [21]**

In 2000, Mueller of Jet Propulsion Laboratory (JPL) conducted an exhaustive market survey of general thruster options for microspacecraft including bipropellant, monopropellant (hydrazine, hydrogen peroxide, and green hydroxylammonium nitrate, HAN-based), cold gas, tri-propellant, warm gas, solid propellant motors, hybrid motors, hall thrusters, field emission electric propulsion, colloid, pulsed plasma, and resistojet thruster options with a technology description for each as well as available hardware and evaluation, issues, and future work for each. For chemical propulsion, the author listed several chamber materials necessary for handling the high temperatures of combustion: rhenium-iridium composites and platinum/rhodium alloys [22]. These alloys will become prohibitively expensive if large numbers of spacecraft are flown exclusively with such thrust chamber materials, and regenerative cooling could enable more affordable metals such as aluminum, copper, and steel to become suitable. These more affordable

metals are also seeing increased use in additive manufacturing (3D printing) as metal printing is becoming more commonplace.

## 2.7. Additive Manufacturing Overview

Additive manufacturing (AM) has grown in recent years for its favorable potential in medical, manufacturing, and aerospace industries. Rapid prototyping is enabled, but the material science of the many 3D printing methodologies is still being researched and understood. Many print methods exist that use a range of materials and build up a part with powders, filaments, lasers, and other tools. Some of the most common methods include fused deposition modeling (FDM), stereolithography (SLA), selective laser sintering (SLS), direct metal laser sintering (DMLS), and atomic diffusion additive manufacturing (ADAM), the latter of which is used in this study. A summary of these techniques is given in

Table *I* below. Variants of these each printing methods exist, but they all utilize the same premise of building a part layer by layer, adding material rather than removing it as is commonplace in subtractive manufacturing (drilling, cutting, milling, etc). AM has many benefits, but the most significant to this study is the ability to integrate intricate internal geometries into a single part. Traditional manufacturing considerations don't limit design as much, and new structural or flow path techniques can be utilized.



**Table 1: Summary of common additive manufacturing techniques**

<b>Print Technique</b>	<b>Common Materials</b>	<b>Common Uses</b>	<b>Advantages</b>	<b>Disadvantages</b>
<b>FDM</b> – fused deposition modeling	Polymers	Rapid prototyping, face shield frames, hobby	Accessible, affordable, fast	Poor material strength
<b>SLA</b> - stereolithography	Polymers	Rapid prototyping, medical	Strong, affordable parts, fast	Post processing
<b>SLS</b> – selective laser sintering	Polymers, metals, ceramics	Aerospace, medical	Material strength	Higher cost
<b>DMD</b> – direct metal deposition	Metals	Aerospace, medical	Material strength	Surface roughness, overhang angles
<b>ADAM</b> – atomic diffusion additive manufacturing	Metals	Aerospace	Non-powder based, lighter parts	High cost, unproven, multiple steps after printing

Certain factors must be considered in additively-manufactured parts, and in this study, surface roughness of a part is significant. Test hardware in this study was 3D printed using 17-4 stainless steel ADAM in which stainless steel-plastic filament is extruded through a nozzle layer by layer to build up the part. The filament comprises stainless steel particles suspended with a plastic binder which are extruded like an FDM print to result in a “green part.” Upon completion, the part then enters a chemical bath to remove the plastic binder to yield the “brown part” and is finally sintered to reach full strength and material properties. A unique feature of ADAM is that as a result of the added plastic binder, the printed green part is up to 20% larger than the final sintered part. The manufacturer pioneering this technology, Markforged, utilizes a 20% scaling factor for the printed parts to account for the plastic binder removal, and therefore the estimated volume shrinkage is 72.8% according to Galati and Minetola who evaluated ADAM prints and confirmed this scaling factor to achieve the intended dimensional accuracy of printed parts [23]. It was also determined that final part densities for ADAM parts are lower than those made from

power-based AM methods. These findings do not change design considerations for this study, but the potential for some minor dimensional distortion is understood and kept in mind.

One limiting feature of most metal AM techniques is surface roughness. A part printed in layers will lack the smooth surfaces produced by other manufacturing techniques, and this can be particularly problematic for fluid flows when roughness is adverse. Particularly in this study with narrow internal flows and surface interactions of coolants and exhaust gases, surface roughness is a consideration when determining pressure drop and losses. This level of surface roughness is shown in Figure 13 for rocket nozzles made with ADAM. Even with a small layer height of 0.0049in (0.125mm), the layered surface texture is noticeable.

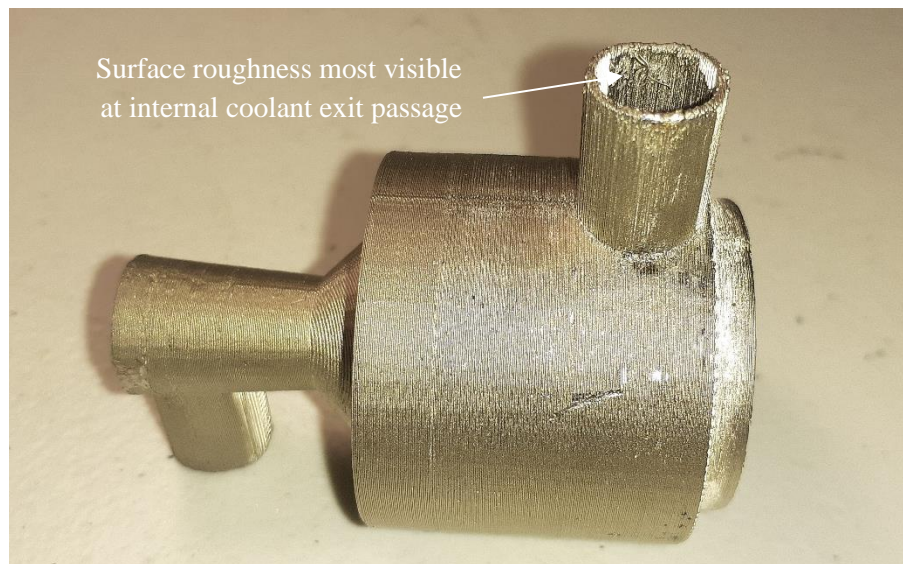


**Figure 13: ADAM-printed part with 0.125 layer height**

Saltzman et al. compared an aircraft heat exchanger for oil coolers that was additively manufactured versus one that was built with traditional techniques. After laser scanning the traditionally built part, they used a powder bed fusion printer with AlSi<sub>10</sub>Mg metal powder to manufacture a part with identical dimensions for testing. They observed twice as great of a pressure drop on the additively manufactured air flow side as the traditional part, but heat transfer was improved 10-14% [24]. The pressure drop was theorized to be due to surface roughness from

the powder-based laser fusion. This is an important consideration for further studies examining cooling flows over 3D printed parts.

For rockets, 3D-printed rocket engines are not brand new, but as can be seen in Table 2, production and flight-worthy systems are largely intended for use on launch vehicle scales with thrust exceeding 20kN. There have been no documented production variants or thrusters observed that utilize largely additively-manufactured hardware. This could be another area for application of AM to the spaceflight industry.

**Table 2: Summary of 3D-printed rocket engines in development or production**

<b>Engine Name</b>	<b>Manufacturer</b>	<b>Propellants</b>	<b>Thrust (kN)</b>	<b>Materials</b>	<b>Print Method</b>	<b>Regen cooled</b>
SuperDraco	SpaceX	NTO/MMH	73	Inconel	DMLS	Yes
Rutherford	Rocket Lab	LOX/RP-1	24		EBM	Yes
E-2	Launcher Space	LOX/RP-1	98	Copper	DMLS	Yes

Santi et al. designed and tested a 10N hydrogen peroxide thruster that was partially 3D printed [25] from stainless steel. It did not utilize regenerative cooling but neared a flight-worthy design by meeting criteria such as stable operation and fast ignition. This is largely the extent of small-scale additively-manufactured thruster hardware, and therefore the need to explore additional cooling approaches at this scale is warranted.

It is the motivation of this study to utilize regenerative cooling to alleviate many of the issues recognized with green propellants, most notably the elevated decomposition temperatures and difficulty in propellant ignition. This study will utilize additive manufacturing to vary the number of rectangular cooling passages of a thrust chamber analog and determine the cooling effectiveness of varying numbers and hence the size of the passages.

## CHAPTER III

### EXPERIMENTAL STUDY

#### 3.1. Test Bed Design

Green monopropellant thrusters utilize a decomposition reaction of a liquid propellant to achieve hot, high-pressure exhaust gases that are accelerated through a nozzle, generating thrust. Such systems are high performance, complex devices and their use is limited to the manufacturers and space research centers. As a result, for this study a test bed is developed for creating a similar rocket chamber environment without the complexity of handling liquid monopropellants or their respective propulsion hardware. This test bed utilizes an affordable, simple-to-manufacture solid propellant to generate hot, high-pressure exhaust gases. The composition of these gases is different from the liquid propellant decomposition, but the elevated temperatures are more suitable than other hot gas generators such as a heat gun or jet engine exhaust.

The solid propellant used was a 65/35 mass ratio of potassium nitrate to sorbitol (KNSB) that was mixed, cast, and cured into elongated propellant grains that utilize an endburning grain geometry. KNSB isn't generally used in an endburning configuration due to the low burn rate, but for generating exhaust gases rather than thrust, this propellant is suitable. Table 3 lists the comparison of KNSB combustion chemistry to hydrazine and several monopropellants.

**Table 3: Exhaust gas comparison of KNSB to liquid monopropellants [26-28]**

<b>Propellant</b>	<b>Ideal Specific Impulse (s)</b>	<b>Molecular Weight (g/mol)</b>	<b>Adiabatic Combustion Temperature (°C)</b>
Potassium nitrate-sorbitol (solid)	164	39.9	1327
Hydrazine (liquid)	234	32.1	800
AF-M315E (liquid)	250	96.04	1800
LMP-103S (liquid)	256	-	1600

### 3.1.1. Thruster Benchmarking

To align with the geometry of in-space thrusters, several 22N thrusters currently in production were used for benchmarking purposes of the nozzle throat area, exit area, and mass flow rate of propellant. It was rationalized that by aligning the combustion mass flow rate and coolant flow rate with that of the production thrusters, similar heat transfer would be achieved. Several of these thrusters are shown in Table 4.

**Table 4: 22N Thrusters in development or in production**

<b>Thruster</b>	<b>Manufacturer</b>	<b>Propellant</b>	<b>Throat Diameter (mm)</b>	<b>Exit Diameter (mm)</b>	<b>Mass Flow rate (g/s)</b>	<b>Chamber Pressure Range (PSI)</b>
MR-106L	Aerojet Rocketdyne	Hydrazine	0.567	34	4.1-14	56-195
MONARC-22-12	Moog	Hydrazine	0.96	38.5	-	70-400
Bradford ECAPS	22N HPGP	LMP-103S	-	-	4.9	80-350
R-6F (bipropellant)	Aerojet Rocketdyne	Monomethyl-hydrazine/ Nitrogen tetroxide	2.6	60.9	7.4	100-300

With some of these major nozzle dimensions and mass flow rates understood, a KNSB propellant grain was designed to produce similar mass flow rates of burning solid propellant based upon chamber pressure and corresponding burn rate at that pressure using Equations 4 and

5. A target mass flow rate of 0.35oz/s (10g/s) and chamber pressure of 200PSI (1.4MPa) were chosen to be within the limits of similar thrusters as can be seen from Table 4.

Nakka determined the KNSB burn rate across a range of pressures from 200-1500PSI (1.4-10MPa) [27]. For the intended chamber pressure, the corresponding temperature coefficient was 1.648 and the burn rate exponent was -0.314. By applying these exponents to Equation 5, a burn rate for KNSB at 200PSI (1.4MPa) was determined to be 0.31in/s (7.9mm/s).

KN-Sorbitol					
Pressure range		a	n	Pressure range	
psia		in/sec. (psia)		Mpa	
				mm/sec. (Mpa)	
15	to 117	0.019	0.625	0.103	to 0.807
117	to 218	1.648	-0.314	0.807	to 1.50
218	to 550	0.330	-0.013	1.50	to 3.79
550	to 1020	0.011	0.535	3.79	to 7.03
1020	to 1548	0.277	0.064	7.03	to 10.67

**Figure 14: Burn rate behavior for KNSB propellant [27]**

The calculated burn rate then was then applied to Equation 4 to identify the corresponding exposed surface area for burning. Assuming an end-burning cylindrical propellant grain with only the circular face exposed to the burning side, an area of 1.004in<sup>2</sup> (648mm<sup>2</sup>) results. For a circle, this area yields a diameter of 1.17in (29.7mm). To align with existing motor testing hardware and supplies, the actual propellant diameter was increased to 1.22in (31mm), so the KNSB motors could be cast into the Aerotech-compatible casting tube and liner from Always Ready Rocketry. Oklahoma State University has rocket motor casings and closures from previous projects that align with this size [29], and therefore the slight size increase was made to fit the already available hardware and supplies. The corresponding actual mass flow rate based upon the diameter enlargement is shown below in Table 5. These calculations are shown in the appendix. At this point, the propellant grain dimensions are fixed to align with a chamber pressure of 200PSI (1.5MPa) and mass flow rate of 0.35oz/s (10g/s). With the propellant grain dimensions set, nozzle design may begin.

**Table 5: Gas generator and KNSB grain design quantities**

<b>Quantity</b>	<b>Value</b>
Target chamber pressure	200 PSI (1.4 MPa)
Temperature coefficient, $a$ @ 200PSI	1.648
Burn rate exponent, $n$ @200PSI	-0.314
Burn rate, $r$ @ 200PSI	0.31 in/s (7.9 mm/s)
Target mass flow rate	0.35 oz/s (10 g/s)
Burning area @ 0.35oz/s mass flow rate	1.075 in <sup>2</sup> (693 mm <sup>2</sup> )
Calculated endburning grain diameter	1.17 in (29.7 mm)
Actual endburning grain diameter	1.22 in (31 mm)
Actual mass flow rate	0.38 oz/s (10.9 g/s)

*3.1.2. Converging-Diverging Nozzle Geometry*

After establishing the propellant diameter and target chamber pressure above, the rocket nozzle was designed using the MotorSim 2.0 internal ballistics simulator for estimating motor performance [30]. To do this, the propellant type was selected (KNSB) which loads the burn rate information for any pressure that is achieved during simulations. The grain diameter, length, and shape are entered. For a cylindrical endburning grain, the length can be increased as desired to extend burn time. A 6in (152mm) grain length yielded an 18s burn time which was to allow for thermocouple response time and heating transients of the nozzle. Once the propellant type and grain dimensions are entered, nozzle parameters of nozzle efficiency, throat diameter, and exit diameter can be adjusted to achieve the intended chamber pressure, burn time, or other performance parameters such as impulse or thrust. For a fixed grain geometry, throat diameter is the driving parameter to control average chamber pressure.

To calculate the exit diameter, perfect nozzle expansion is desired. While thrust and impulse aren't performance parameters of interest for this study, designing for perfect expansion avoids flow separation from over expansion or unnecessary exhaust gas impingement of under expansion. Equation 3 was used with a 1.042 ratio of specific heats for KNSB and resulted in a

nozzle exit diameter of 0.23in (5.8mm) for perfect expansion to 14.2PSI (0.098MPa) at 1000ft (305m) above sea level for Stillwater, OK where testing would occur. These calculations are given in the appendix as well. Those nozzle dimensions were entered into MotorSim and resulted in the cross section shown in Figure 15. An expansion ratio of 3.3 resulted. Most in-space thrusters utilize very large expansion ratios (50 or more), but due to manufacturing constraints, the low internal chamber pressure, and expansion to atmospheric pressure rather than vacuum conditions, the low expansion ratio results. Furthermore, in-space thrusters feature bell nozzles rather than the conical nozzle modeled in MotorSim. Bell nozzles allow for shorter overall length to achieve the same expansion ratio, but when used with solid propellants, ablation and erosion of the bell nozzle wall due to larger concentrations of solid particulates in the exhaust than liquid propellants makes bell nozzles less desirable for solid propellants than liquids [7]. The lower expansion ratio and conical nozzle are two primary design differences from production spacecraft thrusters.

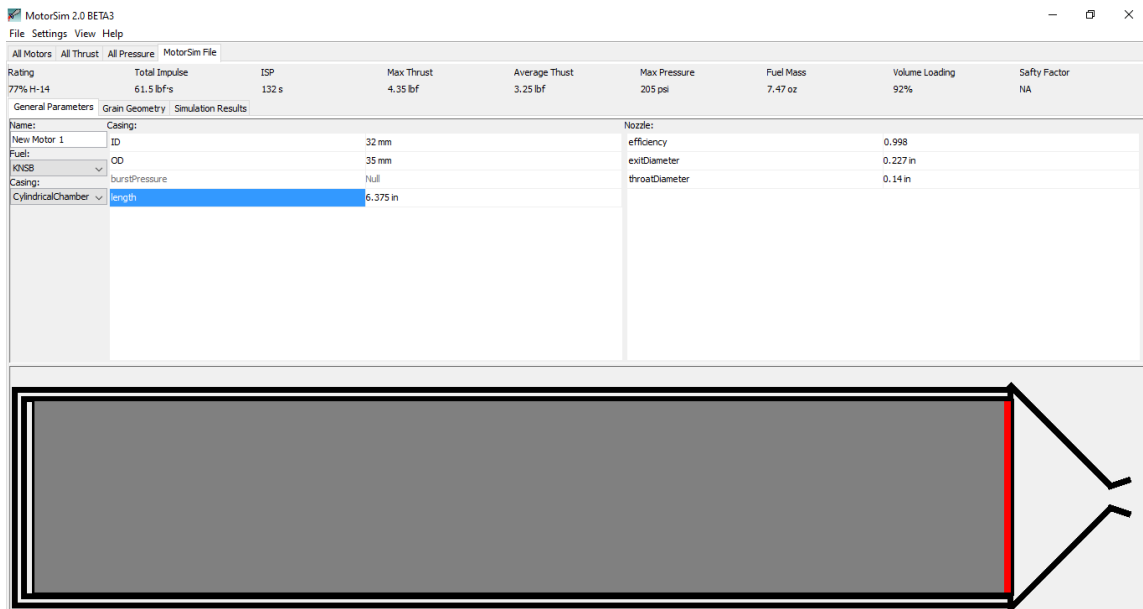


**Figure 15: MotorSim screenshot of 6 inch-long propellant grain**



Simulation results for thrust and pressure during the burn are shown below in Figure 16. At this point, igniter installation was also considered. For ease of placement and safety, the igniter would be inserted through the nozzle throat and must therefore be wide enough to accommodate a 0.13in (3.3mm) ematch head. The average pressure resulting from the throat enlargement to 0.14in (3.6mm) was 162PSI (1.1MPa).

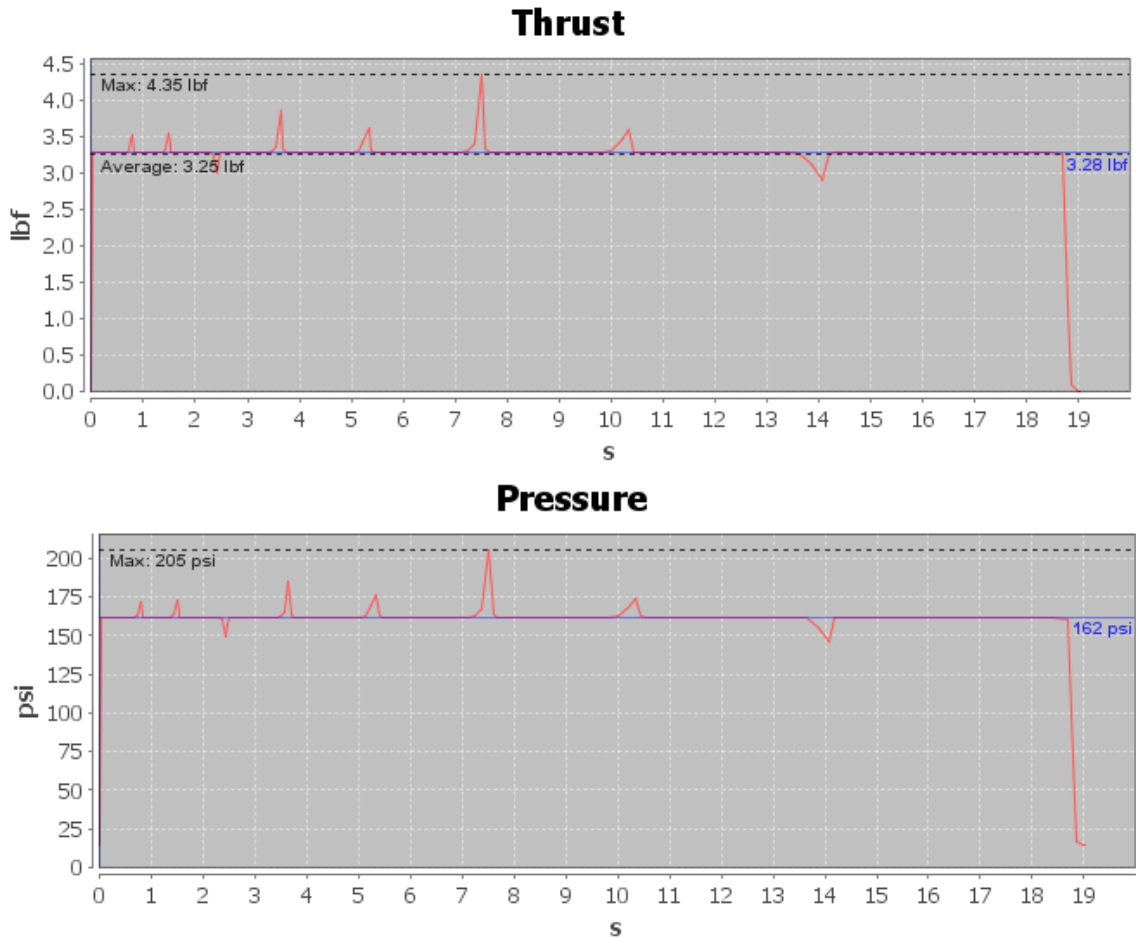


**Figure 16: MotorSim simulation results for thrust and pressure during the 18s burn time**

Most rocket nozzles using this type of hardware feature 45 and 15 degree half angles for the converging and diverging sections, respectively. The 45 converging half angle was maintained, but due to the small expansion ratio, a 15 diverging half angle would result in an impractically short diverging section. As the goal of this study is to study liquid cooling of a

nozzle, this half angle was reduced to 4 to provide added length for cooling flows. A chamber extension above the converging section was added for additional cooling passage length. These dimensions are provided in engineering drawings in the appendix. For the exhaust gas nozzle flow path established, cooling passages and motor integration features could be added.

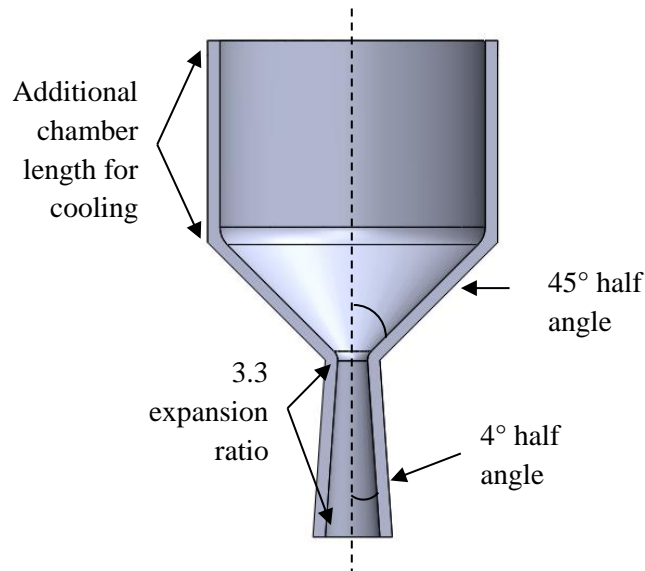


**Figure 17: Uncooled converging-diverging nozzle profile**

### 3.1.3. Motor Integration and Cooling Channel Geometry

With the converging-diverging nozzle areas established, integration with the motor hardware is next, as this imparts dimensional constraints for fitting inside existing motor hardware. The motor casings were cut from 6061-T6-drawn aluminum tube with an outer diameter (OD) of 1.5in (38.1mm) and an inner diameter (ID) of 1.384in (35.2mm). This tube ID constrained the final nozzle OD to 1.374in (34.9mm) to provide 0.005in (0.127mm) of clearance between the nozzle and casing. Following the surface roughness of the ADAM process, additional clearance could have been used, but the parts fit with these tolerances, nonetheless. To

provide a seal against hot gases, a 216 O-ring gland was applied at the top of the nozzle to prevent hot gases from escaping around the nozzle.

To supply water coolant about the circumference of the nozzle, a thin parallel passage was wrapped about the C-D geometry. The wall thicknesses was capped at 0.05in (1.3mm) to align with the single wall printing path used in the Eiger [31] slicing program prior to 3D-printing. For wall thicknesses greater than 0.05in (1.3mm), it was observed that Eiger split the single wall into two thinner walls to reduce printing time and materials. To avoid the added complexity of analyzing a second wall and gap, the indicated wall thickness was maintained. The coolant passage was also fixed to 0.05in (1.3mm) thick as it was observed by Durkee et al. [32] that thinner flow passages are conducive to symmetric coolant flow and reduces gravitational effects and cavitation within passages. Thinner passages also help accelerate the flow allowing for higher Reynolds numbers and improved convective heat transfer coefficient. For a constant liquid layer thickness, the cross-sectional area is reduced towards the throat then increased again at the coolant passage extension. This single flow passage cross section is shown below in Figure 18 along with other design components of the nozzle such as the O-ring gland.

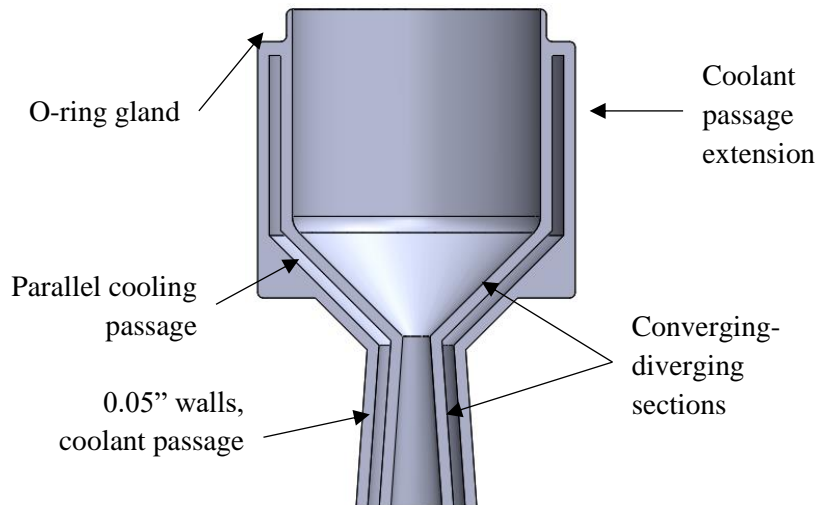


**Figure 18: Nozzle cross section with coolant passage**

To supply and collect the coolant flow throughout the nozzle, inlet and exit manifolds were added. The inlet and exit connected to clear PVC hose 5/16in (7.9mm) ID, 7/16in (11.1mm) OD, and 1/16in (1.6mm) thickness via friction fit connection to the part. These inlets and exits are depicted below in Figure 19 as well as the flow paths for the 2 fluids.

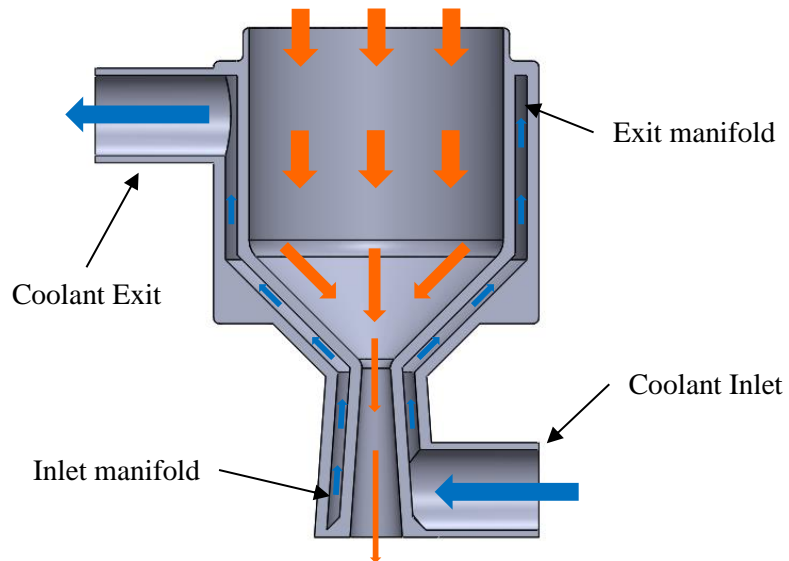


**Figure 19: Coolant (blue) and exhaust gas (orange) flow paths**

To ensure even flow behavior throughout the nozzle, the manifolds and flow paths were validated experimentally by inspection with fused deposition modeling (FDM) 3D-printed parts using polylactic acid (PLA) to ensure adequate flow distribution about the flow passages. One such test part is shown below in Figure 20 with the coolant exit manifold and coolant exit portions of the part removed to as to examine flow distribution before the coolant collects and exits the nozzle.



**Figure 20: Test part to ensure even coolant inlet flow distribution within the nozzle**

With the coolant flow deemed symmetric and even, final design tweaks were added such as rounding out the edges on the O-ring gland. The final nozzle is shown below in Figure 21.

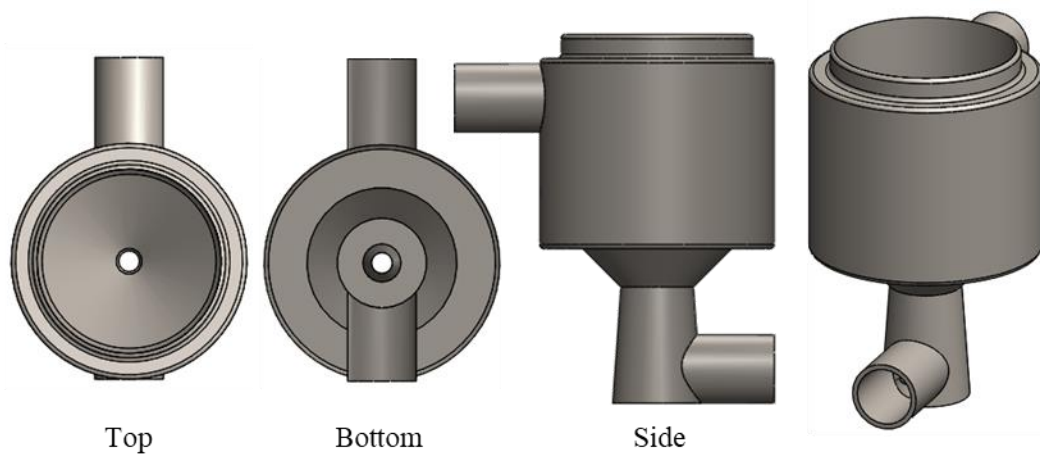


**Figure 21: Final nozzle design in various orientations**

With the nozzle part in its current state of a single annular flow passage throughout, it is most similar to the cooling geometry of a coaxial shell as shown in Figure 9. To vary the number of cooling passages by segmentation, the same flow area is split into smaller channels by a thin

wall. The dimensions of this wall are constant throughout the nozzle length and are shown below in Figure 22.

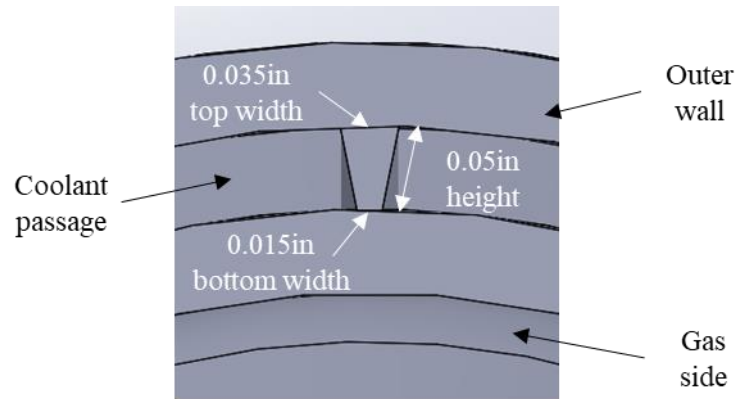


**Figure 22: Channel wall dimensions within coolant flow passage cross section**

Finally, the number of cooling passages was varied to include thrust chambers with 1, 4, 8 and 12 separate passages, although the coolant layer thickness was held constant. Cross sections at the diverging nozzle section, throat, and chamber extension are shown below in Figure 23. The flow area is minimized at the nozzle throat, which for an incompressible cooling liquid following continuity, will increase the fluid velocity. This fact is confirmed in the analytical modeling results section of Chapter IV.

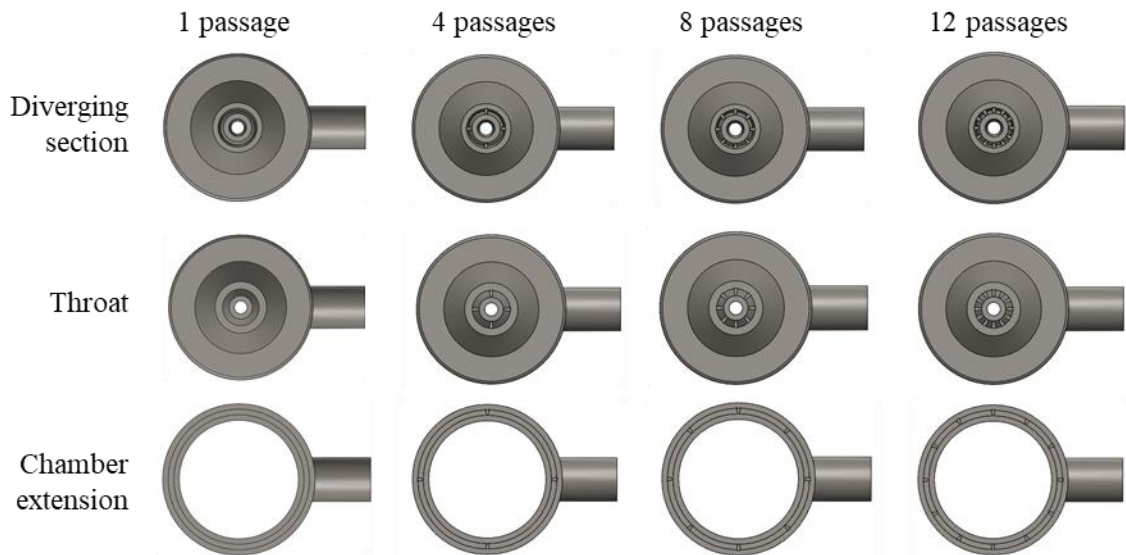


**Figure 23: Nozzle configurations at several cross sections**

To quantify the area changes throughout the nozzle, Table 6 shows the computed flow areas for each of nozzle configuration at the three sections described by Figure 23. Adding more channel walls decreased the flow area by the values shown below in Table 6 because the cooling channel height was unchanged. The negative change in area and negative percentages indicate a decrease in flow area from the coolant inlet, while positive changes in area and positive percentages indicate an increase in flow area from the coolant inlet.

**Table 6: Coolant flow area changes throughout nozzle**

# of Passages	Location	Area (mm <sup>2</sup> )	Area from change inlet (mm <sup>2</sup> )	% area change from inlet
1	Diverging	35.5	-23.1	-40%
	Throat	28.4	-30.2	-52%
	Converging	124.0	65.4	112%
4	Diverging	28.6	-30.0	-51%
	Throat	24.5	-34.1	-58%
	Converging	118.7	60.1	103%
8	Diverging	25.3	-33.3	-57%
	Throat	21.3	-37.3	-64%
	Converging	117.2	58.6	100%
12	Diverging	22.1	-36.5	-62%
	Throat	18.0	-40.6	-69%
	Converging	113.8	55.2	94%

The final design feature of these nozzles include two considerations for additive manufacturing. Support material exterior to the nozzle wasn't problematic, but internal support material was avoided as there was no way to remove that if constrained within internal flow passages. The print orientation was that in Figure 24 as to minimize support material for the coolant exit passage. However, the coolant channel walls and top cap required an overhang support ledge to avoid printing over empty space. These two features are shown below.

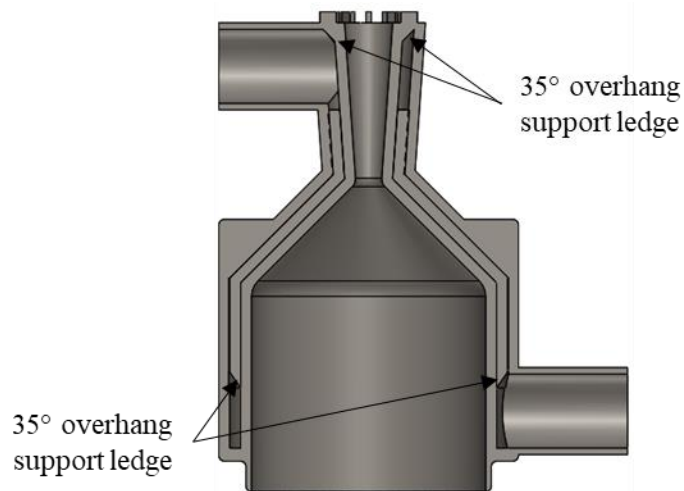


**Figure 24: AM considerations for printing internal passages without support material**



Those final elements comprised the completed 3D file, and the 4 parts (varying internal flow passages at 1, 4, 8, and 12) were sent to be printed on the Metal X machine. The following print specifications were used: 17-4 stainless steel print material, triangular fill pattern, 4 roof layers at 0.5mm layer height, 4 floor layers at 0.5mm layer height, and 4 wall layers at 1mm thickness. The post-sintered layer height was 0.125mm throughout the final product. The manufacturing process followed the ADAM steps described in Chapter II, and images throughout these stages are shown below in Figure 25.

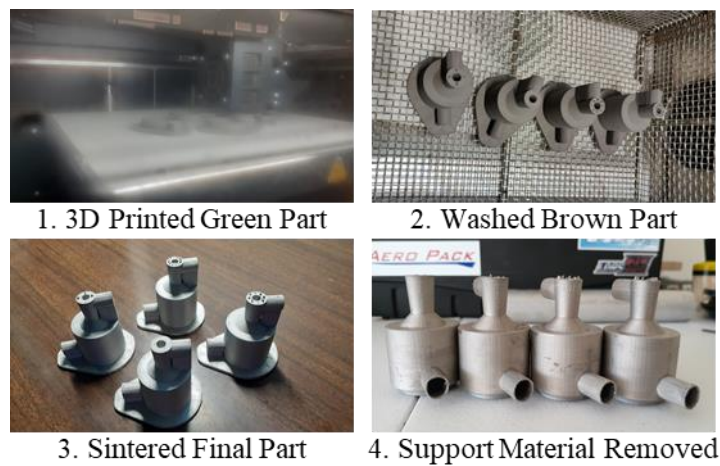


**Figure 25: 3D-printed nozzles from ADAM throughout the processing stages**

The final nozzles are ready for firing at this point. The gas generator test setup was prepared, and subsequent hotfire tests followed.

#### *3.1.4. Solid Propellant Rocket Motor/Gas Generator*

To create the hot, high pressure exhaust gases necessary to thermally evaluate cooling effectiveness, KNSB propellant grains were mixed and cast matching the dimensions determined from calculations described in Section 3.1.1. This mixing and casting process is described in detail by Moody et al [29]. Each 6in (152mm)-long grain was cast to weigh  $7.13 \pm 0.035\text{oz}$  ( $202 \pm 1\text{g}$ ) including the casting tube. Existing 38mm solid rocket motor hardware was used due to

availability and testing capability. This hardware is a common size in high-power rocketry and aligns with the testing capabilities at Oklahoma State University. The hardware uses internal retaining rings (snap rings) and closures to seal the cylindrical chamber. Ease of manufacturing is a large advantage, and minimal parts are needed. These parts are shown in Figure 26 below.

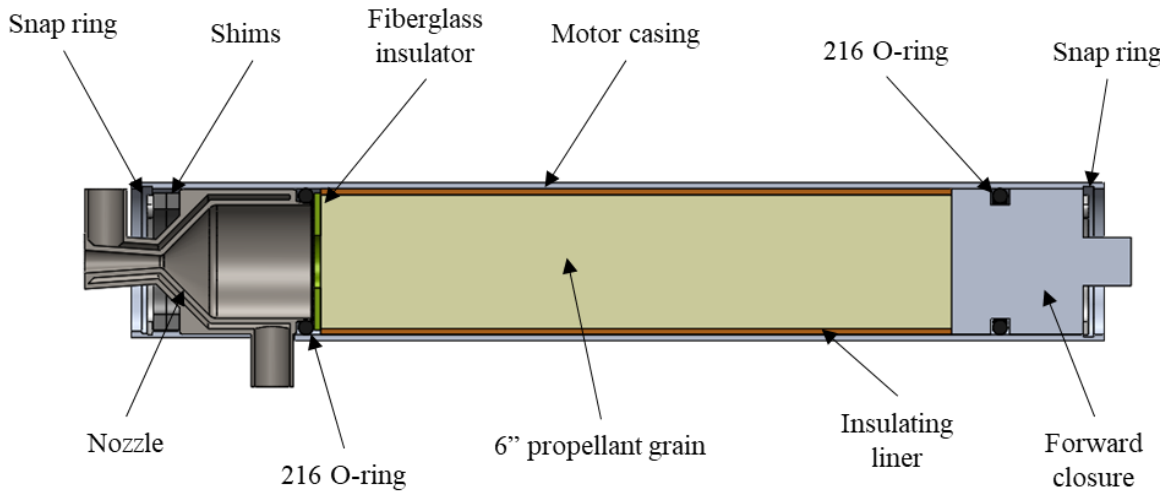


**Figure 26: Components of the assembled gas generator**

The only part modification was for the casing to accommodate the nozzle coolant exit. A notch was cut into the casing 0.4in (1cm) in diameter, so that the nozzle could slide into place for assembly and disassembly. Additionally, a 0.0625in (0.16cm) fiberglass insulating washer protects the aft O-ring from some of the heat of combustion. The assembly parts are shown separately in Figure 27. One distinction is that the forward closure shown in these figures was replaced during testing with a different forward closure, tapped with  $\frac{1}{4}$  NPT threads to attach a t-joint and pressure sensor. This arrangement is discussed further in the section 3.1.6.

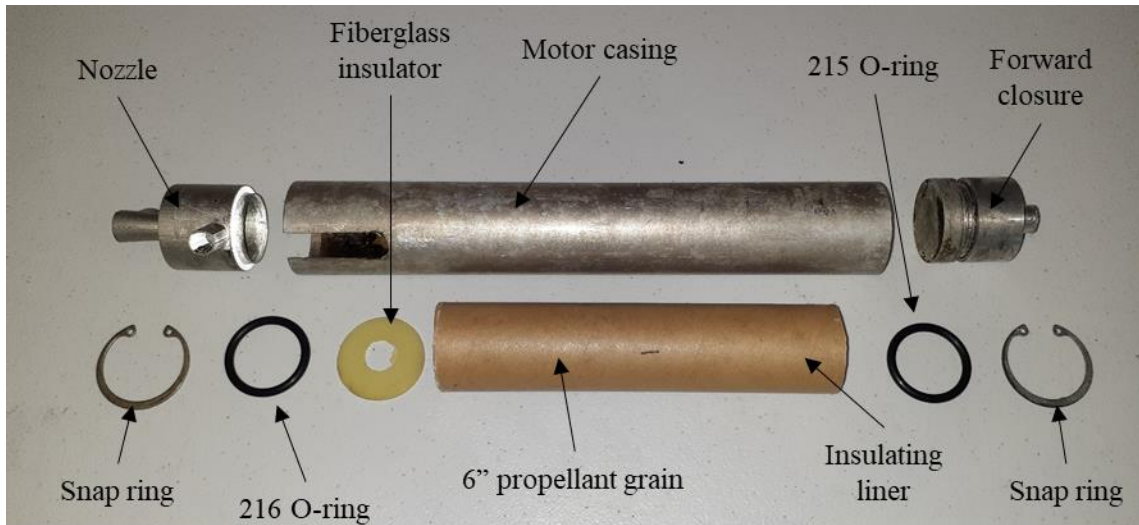


**Figure 27: Gas generator components prior to assembly**

### 3.1.5. Test Setup Integration

For the complete experimental setup, three major systems are integrated: the additively manufactured nozzle, the coolant feed system providing water through the thrust chamber walls, and the KNSB gas generator providing the hot, high-pressure exhaust gases.

The coolant feed system utilizes a 58in (1.5m)-long, 7/16in (11.1mm) OD clear PVC hose that supplies water from a plastic tank to the nozzle. The tank measures 14in (356mm) tall and 11.25in (286mm) in diameter with an open cap at the top for atmospheric pressure. Prior to a firing, it is filled with 8L of water providing 6in (152mm) of depth for head pressure. The assembled rocket motor is secured 2in (51mm) above the thrust stand table, so the head pressure supplying water is 0.144PSI (1kPa) gauge. This was determined experimentally to produce an average cooling water mass flow rate of 0.28oz/s (8g/s). Throughout the 27s motor burn, the tank drains 0.5in (12.7mm) which results in a final head pressure of 0.126PSI (0.9kPa) gauge and reduces the mass flow rate to 0.25oz/s (7g/s). To seal off water flow before and after a firing, a C-clamp is tightened over a portion of the PVC hose to stop the flow.

The KNSB gas generator (rocket motor) is fitted with a lightly greased 216 O-ring at the nozzle and a 215 O-ring on the forward closure. The smaller O-ring on the forward closure is due to the gland dimensioning during previous manufacturing. The propellant grain and cardboard liner are fitted into the casing and components secured with snap rings. The motor is affixed to the stand via pipe clamps and the PVC hoses attached to the coolant inlet and exit. The completed assembly is shown below in Figure 28.



**Figure 28: Water coolant flow setup prior to motor firing (left) and flow rate validation (right)**

### 3.1.6. Instrumentation

During testing, 2 J-type thermocouples record temperature during the burns. A surface-mounted thermocouple was clipped into place at the nozzle exit, and a second thermocouple measured the coolant exit water temperature. This probe was inserted into the PVC hose attached at the coolant exit. The location of these is shown in Figure 29.



**Figure 29: Thermocouples installed onto nozzle for firing**

This test rig was centered around the Oklahoma State University 500lb rocket thrust stand. The stand is comprised of a steel table, useful for preparing tests and mounting the flow rig and thermocouples. It provides linear bearings and mounting points for securing rocket motors of diameters 1.5-4in (38-98mm) and lengths up to 36in (0.9m). It also features a 500lb ( $\pm 0.5\%$  accuracy) load cell for thrust readings and 1500PSI ( $\pm 0.5\%$  accuracy) pressure sensor for obtaining internal pressure data during a motor burn. Lastly, it contains the power supply, amplifier, and data acquisition (DAQ) card for recording these data as well as an electric relay to remotely control motor ignition. These components are photographed in Figure 30.

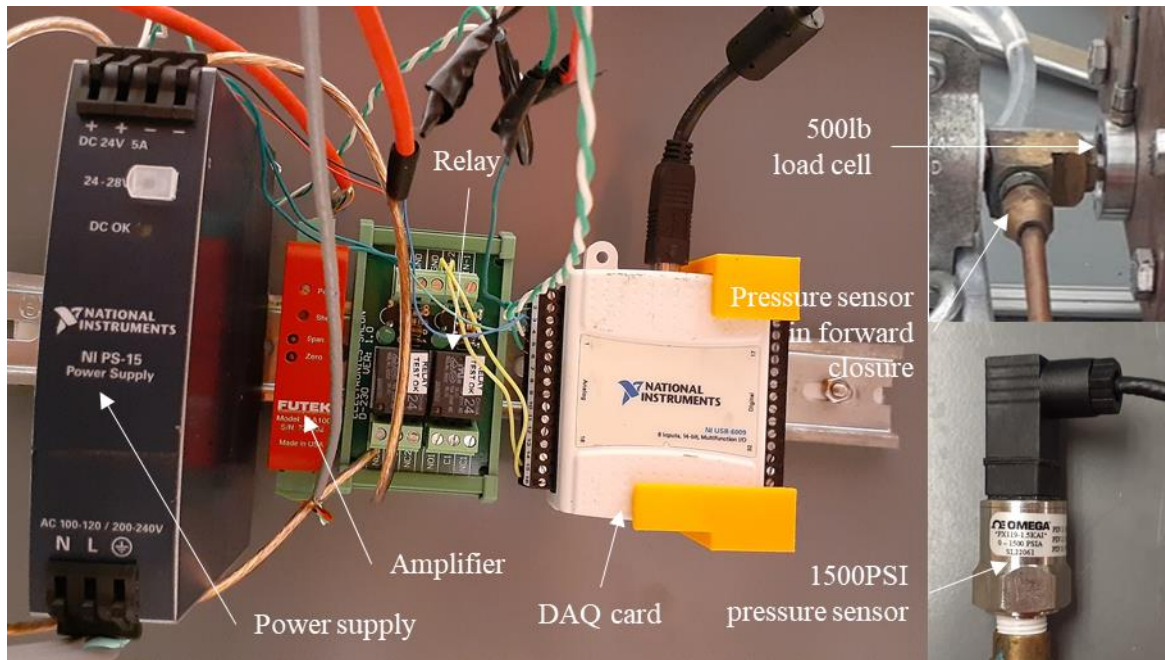


**Figure 30: Thrust stand instrumentation and data acquisition components**

While studying the motor's thrust and pressure were not the goal of this study, these measurements are nonetheless recorded for each firing as to record burn time and check for potential issues during the motor burn. Utilizing this stand also provides the means of controlled, remote ignition in the interest of safety during these long motor burns. A schematic of these components and their dependencies are shown in Figure 31.

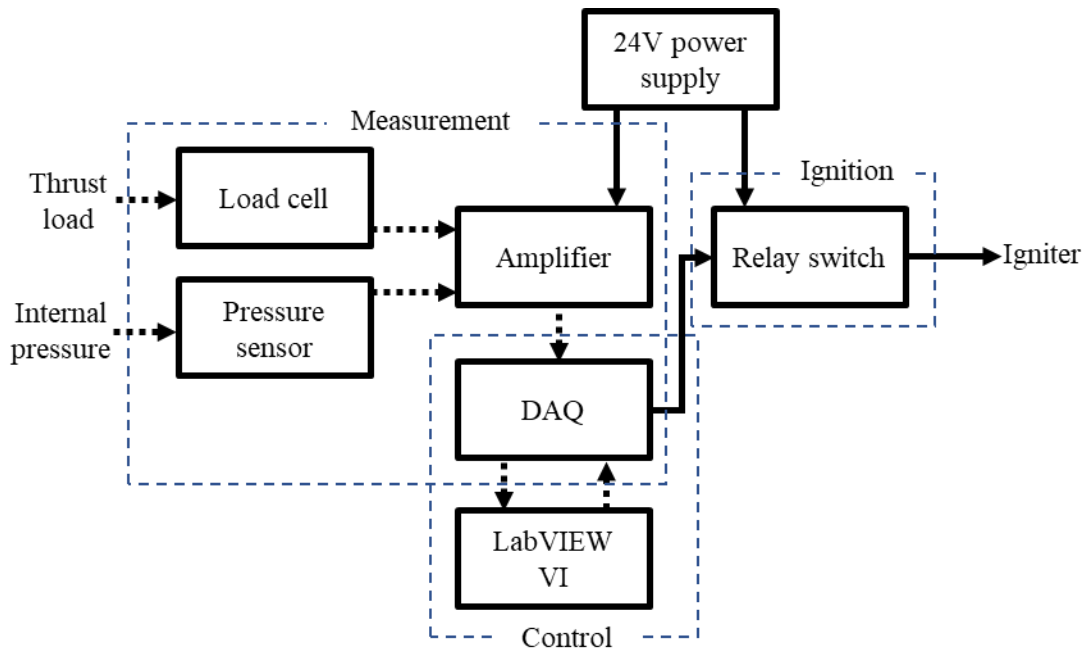


**Figure 31: Thrust stand component schematic and flowchart**

For operating the stand and collecting temperature data, 2 separate virtual instruments (VIs) are run in National Instrument's LabVIEW program [33]. One VI controls thrust stand ignition and data acquisition, and the second records temperature data from the 2 thermocouples. These 2 VI interfaces are shown side by side in Figure 32 as they were used during each test. Both VIs can vary the sampling frequency and sampling duration, but pressure and thrust samples were recorded at 1000Hz and thermocouple data recorded at 5Hz for all trials.

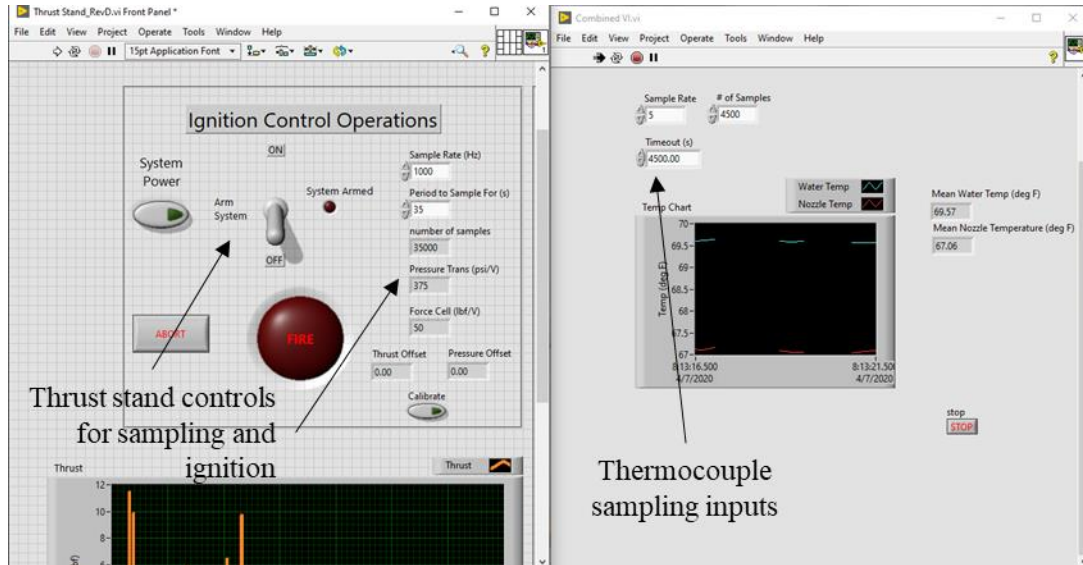


**Figure 32: LabVIEW VI interfaces for the thrust stand (left) and thermocouples (right)**

### 3.2. Hotfire Testing Procedures

Following motor installation on the thrust stand, connection of the water flow hoses, and affixing the thermocouples, all that remains is insertion of an electric match (ematch) to facilitate motor ignition. The ematch is connected to the thrust stand's equipped alligator clips for each wire lead and pushed through the nozzle throat until seated against the propellant grain face. A video camera begins recording, the C-clamp is opened to allow water flow through the nozzle. The area is cleared of any personnel, the thermocouple VI is run and confirmed functional, then the thrust stand VI is run, and finally the ignition sequence is initiated. This circuit ignites the ematch and the motor burns for its 27 seconds.

The thrust stand VI runs 35 seconds in case an ignition delay occurs, but the thermocouple VI is allowed to run for 15 minutes to capture the cool-down transient after motor burnout. Upon motor burnout, the water flow is shut off 90 seconds after opening the flow. After the 15 minute thermocouple sampling duration, instrumentation is removed, the motor disassembled and cleaned, the water capture weight recorded to confirm average mass flow rate



during the burn, and the tank refilled to the 8L mark. Each of the four nozzles is fired once. The nozzle with 1 cooling passage during a firing is shown below in Figure 33.



**Figure 33: Single cooling passage nozzle during firing**

### 3.3. Analytical Model

This analytical model was designed to compare experimental data and also study the thermal effects of cooling effectiveness by segmenting the cooling passage. This analysis follows the regenerative cooling jacket process described by Heister et al [26] and makes several simplifications that while not exactly representative of the conditions seen during testing, can still be used to draw conclusions of segmentation effects. This procedure does not dictate a design in terms of identifying coolant passage dimensions; rather, it assumes an existing flow path geometry and outputs values such as the total heat flux throughout the nozzle, cooling liquid temperature change, and internal pressure changes of the coolant.

This model assumes all heat transfer from the hot gas enters the cooling liquid and negligible heat transfer is due to radiation. It assumes steady state heat transfer and does not account for frictional losses from the gas or liquid. The nozzle is segmented into 12 slices upstream of the throat, and 13 slices downstream. The fluid and thermal properties are evaluated at each slice before applying a heat transfer balance to obtain the properties at the next slice. In this manner, the final properties are known, and the nozzle is characterized. As with the experimental setup, the liquid coolant is water and enters at the nozzle exit slice and moving upstream, opposite the flow direction of the hot gas.

With these assumptions and segments known, establishing the gas properties throughout the nozzle are the necessary first step. Using Rocket Propulsion Analysis (RPA), the KNSB composition, chamber pressure, nozzle shape, and ambient operating conditions are defined. It then runs its analysis to define the gas flow properties such as temperature, pressure, Mach number, Prandtl number, viscosity, and conductivity at each slice. The outputs of some of these slices at the converging section are shown below in Figure 34.

Chamber Performance										
Thermodynamic properties	Performance	Altitude performance	Throttled performance							
<b>Thermodynamic properties</b> (O/F=1.857)										
Parameter	Injector	Nozzle inlet	A/At=70.300	A/At=61.740	A/At=53.190	A/At=44.630	A/At=36.080	A/At=27.520	A/At=18.970	
Pressure	1.2066	1.2065	1.2065	1.2065	1.2065	1.2064	1.2063	1.2062	1.2059	
Temperature	1560.9354	1560.9294	1560.9275	1560.9256	1560.9234	1560.9164	1560.9094	1560.8909	1560.8479	
Enthalpy	-5776.8077	-5776.8183	-5776.8225	-5776.8266	-5776.8315	-5776.8469	-5776.8623	-5776.9029	-5776.9973	
Entropy	7.4326	7.4326	7.4326	7.4326	7.4326	7.4326	7.4326	7.4326	7.4326	
Internal energy	-3414.1407	-3414.1460	-3414.1469	-3414.1478	-3414.1488	-3414.1520	-3414.1552	-3414.1637	-3414.1834	
Specific heat (p=const)	2.8630	2.8630	2.8630	2.8630	2.8630	2.8629	2.8629	2.8629	2.8627	
Specific heat (V=const)	2.5105	2.5105	2.5105	2.5105	2.5105	2.5105	2.5105	2.5104	2.5103	
Gamma	1.1404	1.1404	1.1404	1.1404	1.1404	1.1404	1.1404	1.1404	1.1404	
Isentropic exponent	1.1205	1.1205	1.1205	1.1205	1.1205	1.1205	1.1205	1.1205	1.1205	
Gas constant	0.2113	0.2113	0.2113	0.2113	0.2113	0.2113	0.2113	0.2113	0.2113	

**Figure 34: Calculated coolant passage geometry cross section at nozzle throat**

The outputs may be exported as a text file and imported into Excel where this model is developed. In addition to the RPA gas outputs, the nozzle geometry was defined for the gas flow path as well as the cooling geometry at each slice. The gas convection coefficient is calculated using Equation 8 with an initial guess of the gas-side wall temperature and assuming one-

dimensional flow. The heat flux by gas convection is then calculated with Equation 6. The liquid wall temperature through the stainless steel nozzle wall is calculated using Equation 7 for conduction with the heat flux obtained from Equation 6 for the steady state assumption. Then the liquid convective heat transfer coefficient may be calculated using Equation 9 of the liquid temperature from the previous segment, assuming laminar cooling flow due to the low Reynolds numbers of the supplied water. Now, to assume steady-state heat transfer to the liquid, this liquid convective heat flux will be set equal to the heat flux imparted from the hot gas. The gas-side wall temperature guess is iterated upon until heat flux for both the convective gas and convective cooling liquid are equal. A schematic of this process is illustrated below in Figure 35. The green-highlighted heat fluxes are desired to be set equal, at which point the gas-side wall temperature, highlighted in purple, is assumed correct.

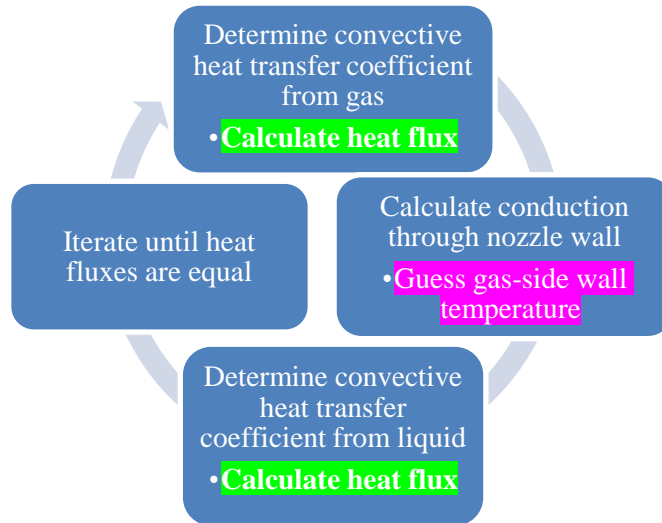


**Figure 35: Analytical model iteration schematic**

At this point, the cooling liquid properties are fixed for that nozzle slice. To determine the liquid temperature increase to the next slice, the following equation is utilized where  $\dot{m}$  is the liquid flow rate, and  $x_i$  is the slice length of the nozzle segment:

$$T_{l(i+1)} = T_{li} + \frac{1}{\dot{m}c_{pl}} \int_{x_i}^{x_{i+1}} \dot{q} dA_i$$

The integral assigns the 2D area of the cooling segment which is the slice length  $x_i$  multiplied by the coolant channel width. The process is repeated from the nozzle exit upstream to the coolant exit and nozzle inlet, continuously guessing the gas-side wall temperature until convergence is reached for each slice and updating fluid properties at each step. Many intermediate calculations are necessary to solve for the convective heat transfer coefficients including calculation of Reynolds number and variable flow areas that stem from the predefined nozzle flow paths. The results for these calculations are discussed in the following chapter.

## CHAPTER IV

### RESULTS

The experimental data collected included pressure and thrust measurements during the motor burns, as well as temperature measurements of the water coolant used and nozzle surface temperatures before, during, and after the rocket motor burn. In this chapter, a brief coverage of the motor performance precedes the thermal data measurements. A discussion of the nozzle's cooling passage segmentation influence on the temperatures recorded follows, as well as visual observations to assist in explaining the collected data.

The analytical model's results are presented and compared to experimental data along with discussion. The model's results themselves are also compared to each nozzle configuration for segmented cooling passages. Finally, an overall assessment of this cooling strategy is made for being applied to small satellite propulsion systems.

#### 4.1 Motor Performance

Pressure and thrust measurements were obtained during each of the 4 motor burns as confirmation of reasonable burn times and to check for anomalies during the burn. The obtained thrust data suffers from a large amount of noise due to the low thrust values at less than

5lbf (22N), but the internal pressure data is more useful. The chamber pressure readings for all 4 motors are plotted below in Figure 36.

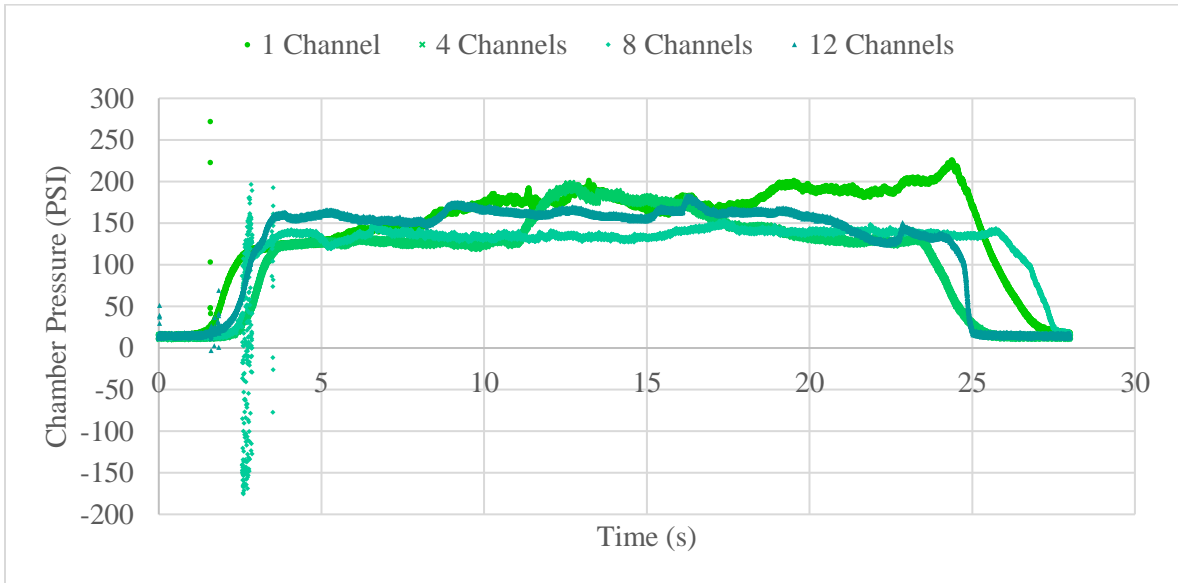


**Figure 36: Combined pressure data for 4 firings**

From the above figure, each motor reaches its near-steady state chamber pressure between 3 and 4 seconds after receiving the ignition command which occurs at time equal 0 seconds. The average pressure and standard deviation for each is tabulated below in Table 7.

**Table 7: Average chamber pressure and standard deviation for 4 firings**

Test	Average Pressure	Average Pressure	Standard Deviation
	(PSI)	(MPa)	(PSI/MPa)
1 Channel	146.4	1.01	55.53 / 0.38
4 Channels	112.2	0.77	56.11 / 0.39
8 Channels	119.6	0.82	41.80 / 0.29
12 Channels	126.7	0.87	56.45 / 0.39

The ranges of pressure align with the expected design condition of 160PSI (1.1MPa). Burnout occurred between 25 and 28 seconds following the ignition command. This variation in burnout time affects the average mass flow rate somewhat, and these values are tabulated in Table 8. The average mass flow rates fall within 0.042oz/s (1.2g/s) of each other. These data indicate consistent tests as far as performance is concerned. A more in-depth analysis of repeatability is discussed in Chapter V.

**Table 8: Propellant burn time and mass flow rate during motor burn**

Nozzle Configuration	Burn time (s)	Average propellant mass flow rate	
		(oz/s)	(g/s)
1 Channel	26.5	0.27 ± 0.001	7.6 ± 0.038
4 Channels	23.5	0.30 ± 0.001	8.6 ± 0.043
8 Channels	25.5	0.28 ± 0.001	7.9 ± 0.039
12 Channels	23	0.31 ± 0.001	8.8 ± 0.043

#### 4.2 Thermal Evaluation

This section will cover the temperature data for each nozzle configuration as a result of hotfire testing. Two types of temperatures were measured: cooling water temperature flowing through the nozzle and external surface temperature at the nozzle exit. The tests were conducted in order of increasing passage numbers: 1, 4, 8, and 12. Video was recorded of each test, and visual observation was critical to diagnosing the temperatures observed. The temperature data for the 1 channel nozzle are shown in Figure 37. Because this plot covers the 15 minutes after motor ignition, 3 vertical, colored lines describe primary events taking place following ignition. The black vertical line at time equal 0 is for ignition, the red line is for motor burnout, and the blue line is for cooling water shutoff.

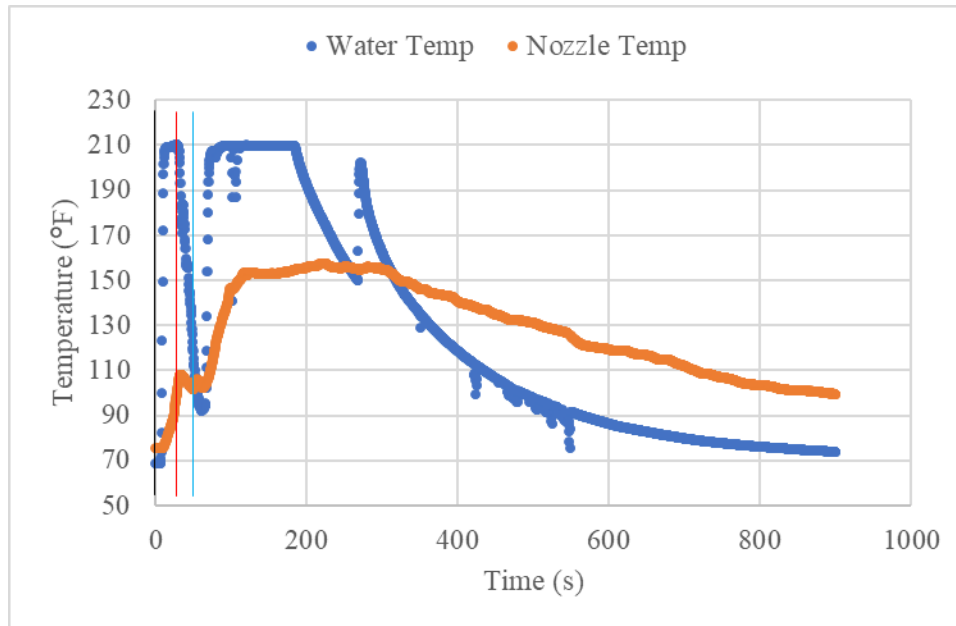


**Figure 37: Overall temperature plot – 1 channel**

There is a rapid water temperature increase immediately following motor ignition that appears to begin extracting heat from the nozzle right away. After burnout, but before the water flow is shut off, there is a rapid drop in water temperature to under 100°F, but as soon as the water is shut off, it climbs right back up to its maximum temperature of 209.5F. From video review, after the water is shut off, an enclosure of water surrounds the hose exit, perhaps due to cohesion. A frame from the video shown below in Figure 38 indicates this, and the temperature increase could be from the resulting air trapped inside the hose that heats with the nozzle temperature still climbing. This would indicate the high sustained thermocouple reading.



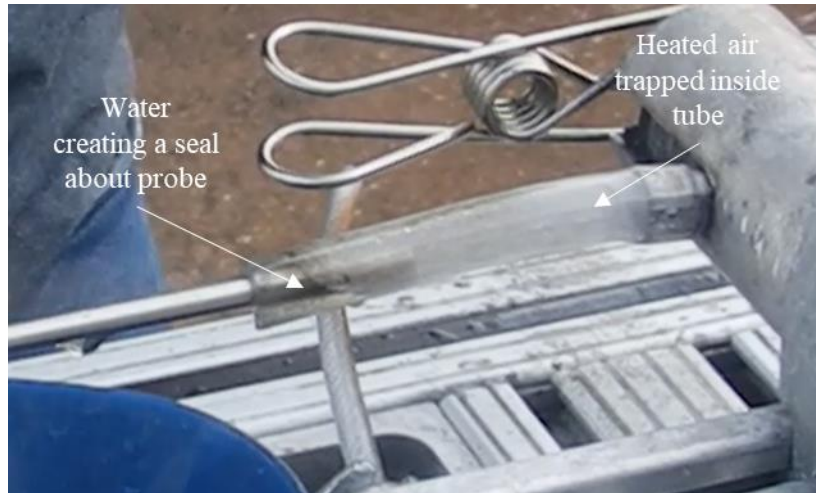


**Figure 38: Water behavior after flow shutoff**

For tests of the nozzles with 4 and 8 channels, the water flow behavior was different. From video, there was a noticeable issue with maintaining constant flow throughout the motor burn. The water at the nozzle inlet seemed to flow back and forth without entering the nozzle itself. When it did rock back to the inlet and contacted the hot nozzle, a spurt of steam would emit through the exit. The consequence of this is that water was not continuously flowing during the motor burn and impacted the temperatures recorded. The thermocouple data is shown in Figure 39 and Figure 40.

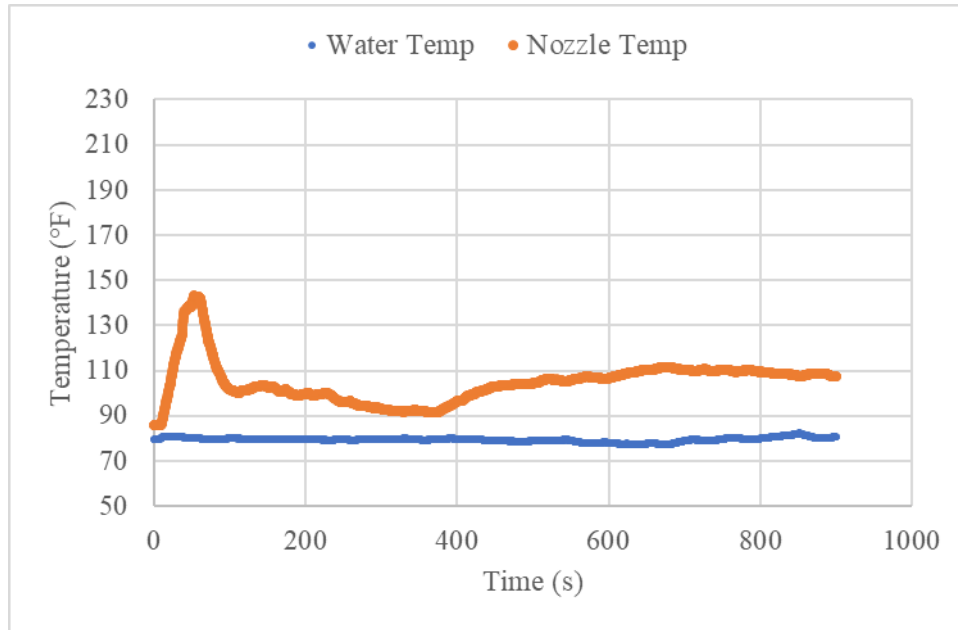


**Figure 39: Overall temperature plot for 4 channels**

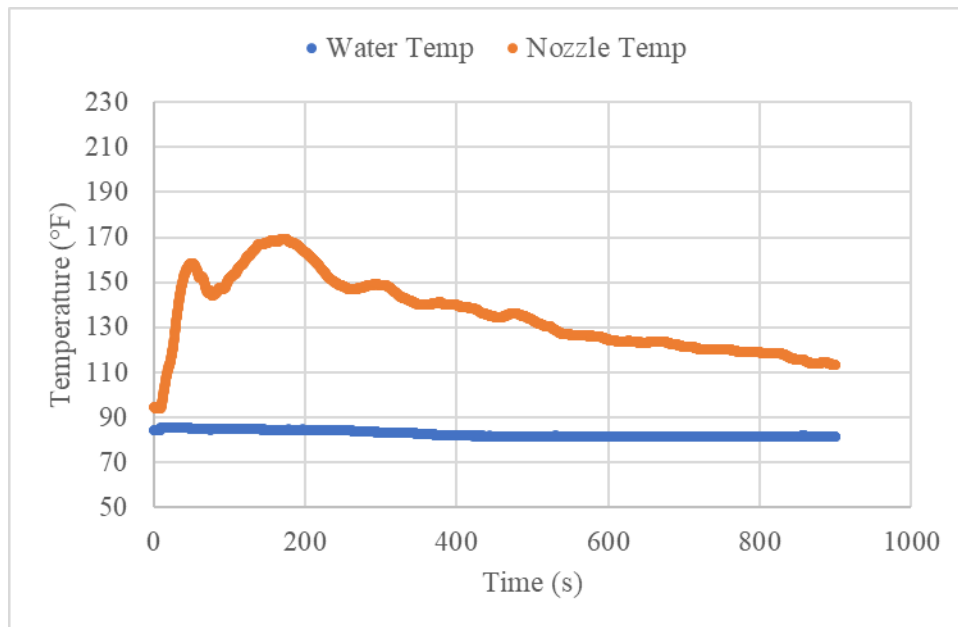


**Figure 40: Overall temperature plot for 8 channels**

Both of the above figures are the result of inconsistent water flow through the nozzle during firing. Because there was minimal moving water or air, the thermocouple read near constant values during the entire sampling period. The reason water was unable to flow through is speculated to be due to small gaps between the additively-manufactured layers of the wall

separating the gas flow path from the cooling water flow channel. While these gaps were not large enough for the exhaust gas flow to enter the coolant flow passage, the pressure generated by the gas overcame the small head pressure being applied by the water tank depth. With enough pressure applied through the gaps in the printed wall, water was unable to push against that to enter and exit the nozzle from the other side. As a result, minimal flow through the coolant passage existed, and near constant cooling water temperature was sampled for the stationary air.

For the final nozzle containing 12 passages, slightly more water flow seems to have occurred than with the 4 and 8 channel nozzles. That temperature profile is shown below in Figure 41. This is more representative of the first firing with a coolant temperature drop between burnout but before water flow is shut off. Then after the water flow is closed off, the indicated coolant temperature rises again and features the same cohesive behavior that encases the thermocouple probe with enough water to warm up the trapped air. During the 15-minute cooldown period, the water temperature thermocouple drops below its initial temperature, possibly due to evaporation as the sun had come out by this point in the day during testing and was warming the surroundings.

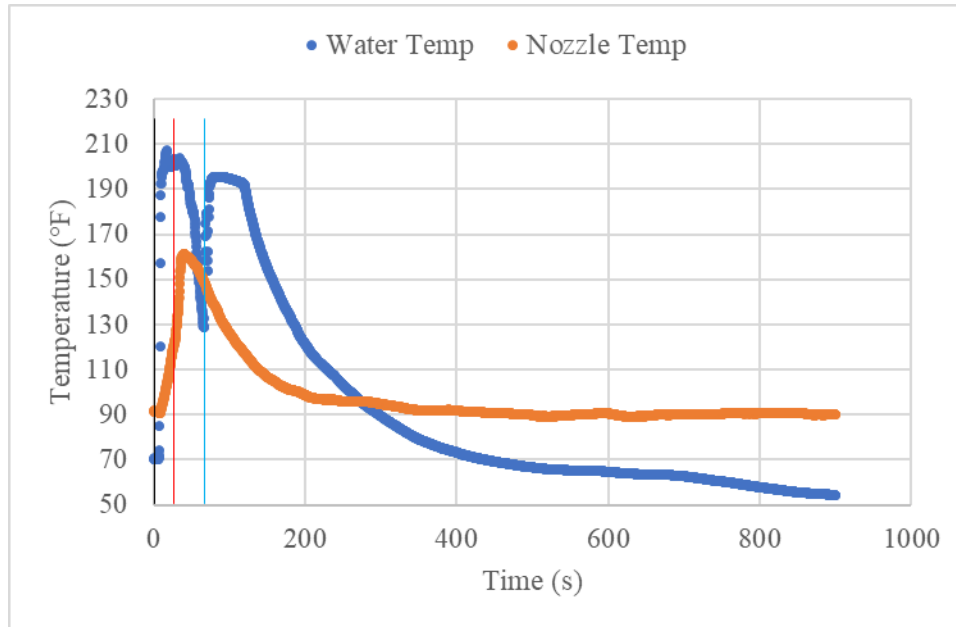


**Figure 41: Overall temperature plot for 12 channels**

On this final test, there was some sputtering due to fluctuating water flows, but the frequency with which that occurred was less than that on previous tests. An anomaly occurred in the final seconds of this test in that the aft thermal insulator failed and burn-through of the casing occurred. This is most likely due to the prolonged burn times, repeated use of this casing, and the observed behavior of a gravitational component associated with the exhaust gas and associated residue from the burned KNSB propellant. Figure 42 shows that at the end of a firing, much more of the propellant residue accumulates at the bottom of the casing due to gravity and could have contributed to the burn-through of the casing there at the bottom-most location.

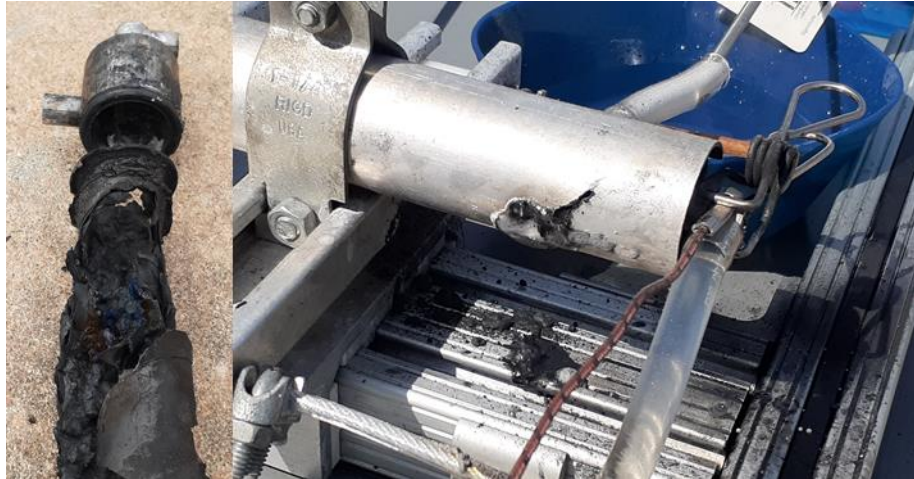


**Figure 42: KNSB residue accumulation (left) and eventual casing burn-through (right)**

Additional plots specifically of the burn time period are given in the appendix. For 1 and 12 channels, the water coolant response time is quite rapid, but the nozzle surface temperature takes much longer to heat and features slower transients that are still increasing for up to a minute or more following motor burnout.

#### *4.2.1 Leakage Between Nozzle Walls*

To further examine the observation of potential leakage between the printed wall layers, each nozzle was examined individually after firing. To test for gaps in the wall layer, leakage was observed in two ways: flowing water through the nozzle to visualize water leakage through the wall, and by submerging the nozzle underwater by blowing air through the cooling passage to observe any air bubbles that may emerge through the wall layers. The water leakage is shown below in Figure 43. Initially, there is water exiting the coolant exit only (as it should be), but then frame by frame, a droplet emerges, grows, and exits the exhaust gas flow passage where there should not be any water present. This was significant such that in an attempted subsequent firing, enough water leaked through to soak the front face of the KNSB propellant grain, rendering it impossible to ignite, and thereby preventing future firings with this nozzle. The remaining parts featured the same behavior with water flowing to areas that should have remained dry.

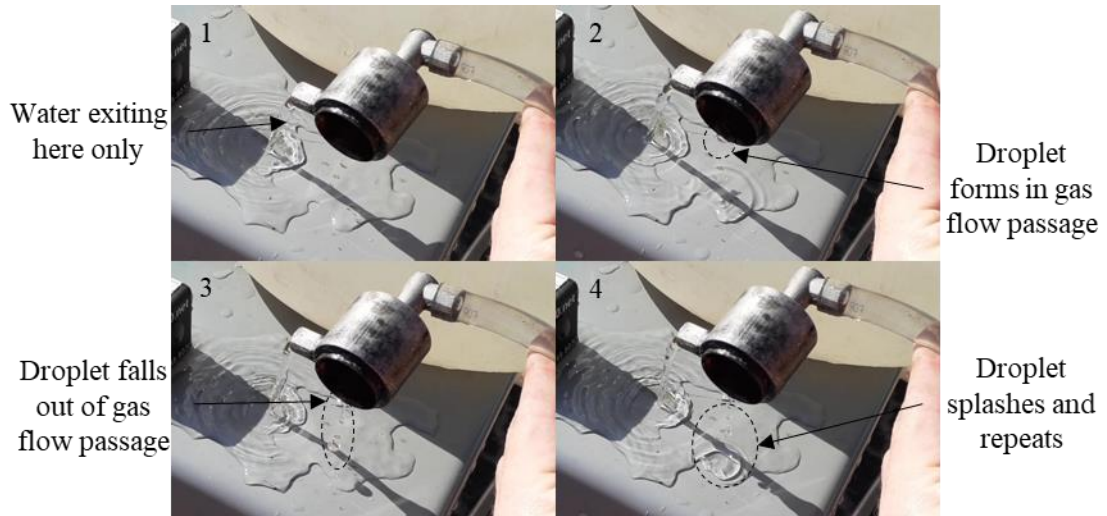


**Figure 43: Water leakage through gas flow passage**

Furthermore, each nozzle was also submerged underwater and air blown through the coolant passage to identify formation of air bubbles, thereby indicating a leak between the nozzle wall layers. A frame-by-frame figure is shown below in Figure 44. At first, there is no air bubble present, but then one forms in the bottom left quadrant near the nozzle throat, floats upwards, and exits the nozzle. Each of the remaining nozzles also exhibited this behavior.

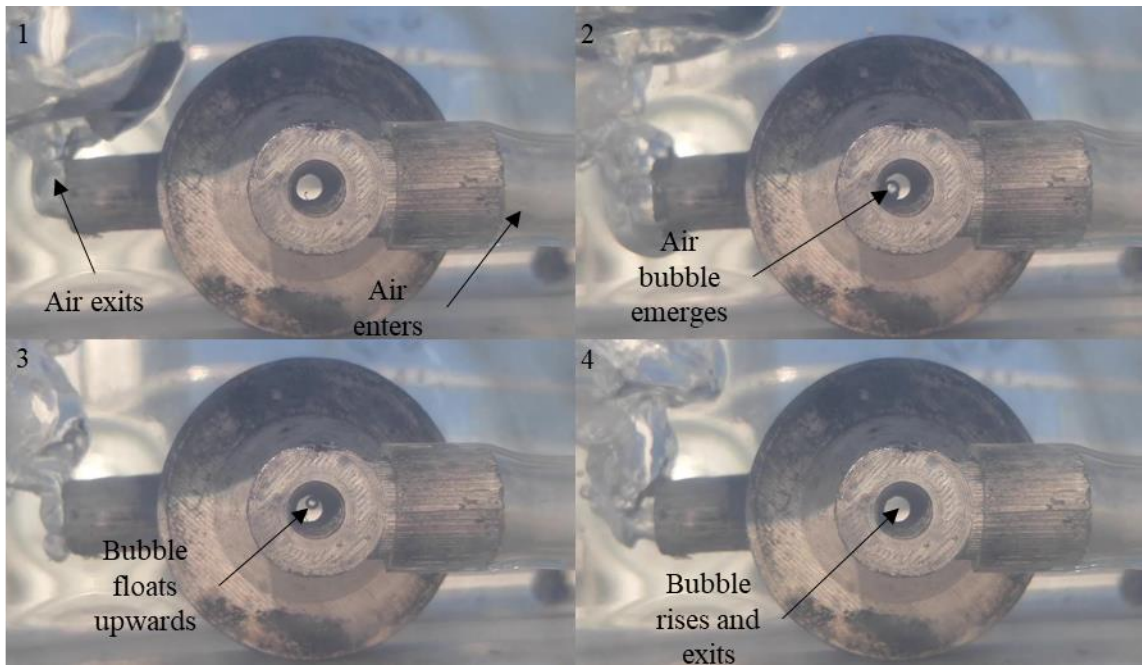


**Figure 44: Air bubble formation through nozzle wall indicating leakage**

Because no such leakage was observed prior to firing, the extended motor burn seems to have inflicted damage on these nozzles, forming the gaps or growing existing gaps between the 3D-printed layers. This could be a figment of the FDM-style printing technique that ADAM uses, or could be avoided with a thicker wall layer. Other powder-based printing methods may be more suitable for future tests.

#### 4.2.2 Influence of Segmented Cooling Passages

To study the effect of passage segmentation, the obtained temperatures during these firings are summarized and tabulated below in Table 9. For each nozzle configuration, the coolant temperatures were averaged, and the maximum value identified. Additionally, the surface temperature measurements were averaged, the maximum value listed, and finally the ending surface temperature to provide an indication of the cooling effect on the overall cool-down transient that occurs after motor burnout.

**Table 9: Summarized thermal data**

<b>Number of Cooling Channels</b>	<b>Maximum Coolant Temperature (°F)</b>	<b>Average Coolant Temperature (°F)</b>	<b>Maximum Surface Temperature (°F)</b>	<b>Average Surface Temperature (°F)</b>	<b>Ending Surface Temperature (°F)</b>
1	210.3	123.9	157.6	127.3	99.3
4	82.2	79	143.4	104.8	107.5
8	85.6	82.6	169.4	135.4	113.0
12	207.1	92.8	161.4	98.0	90.3

For the cooling flows, it was desired that the liquid temperature be maximized, so as to increase cooling effectiveness according to Equation 10. The maximum liquid temperature

achieved was for the single channel configuration, indicating the most favorable cooling geometry may be for this single channel, as it featured the highest temperature increase from the nozzle to the coolant.

The surface temperature is indicative of the thermal loads imparted through the hot gas flow path through the nozzle walls and coolant passage. It is desirable that the surface temperature be minimized, thereby indicating a greater portion of the thermal load was applied to the cooling flow. While the single channel nozzle exhibited the greatest liquid temperature increase, it measured only the third coolest average surface temperature compared to the other nozzle configurations. According to the data from Table 9, the 8-channel configuration resulted in the highest maximum, average, and ending surface temperatures. This could be indicative that more segmented channels corresponded to hindering cooling effectiveness, but it must also be remembered that the 4 and 8 channel configurations suffered from inconsistent cooling flow during the burn. Had the water flow been maintained throughout, upward or downward trends for these data may have been more identifiable.

The presence of a steady cooling flow did speed up the cool-down transient after a firing, and heat was certainly extracted by the cooling flow as temperature differences from the nozzle exit to inlet were over 100°F. A closer examination of these deltas are discussed in the following section. It appears these tests were hampered by slight leakage between the printed layers that prevented a consistent water flow. To examine further examine the impact of cooling channel segmentation and improve understanding of segmentation influence, the analytical model will address this area more precisely by calculating heat transfer as a function of the variable flow areas that exist for the segmented channels. Trends for increasing channel segmentation will be observed and compared to the obtained experimental data. Lastly, to calculate cooling effectiveness from the experimental data, the analytical model results will be partially used to estimate the wall and gas temperatures as those measurements were not obtained in the



experiment. Using those analytical values, cooling effectiveness will be calculated with the measured liquid temperature.

### 4.3 Analytical Model Results

Results from this analytical model include gas and liquid temperatures and other fluid properties for the varying conditions throughout the nozzle. The primary parameters of interest are the convective heat transfer coefficient for the gas and liquid, the overall heat flux throughout the nozzle, and the liquid coolant temperature increase as a result of the hot nozzle. A condensed snapshot of the spreadsheet model calculations is shown below in Figure 45. Detailed tables of these results are given in the appendix.

Station	Area Ratio	Name	$A_{chamber}$ m <sup>2</sup>	$D_{h, gas}$ m	$\mu_g$ kg/m*s	$c_p$ J/kg*K	$Pr_g$	$T_\infty$ K	$M_\infty$
26	N/A	Coolant Exit							
25	78	"Injector"	0.00057876	0.02715	6.10E-05	1874	0.6675	1560.94	0.01
24	78	Nozzle Inlet	0.00057876	0.02715	6.098E-05	1874	0.6674	1560.93	0.0076
23	70.3		0.000521626	0.02578	6.098E-05	1874	0.6674	1560.93	0.0089
22	61.74		0.000458144	0.02416	6.098E-05	1874	0.6627	1560.93	0.0101
21	53.19		0.000394662	0.02242	6.098E-05	1874	0.6679	1560.92	0.0114
20	44.63		0.000331179	0.02054	6.098E-05	1874	0.6675	1560.92	0.0146
19	36.08		0.000267697	0.01847	6.098E-05	1874	0.6674	1560.91	0.0172
18	27.52		0.000204215	0.01613	6.098E-05	1874	0.6676	1560.89	0.0227
17	18.97		0.000140733	0.01339	6.098E-05	1874	0.6675	1560.85	0.032
16	10.41		7.72504E-05	0.00992	6.098E-05	1874	0.6674	1560.66	0.0575
15	1.86		1.37682E-05	0.00419	6.071E-05	1874	0.6645	1551.17	0.3418
14	1	Throat	0.00000742	0.00307	5.871E-05	1871	0.664	1480.69	1
13	1.18		8.73277E-06	0.00334	5.635E-05	1865	0.6598	1398.85	1.4529
12	1.35		1.00455E-05	0.00358	5.528E-05	1860	0.6565	1361.88	1.6255
11	1.53		1.13583E-05	0.00380	5.44E-05	1855	0.6556	1331.54	1.7585
10	1.71		1.26711E-05	0.00402	5.366E-05	1850	0.6542	1306.43	1.8642
9	1.88		1.39838E-05	0.00422	5.306E-05	1846	0.6528	1286	1.9479
8	2.06		1.52966E-05	0.00441	5.25E-05	1842	0.6515	1266.98	2.0242
7	2.24		1.66094E-05	0.00460	5.199E-05	1839	0.6502	1250.01	2.0913
6	2.42		1.79222E-05	0.00478	5.154E-05	1835	0.6489	1234.74	2.1511
5	2.59		1.92349E-05	0.00495	5.11E-05	1832	0.6479	1221.59	2.2021
4	2.77		2.05477E-05	0.00512	5.076E-05	1829	0.6467	1208.8	2.2515
3	2.95		2.18605E-05	0.00528	5.058E-05	1827	0.6462	1202.76	2.2885
2	3.12		2.31732E-05	0.00543	5.042E-05	1826	0.6457	1197.52	2.3212
1	3.3	Nozzle Exit	0.000024486	0.00559	5.026E-05	1825	0.6452	1192.19	2.3532

**Figure 45: Analytical spreadsheet model snapshot**

To obtain an understanding of how these parameters vary throughout each nozzle slice, the values at each slice are plotted in the following figures. Figure 46 shows the variation of heat transfer coefficient with axial location downstream through the nozzle. The peak value over

50000W/m<sup>2</sup>K occurs at the nozzle throat. The heat transfer coefficient ramps up from 0 at the nozzle inlet due to the low subsonic velocity of the gas before it accelerates through the throat.

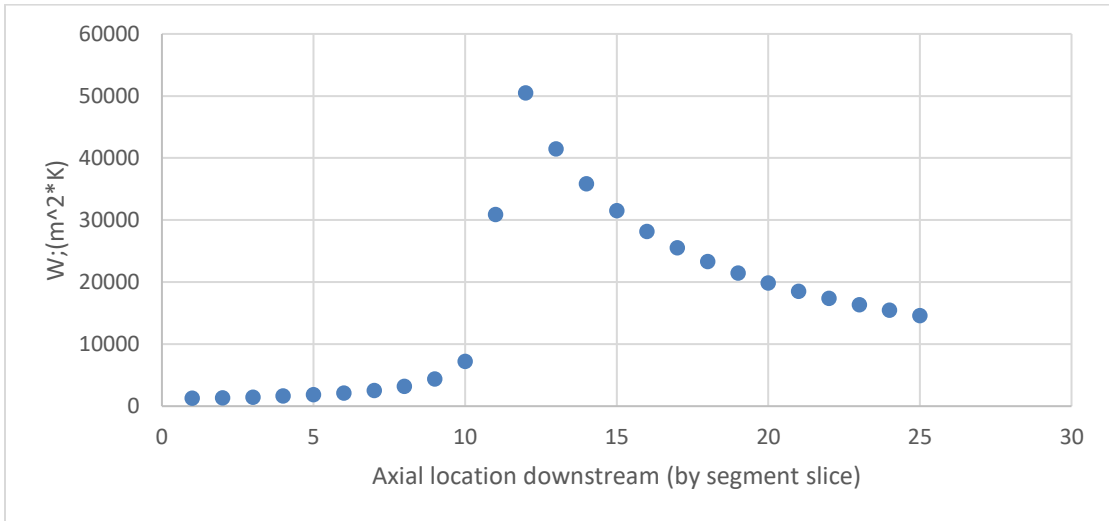


**Figure 46: Gas convection heat transfer coefficient for 1 passage**

A similar trend exists in Figure 47 for heat flux, with the greatest magnitude occurring at the throat. Likewise, the least amount of heat flux exists at the nozzle inlet in which the exhaust gas has low velocity.

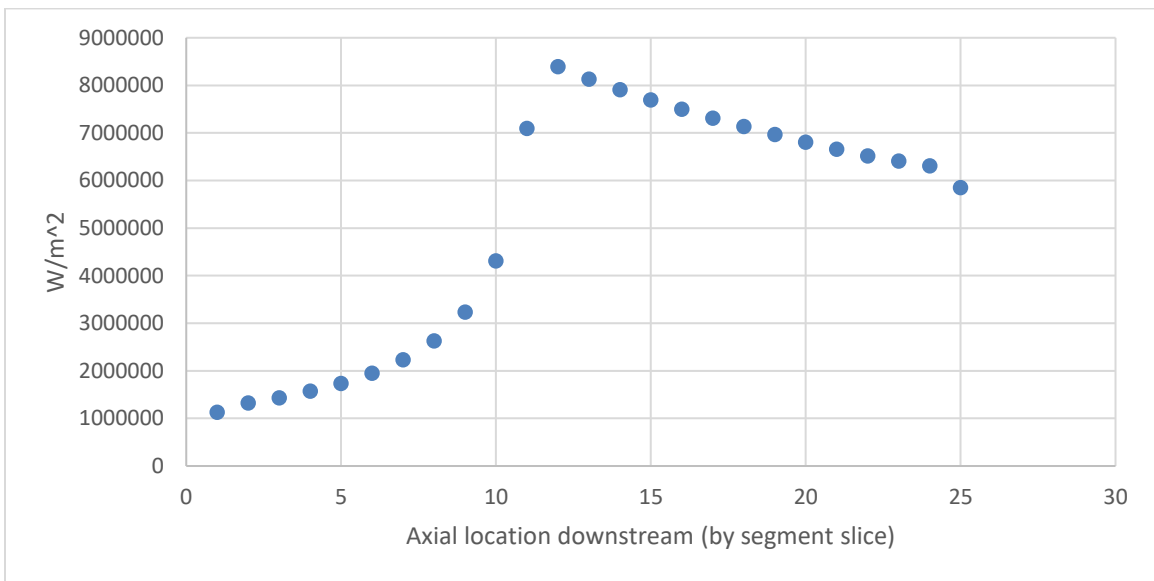


**Figure 47: Heat flux for 1 passage**

Finally, a plot of the cooling liquid heat transfer coefficient is plotted below in Figure 48. It follows similar behavior as the gas coefficient and heat flux, but less change from slice to slice in the diverging nozzle section downstream of the throat. This is due to the lower heat flux occurring downstream of the throat where the greatest heat transfer exists.

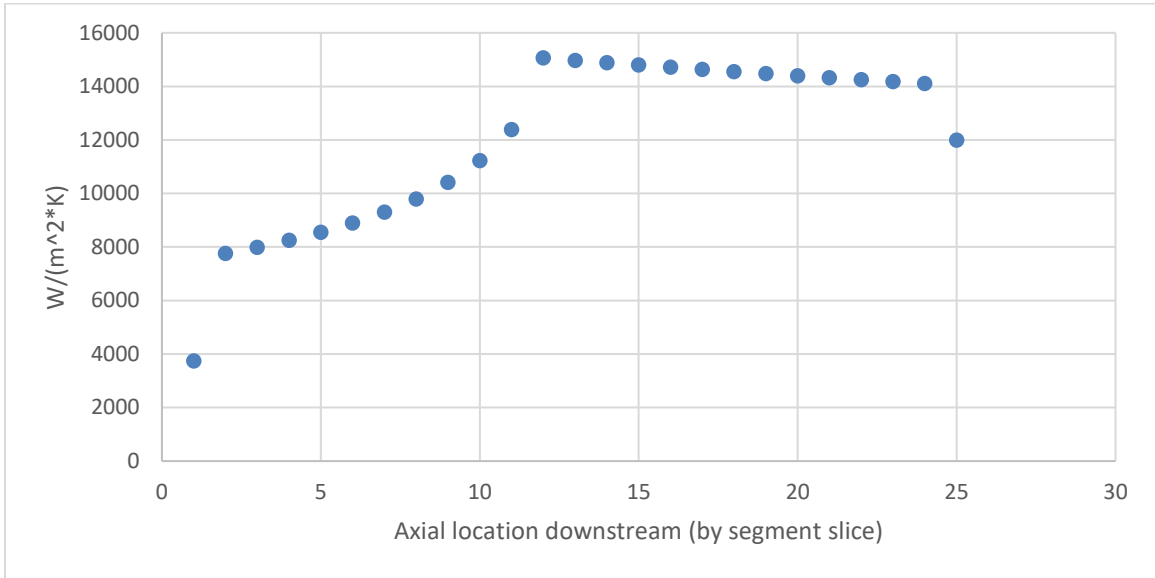


**Figure 48: Liquid cooling convective heat transfer coefficient for 1 passage**

The primary nozzle locations of interest: exhaust gas nozzle inlet upstream, the throat, and nozzle exit have their respective heat transfer parameters tabulated below in Table 10. There is a far greater heat transfer coefficient for the gas due to the high velocities, despite a near-identical mass flow rate between the gas and cooling water.

**Table 10: Heat transfer coefficients at 3 nozzle locations**

# of Channels	Inlet	Throat	Exit	Inlet	Throat	Exit
	$h_g$ (W/m <sup>2</sup> K)			$h_l$ (W/m <sup>2</sup> K)		
1 Channel	1325	50473	14585	7755	15053	11988
4 Channels	1299	50183	14309	5054	10792	8082
8 Channels	1283	50094	14196	4066	9746	6880
12 Channels	1275	50099	14153	3637	9794	6467

These values for liquid heat transfer coefficient are graphed below in Figure 49. This aligns with Figure 48 that the largest heat transfer occurs at the nozzle throat.

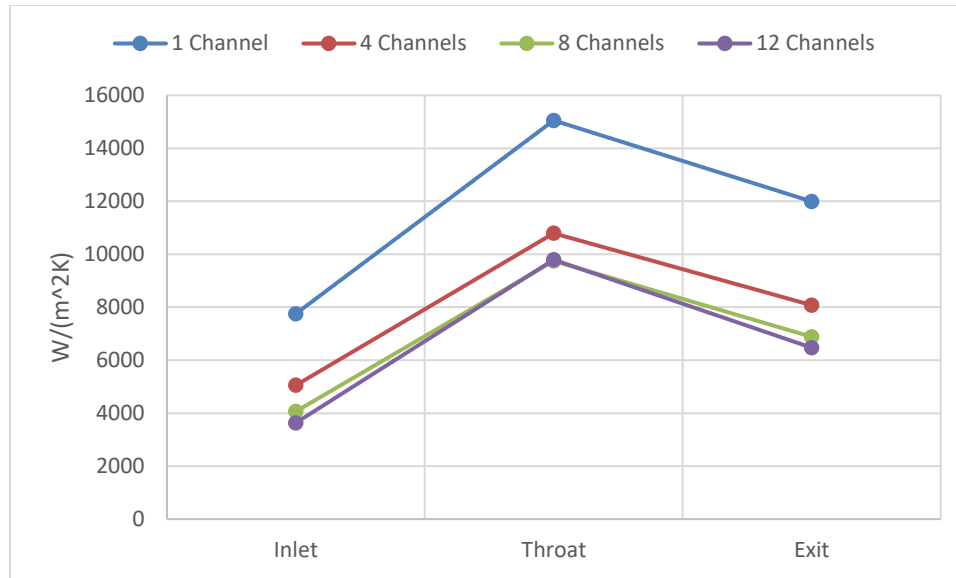


**Figure 49: Liquid heat transfer coefficient for all nozzle configurations**

As for the nozzle heat flux, these values are tabulated in Table 11. There is a consistent trend that with additional cooling channels, and therefore increased segmentation, less heat flux occurs with increasing number of channels. These are also plotted in Figure 50, and the same trends exist for heat flux as with liquid convection coefficient, in which the highest heat transfer occurring at the throat.

**Table 11: Overall heat flux at 3 nozzle locations**

Channel #	Inlet	Throat	Exit
	Heat Flux (W/m <sup>2</sup> )		
1 Channel	1.33E+06	8.39E+06	5.85E+06
4 Channels	1.22E+06	7.15E+06	4.91E+06
8 Channels	1.16E+06	6.77E+06	4.52E+06
12 Channels	1.12E+06	6.79E+06	4.38E+06

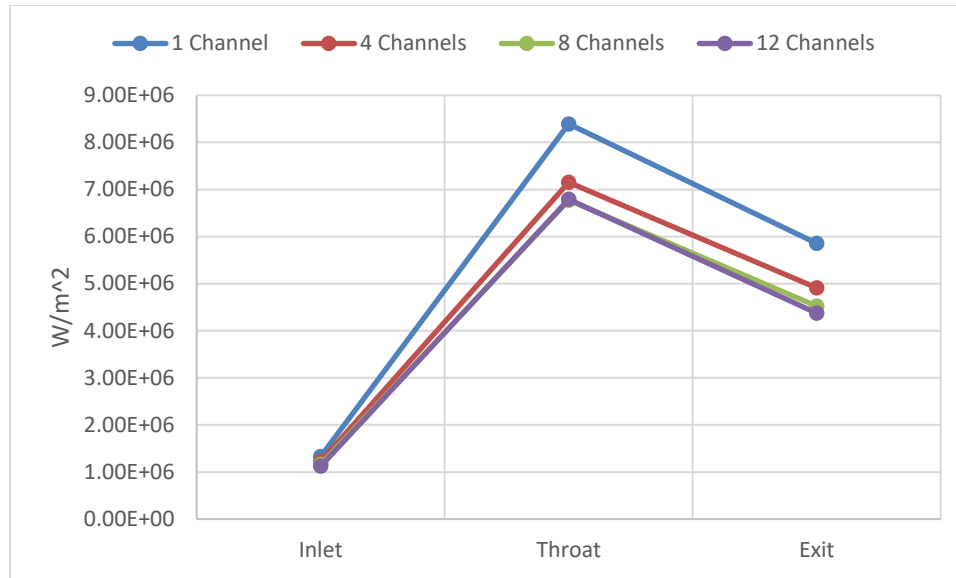


**Figure 50: Heat flux for various nozzle configurations**

For comparing the analytical model to the observed experimental results, the cooling liquid temperature rise is tabulated below in

Table *12*. This temperature rise is the final liquid temperature slice for the model and the measured temperature from the thermocouple probe experimentally. The percent differences are large, at more than 130% for all configurations. This is indicative that the analytical model does not provide an accurate representation of the magnitudes of temperature increase within the nozzle. This is likely due to assumptions made for the model as well as improper convective heat transfer correlations for the small scale, low Reynolds numbers present in this test setup. While the magnitudes of these temperatures do not align well, trends for varying the number of cooling channels can still be applied and studied, along with their relationship to cooling effectiveness.

**Table 12: Analytical model comparison to analytical results**

<b>Channel #</b>	<b><math>\Delta T</math> Liquid Analytical (°F)</b>	<b><math>\Delta T</math> Experimental (°F)</b>	<b>Percent Difference</b>
1 Channel	15.8	141.5	160%
4 Channels	13.7	2.6	-135%
8 Channels	12.9	1.4	-162%
12 Channels	12.8	136.5	166%

To analyze the temperature change in the liquid cooling water and identify the cooling effectiveness of each nozzle configuration using the analytical model developed, the final liquid temperature is subtracted from the initial temperature of 66°F (292K). Using Equation 10, with the overall averaged recovery temperature as the gas temperature, averaged gas-side wall temperature minus the liquid-side wall temperature yielding the metal temperature, and the averaged cooling water temperature, the following calculations for cooling effectiveness are shown below in Table 13. The experimental data for cooling liquid temperature are also applied to determine cooling effectiveness for the obtained test data.

**Table 13: Liquid temperature change and averaged cooling effectiveness**

<b>Channel #</b>	<b><math>\Delta T</math> liquid (°F)</b>	<b><math>\Delta T</math> liquid (K)</b>	<b>Cooling Effectiveness</b>	<b>Cooling Effectiveness Experimental</b>
1 Channel	15.76	8.75	55.2%	56.9%
4 Channels	13.73	7.63	49.5%	49.7%
8 Channels	12.94	7.19	47.1%	47.3%
12 Channels	12.77	7.10	46.4%	47.8%

As with the largest heat flux occurring for the single cooling channel nozzle configuration, cooling effectiveness is maximized for the coaxial shell configuration (single cooling passage). There is decreasing effectiveness with the inclusion of additional cooling passage segmentation. The liquid temperature difference is maximized for a single cooling passage by extracting the most heat and is therefore the most effective for regenerative cooling according to this model.

According to Heister, this model should yield a coolant temperature change in the jacket of 50-100K [26], but for this model, temperature increases of less than 10K were present. An explanation for this phenomenon is likely the scale of this setup. For such small nozzle geometry, cooling passages, low pressures, and low Reynolds numbers of the cooling flow in particular, less heat transfer to the cooling water results, and it might be expected that smaller temperature changes would be observed.

Other complications of the model include the short thrust chamber/nozzle length. The diameter of the inlet and exit hose made up 32% of the coolant passage length along the nozzle and was necessary as a manifold for distributing the coolant around the circular hardware. Equation 9 is also has several criteria for recommended use including the viscosity ratio between 0.0044 and 9.75 but varies between 30 and 36 for this study due to assumed saturated steam for evaluating viscosity at the high wall temperature. An improved Nusselt number correlation would best suited for determining the water liquid temperature. Ultimately, that is why such low cooling water liquid temperatures were calculated from the analytical model are the result of a low heat transfer coefficient for the low Reynolds number water flow.

#### 4.4 Summary of Experimental and Analytical Results

In this section, experimental results were presented and discussed. Issues existed with supplying constant cooling water through the nozzles, possibly due to leakage between the



printed wall layers. Analytical model results were also discussed. While poor agreement existed between the amount of cooling liquid temperature increase, evaluation of the influence of cooling passages was highlighted for both the experimental and analytical data. It was found that with fewer cooling passages, and therefore less segmentation, improved cooling effectiveness is demonstrated.

Summarily, regenerative cooling on the scale of small satellite thrusters appears feasible due to the thermal loads extracted by means of a cooling flow, and additive manufacturing is applicable, but improved wall design or other AM techniques are necessary to prevent gaps between printed layers. Cooling effectiveness is maximized for a single, annular flow passage extending the length of the thrust chamber and nozzle.

## CHAPTER V

### UNCERTAINTY ANALYSIS

During development of the KNSB gas generator, performance of the solid propellant itself was evaluated to validate the predicted simulations in MotorSim. It is critical that the KNSB exhaust mass flow rate closely match the designed 10g/s, burn times are consistent, and that overall performance be repeatable between propellant grains. Utilizing the portable 500lb thrust stand at Oklahoma State University [34], two 6in (15.2cm) long endburning propellant grains were fired, one of which shown in Figure 51. Internal chamber pressure and thrust were measured throughout.



**Figure 51: Gas generator performance validation test**

The trial setup on the stand is shown in Figure 52. Chamber pressure readings are obtained through a pressure transducer and thrust is collected via load cell at a sample rate of 1000Hz. Both grains were measured to be 6in (15.2cm) long and weigh 0.45lb (202g).

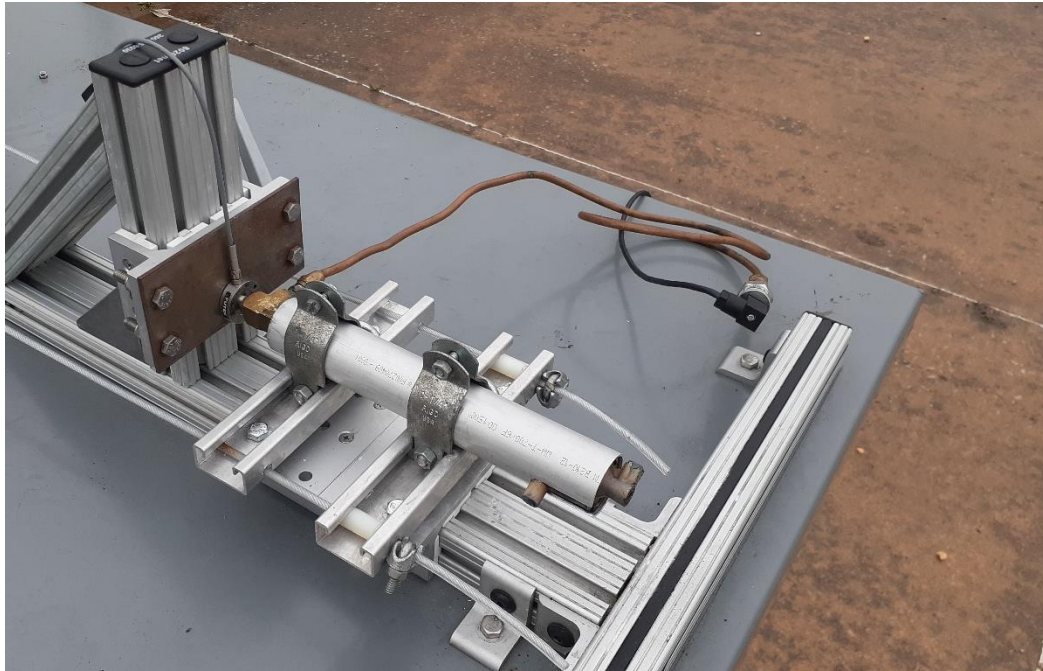


**Figure 52: Instrumented motor assembly for repeatability testing**

Two such motors were fired to compare total impulse, burn time, and the variability between each. According to NFPA 1125, high-power rocket motors require only two test firings for commercial certification purposes, and for this reason other test firings are not necessary should these two motors reflect similar performance parameters. The thrust for both motors is plotted in Figure 53. The noise is most likely attributed to the very low thrust produced by this motor. The test stand's load cell is rated to 500lbf (2.2kN), so for these motors operating at just 0.2% of that, signal accuracy is hindered. However, as thrust is not a critical assessment of this gas generator, the data obtained are still acceptable.

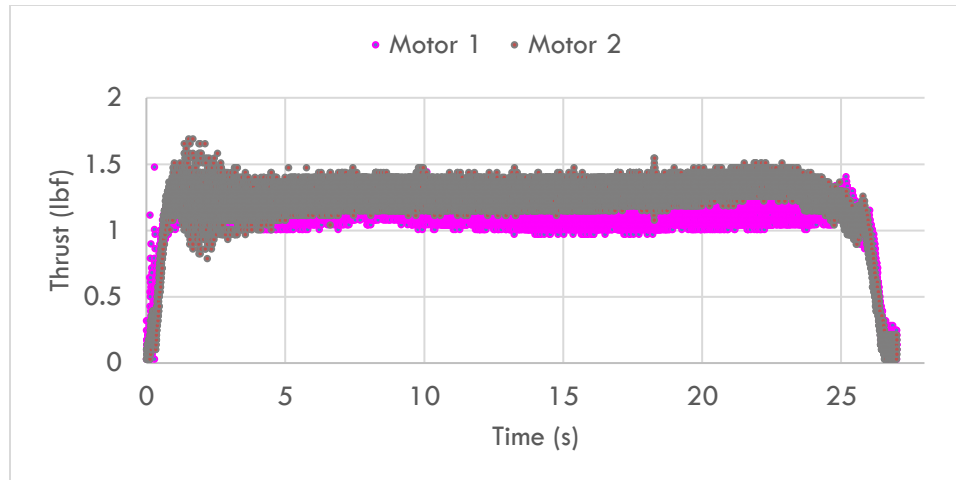


**Figure 53: Thrust data for repeatability study**

Additionally, chamber pressure was collected, and these data are shown in Figure 54.

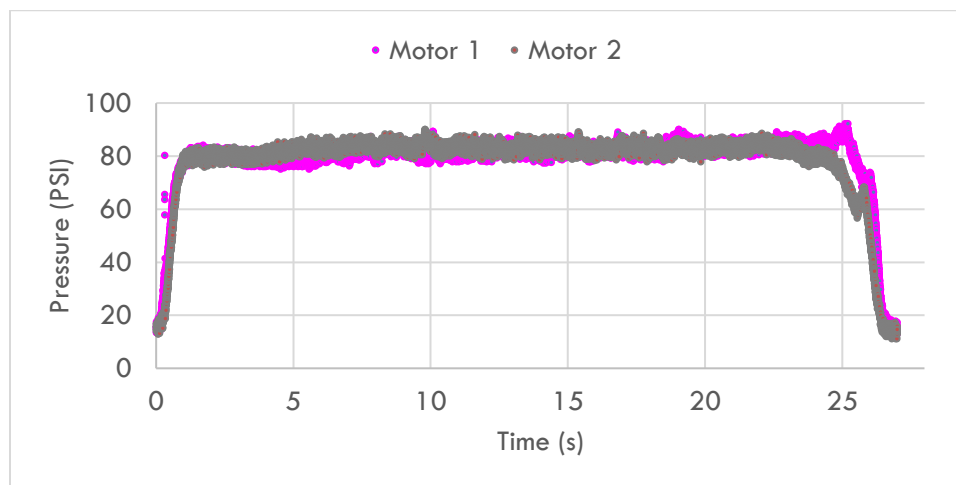


**Figure 54: Chamber pressure data for repeatability study**

From these data, performance parameters including total impulse and burn time are calculated and tabulated in

**Table 14.** The percent difference and standard deviation from the average of 3 firings for the simulation and each motor are also given.

**Table 14: Gas generator repeatability study**

Motor #	Total Impulse			Average Thrust			Average Pressure		
	Value (lbf-s)	% Diff	Std dev	Value (lbf)	% Diff	Std dev	Value (PSI)	% Diff	Std dev
1	30.01	9.38%	2.09	1.11	9.38%	0.08	79.06	0.97%	0.54
2	32.96			1.22			78.3		
Motor Sim	53.2	56.1%	12.62	2.93	100.5%	1.02	153	71.8%	0.67

These figures indicate there is good reliability between each propellant grain and gas generator system. Percent differences are below 10%, even with the noise and potentially inaccurate thrust readings (total impulse is calculated from thrust measurements). Chamber pressure similarity was excellent, with less than 1% difference between each firing. Burn time and mass flow were nearly indistinguishable as both samples burned in 27s, consuming an identical 0.45lb (202g) of propellant in that time to yield an exhaust gas mass flow rate of 7.5g/s. While short of the designed 10g/s, this figure still aligns well with other monopropellant thrusters as described in Table 4.

Unfortunately, there is large deviation from the data obtained versus the predicted performance from the Motor Sim simulation. This may be due to several factors including poor nozzle efficiency, humidity of ambient conditions during testing (potassium nitrate is hygroscopic), or losses from operating at relatively low chamber pressures and therefore a low burn rate, which may be poorly predicted by the simulation.

While the simulation did not align with the data collected, it is of greater importance that each propellant grain perform similarly to the others, and this is achieved and confirmed by these tests. With a reliable gas generator design established, only one firing per nozzle configuration is necessary, thus improving safety and minimizing the resources necessary for each test.

## CHAPTER VI

### CONCLUSIONS

#### 6.1 Summary of Experiments and Results

A rocket nozzle on the scale of a 22N small satellite thruster was designed, additively-manufactured, and hot-fire tested with a solid propellant gas generator. Water was used as a coolant to simulate regenerative cooling during the motor burn. Coolant temperatures were measured at the exit to determine the temperature rise and calculate the heat extracted during the tests. Nozzle exit surface temperature was also measured to compare how cooling flow contributed to reducing the high nozzle temperatures externally.

Four nozzle configurations were tested that contained identical converging-diverging geometry but varied in the number of segmented cooling channels between 1 and 12 passages, thereby also reducing the flow area, particularly at the throat and diverging regions. Each nozzle was fired once but was determined that some leakage between the nozzle wall prevented cooling water from being supplied steadily during the whole motor burn for three of the nozzle configurations. To further study the effect of segmented channels, an analytical model was created to compare to the measured data and calculate thermal loads resulting from the solid propellant exhaust gases.

It was determined that for increasing segmentation of the cooling passage, and therefore reduction in flow area, reduced cooling effectiveness resulted. A nozzle with a single cooling passage extracted the greatest thermal loads from the nozzle with a cooling effectiveness of 55% whereas 12 passages resulted in just 46%. The analytical model yielded much lower coolant temperature increases compared to experimental findings, but this is likely due to the convective heat transfer coefficient correlations that are suitable for larger rocket engines but suffer at the scale of these types of propulsion systems.

From this study, it can be concluded that regenerative cooling at this scale is feasible and is enabled by additive manufacturing for small satellite thrusters, but further research is necessary to better characterize heat transfer at this scale. For a developed green monopropellant system, the elevated liquid temperature will augment propellant inlet temperature to the catalyst bed thereby reducing power requirements necessary for ignition. Furthermore, the heat extracted could lower the thruster wall material to below the glass transition temperature of plain carbon steel or aluminum, reducing cost associated with thruster hardware.

## 6.2 Recommendations for Future Work

It is recommended that this scale of regenerative cooling jacket be designed and integrated for use with an existing small satellite thruster utilizing green monopropellants throughout the tests. The solid propellant gas generator created hot, high-pressure gases at high velocity, but the solid particulates, lower combustion temperatures, and material compatibility are not well aligned with decomposition of liquid propellants. Additionally, the small expansion ratio used in this test is not representative of nozzles expanding to near-vacuum ambient conditions. The large bell nozzle will have different coolant flow characteristics and the exhaust gases will cool more as a result of larger expansion, thereby affecting heat transfer to the coolant flow.



An improved analytical model is also necessary that matches more closely the temperature increases observed experimentally. This tool could optimize the coolant passage flow geometry at this scale and be applied to thrusters above and below the 22N scale.

Many satellite thrusters utilize pulsed burns for reaction control or stabilization, and this study only examined long-duration burns. Pulsing may affect the pressure drop in the coolant passage and cooling effectiveness as the thrust chamber will radiate heat and cool in between burns.

Finally, other additive manufacturing techniques could be examined, in particular powder-bed and laser sintering methods that may reduce gaps between propellant layers. The resulting surface roughness should also be studied to understand what degree of pressure drop could be expected.

## REFERENCES

1. ppl4world, *ArduSat - Your Arduino Experiment in Space*. 2012: Kickstarter.
2. NASA/JPL, *MarCO (Mars Cube One)*, A.a.s.r.o.N.s.t.M.C.O.M.s.a.t.f.t.d. space., Editor. 2018: NASA Science Solar System Exploration.
3. SpaceX, *Stars and Starlink*, b.t.m.n.s.m.i.e.o.a. SpaceX says that efforts to darken one Starlink satellite resulted in a “notable reduction” in its brightness, Editor. 2020: The Space Review.
4. Space, A.D.a., *SES 12*, S. 12, Editor. 2018: Gunter's Space Page.
5. Stephen A. Whitmore, S.L.M., Zachary S. Spurrier, Sean D. Walker. *Development of a Power Efficient, Restartable, "Green" Propellant Thruster for Small Spacecraft and Satellites*. in *29th Annual AIAA/USU Conference on Small Satellites*. 2015.
6. Ronald A. Spores, R.M., Scott Kimbrel, Chris McLean, *GPIM AF-M315E Propulsion System*, in *49th AIAA/ASME/SAE/ASEE Joint Propulsion Conference and Exhibit*. 2013, AIAA.
7. George P. Sutton, O.B., *Rocket Propulsion Elements*. 7th ed. 2001, New York, NY: John Wiley & Sons.
8. Bill Doncaster, J.S., John Bradford, John Olds, *SpaceWorks' 2016 Nano/Microsatellite Market Forecast*, in *30th Annual AIAA/USU Conference on Small Satellites*. 2016, AIAA.
9. Henry, C. *SpaceX submits paperwork for 30,000 more Starlink satellites*. 2019.
10. Henry, C. *Amazon planning 3,236-satellite constellation for internet connectivity*. 2019.
11. Joyce Wong, H.R., Andrew Ketsdever, *Micropropulsion for Small Spacecraft: University Micro-/Nanosatellite as a Micropropulsion Testbed*. Progress in Astronautics and Aeronautics, ed. P. Zarchan. Vol. 187. 2000: AIAA.
12. John H. Schilling, R.A.S., Gregory G. Spanjers, *Micropropulsion for Small Spacecraft: Micropropulsion Options for the TechSat21 Space-Based Radar Flight*. Progress in Astronautics and Aeronautics, ed. P. Zarchan. Vol. 187. 2000: AIAA.
13. A. Chaalane, R.C., M. Houabes, R. Yahiaoui, A. Metatla, B. Ouari, N. Metatla, D. Mahi, A. Dkhissi, and D. Esteve. , *A MEMS-based solid propellant microthruster array for space and military applications*. Journal Of Physics: Conference Series, 2015. **660**.
14. Rocketdyne, A., *In-Space Propulsion Data Sheets*. 2019, Aerojet Rocketdyne.

15. Mohammad H. Naraghi, M.F. *A Simple Approach For Thermal Analysis of Regenerative Cooling of Rocket Engines*. in *2008 ASME International Mechanical Engineering Congress and Exposition*. 2008. Boston, Massachusetts, USA: ASME.
16. Yunus A. Cengel, A.J.G., *Heat and Mass Transfer Fundamentals and Applications*. McGraw Hill Education. 2015, New York: McGraw Hill Education.
17. Robert L. Sackheim, R.K.M., *Green Propulsion Advancement: Challenging the Maturity of Monopropellant Hydrazine*. *Journal of Propulsion and Power*, 2014. **30**(2): p. 265-276.
18. Robert K. Masse, M.A., Elizabeth Driscoll, Ronald A. Spores, Lynn A. Arrington, Steven J. Schneider, Thomas E. Vasek, *AF-M315E Propulsion System Advances & Improvements*, N.T.R. Server, Editor. 2017, NASA.
19. Aerospace, B., A.B.A.e.a.t.t.i.o.N.s.G.P.I.M.s.b.f.i.o.t.p. system., Editor. 2015.
20. Wilson, M.J., *Demonstration Testing of a Long-Life 5-Lbf (22-N) MR-106L Monopropellant Hydrazine Rocket Engine Assembly*, in *41st AIAA/ASME/SAE/ASEE Joint Propulsion Conference & Exhibit*. 2005, AIAA.
21. McGee, A., *Hot-Fire Testing of an AF-M315E 1-Newton Thruster*, in *Sally McDonnell-Barksdale Honors College*. 2017, University of Mississippi.
22. Mueller, J., *Micropropulsion for Small Spacecraft: Thruster Options for Microspacecraft: A Review and Evaluation of State-of-the-Art and Emerging Technologies*. *Progress in Astronautics and Aeronautics*, ed. P. Zarchan. Vol. 187. 2000: AIAA.
23. Manuela Galati, P.M., *Analysis of Density, Roughness, and Accuracy of the Atomic Diffusion Additive Manufacturing (ADAM) Process for Metal Parts*. *MDPI*, 2019. **12**(4122).
24. David Saltzman, M.B., Stephen Lynch, Timothy W. Simpson, Edward W. Reutzler, Corey Dickman, Richard Martukanitz, *Experimental Comparison of a Traditionally Built versus Additively Manufactured Aircraft Heat Exchanger*, in *55th AIAA Aerospace Sciences Meeting*. 2017, AIAA.
25. M. Santi, I.D., F. Barato, D. Pavarin, *Design and Testing of a 3D Printed 10 N Hydrogen Peroxide Monopropellant Thruster*, in *AIAA Propulsion and Energy 2019 Forum*. 2019, AIAA.
26. Stephen D. Heister, W.E.A., Timothee L. Pourpoint, R. Joseph Cassady, *Rocket Propulsion*. 2019: Cambridge University Press.
27. Nakka, R. *KN-Sorbitol Propellant Chemistry and Performance Characteristics*. 1999 November 13, 1999 2/11/20]; Available from: <http://www.nakka-rocketry.net/sorbchem.html>.
28. R. Vieira, C.P.-H., N. Keller, M.J. Ledoux, *New Carbon Nanofiber/Graphite Felt Composite for Use as a Catalyst Support for Hydrazine Catalytic Decomposition*. *Chemical Communications*, 2002(9): p. 954-955.
29. Kylar J. Moody, A.M.W., Alvin D. Ngo, Seabrook Whyte, Austin Stottlemyre, Kurt P. Rouser, *Development of Sorbitol-Based Solid Rocket Motors for Propulsion Education*, in *AIAA Scitech 2020 Forum*. 2020, AIAA.
30. Kuker, B., *MotorSim 2.0*. 2011.
31. Markforged, *Eiger Software*. 2016.

32. Matt Durkee, C.M., Andrew Quinton, Kathryn Stewart, Lucas Utley, Kurt Rouser, *Design and Test of a Small-Scale, Additively-Manufactured, Liquid-Cooled Rocket Nozzle*, in *AIAA Scitech 2020 Forum*. 2020, AIAA: Orlando, FL.
33. Instruments, N., *LabVIEW 2018*. 2018, National Instruments.
34. Garrett C. Foster, L.J.U., Kurt P. Rouser, *Design and Evaluation of a Portable, Flexible-Use Rocket Thrust Stand*. 2018, Oklahoma State University.

## APPENDICES

### **Nozzle Design Discussion**

This appendix discusses the design approach, iterations, and features of the thruster and nozzle geometry not discussed in full detail in the above text. Some of the overall design choices included:

1. Use of 38mm-diameter solid propellant hardware to align with existing hardware availability and testing equipment.
2. Kosdon-style snap ring hardware that uses internal retaining rings for containing the forward closure and nozzle. This is due to ease of manufacturing avoiding threads, flanges, or complex seals.
3. A minimum nozzle throat size of 0.14in (3.56mm) to fit an ematch igniter through the throat.
4. Minor modification of the motor casing to accommodate the nozzle coolant exit out the side of the casing.

After following the design methodology discussed in Chapter III, some finer details are discussed here. The coolant passage geometry was made to use the same thickness as the wall thickness which was on the lower end of the Metal X printing resolution for wall thicknesses. It was observed that from Durkee et al. that a thinner coolant layer helps to accelerate the coolant flow and maintain a filled layer without air pockets or voids. It was for this reason that the coolant layer was made as thin as possible, hence the 0.05” thick layer.

The wall divider was an arch shape also to accommodate the printer's wall thickness capability. The number of channels was capped at 12 because at the nozzle throat when the cross-sectional size is minimal, the channel walls neared the thickness of the cooling passage. This was strictly a judgement call on the part of the author.

Blends were added to the initial converging section (radius = 0.1in) and at the throat (radius = 0.05in) to assist with smoother exhaust gas flow and minimize stress and thermal concentrations.

Most high-power rocket nozzles utilize a 45° converging half angle and 15° diverging half angle. The 45° is applied to this study's nozzle, but the diverging half angle was reduced to 4° to provide a longer diverging section for the coolant to flow through and distribute the coolant inlet. Any angles less than 4° not only failed to clear the casing edge for supplying coolant, but also would provide insufficient length for the coolant supply hose diameter.

The PVC tubing size was based upon existing availability for tubing and the plastic tank to supply water and the necessary head pressure. These are friction fitted and allow for rapid connection and disconnection with minimal leakage.

Finally, the flat ledge near the throat is to provide the interface with the snap ring.

## Gas Generator Calculations

$$\rho := 0.00182 \frac{\text{kg}}{\text{cm}^3} \quad a := 1.648 \quad p_c := 200$$

$$n := -0.314$$

$$\dot{m} := 0.01 \frac{\text{kg}}{\text{s}}$$

$$r_{200\text{psi}} := a \cdot p_c^n = 0.312 \quad r := 0.312 \frac{\text{in}}{\text{s}} \quad (\text{redefine for units})$$

$$A_{b200\text{psi}} := \frac{\dot{m}}{r \cdot \rho} = 6.933 \times 10^{-4} \text{ m}^2$$

$$A_{b200\text{psi}} = 693.33 \cdot \text{mm}^2 \quad A_{b200\text{psi}} = 1.075 \cdot \text{in}^2$$

$$D_{200\text{psi}} := \left( \frac{A_{b200\text{psi}}}{\frac{\pi}{4}} \right)^{0.5} = 29.712 \cdot \text{mm}$$

necessary propellant diameter

$$D_{200\text{psi}} = 1.17 \cdot \text{in}$$

For AT Casting Tube:  $D := 1.222 \text{in}$

$$L_{20s200\text{psi}} := 20s r = 6.24 \cdot \text{in}$$

$$A_b := \frac{\pi}{4} \cdot D^2 \quad \dot{m}_{\text{new}} := A_b \cdot r \cdot \rho \cdot 10^3 = 10.913 \cdot \frac{\text{kg}}{\text{s}}$$

(grams per second)

About \$4-5 per firing

## Perfect Nozzle Expansion

$$p_{\text{ch}} := 197 \text{psi}$$

$$d_t := 0.122 \text{in} \quad k := 1.042$$

$$p_e := 14.16 \text{psi} \quad \text{Ambient pressure in Stillwater, OK}$$

$$p_e = 0.098 \cdot \text{MPa}$$

$$A_{t\_Ae} := \left( \frac{k+1}{2} \right)^{\frac{1}{k-1}} \cdot \left( \frac{p_e}{p_c} \right)^{\frac{1}{k}} \cdot \sqrt{\frac{k+1}{k-1} \left[ 1 - \left( \frac{p_e}{p_c} \right)^{\frac{k-1}{k}} \right]} = 0.29$$

$$A_{e\_At} := \frac{1}{A_{t\_Ae}} = 3.448$$

$$A_t := \frac{\pi}{4} \cdot d_t^2 = 7.542 \times 10^{-6} \text{ m}^2$$

$$D_e := \sqrt{\frac{4 \cdot A_{e\_At} \cdot A_t}{\pi}} = 5.754 \cdot \text{mm}$$

$$D_e = 0.227 \cdot \text{in}$$

## Temperature Data During Motor Burns

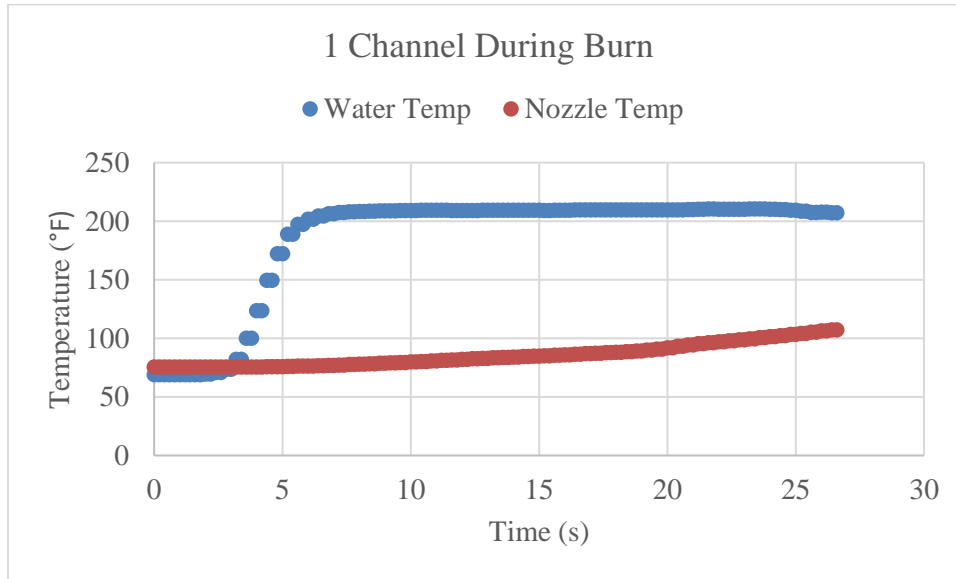


**Figure 55: Temperature data during motor burn - 1 channel**

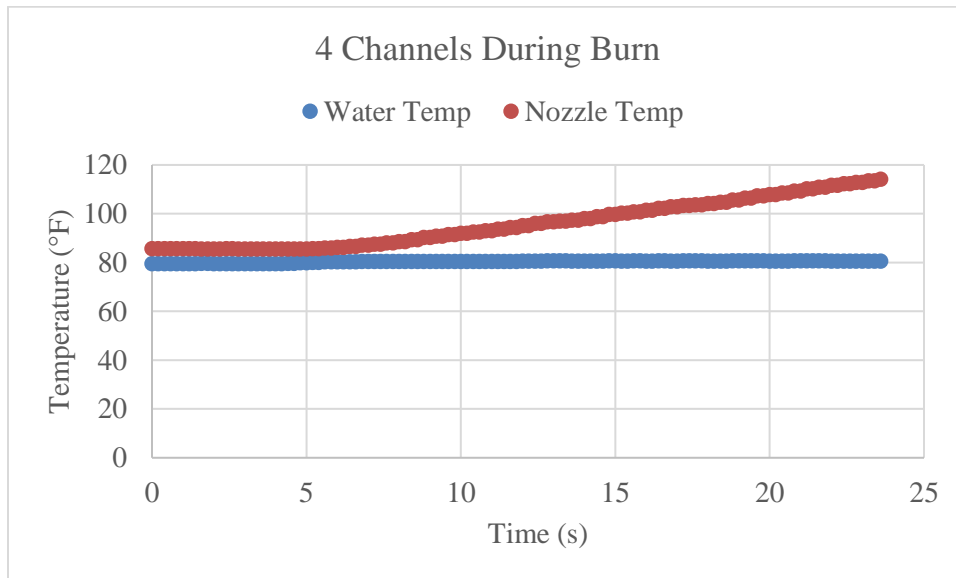


**Figure 56: Temperature data during motor burn - 4 channels**



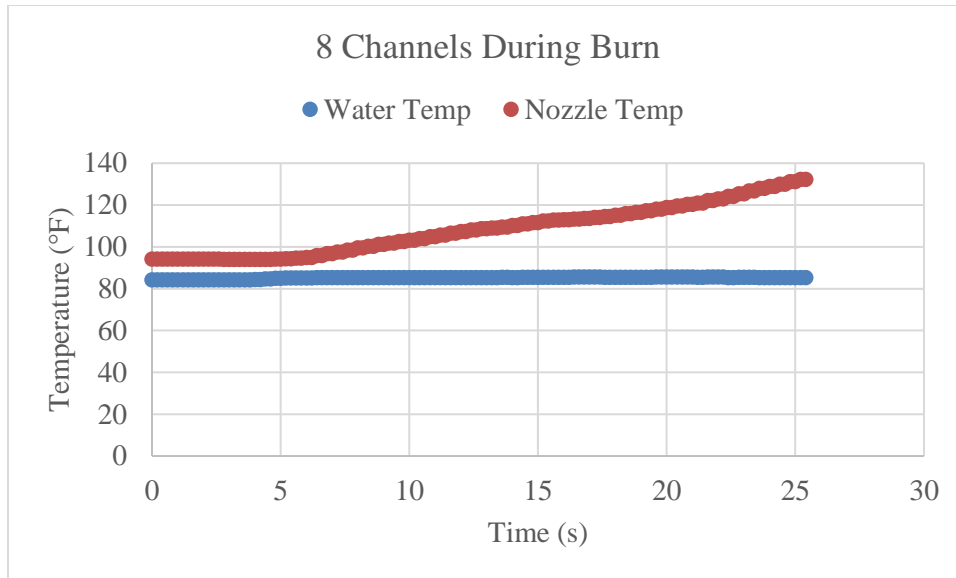


**Figure 57: Temperature data during motor burn - 8 channels**

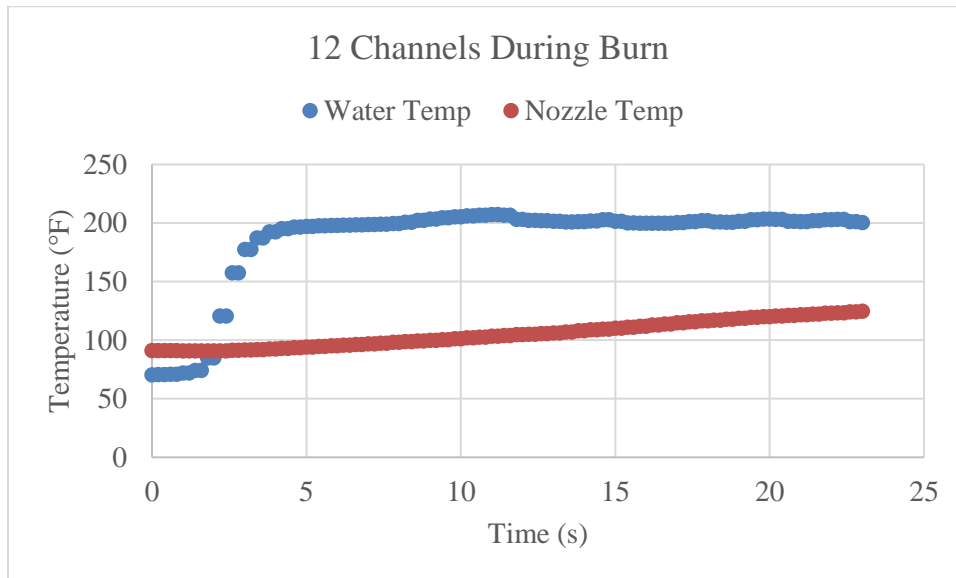


**Figure 58: Temperature data during motor burn - 12 channels**

### Analytical Model Results – 1 Channel

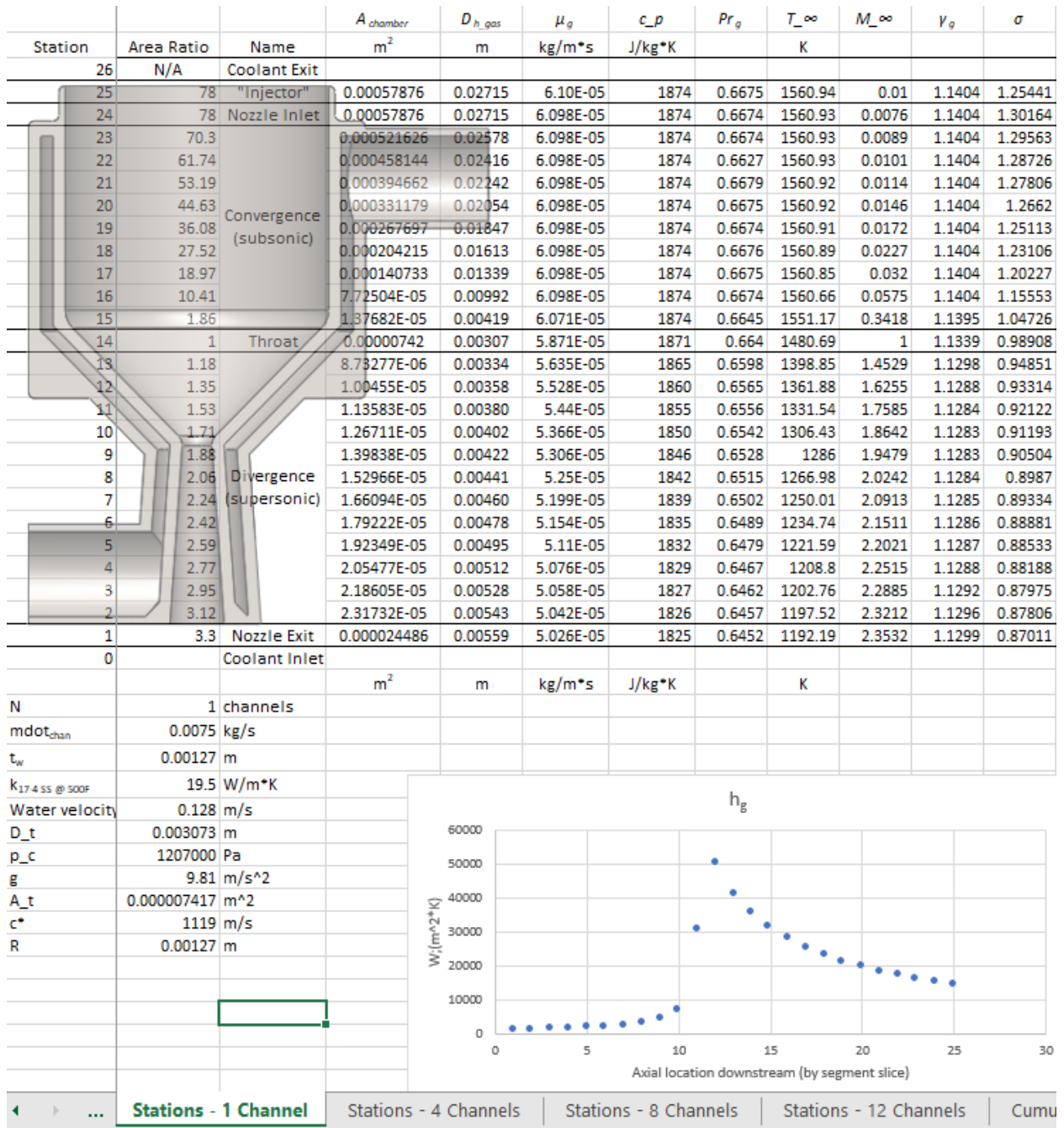


Figure 59: Analytical model - 1 channel part 1

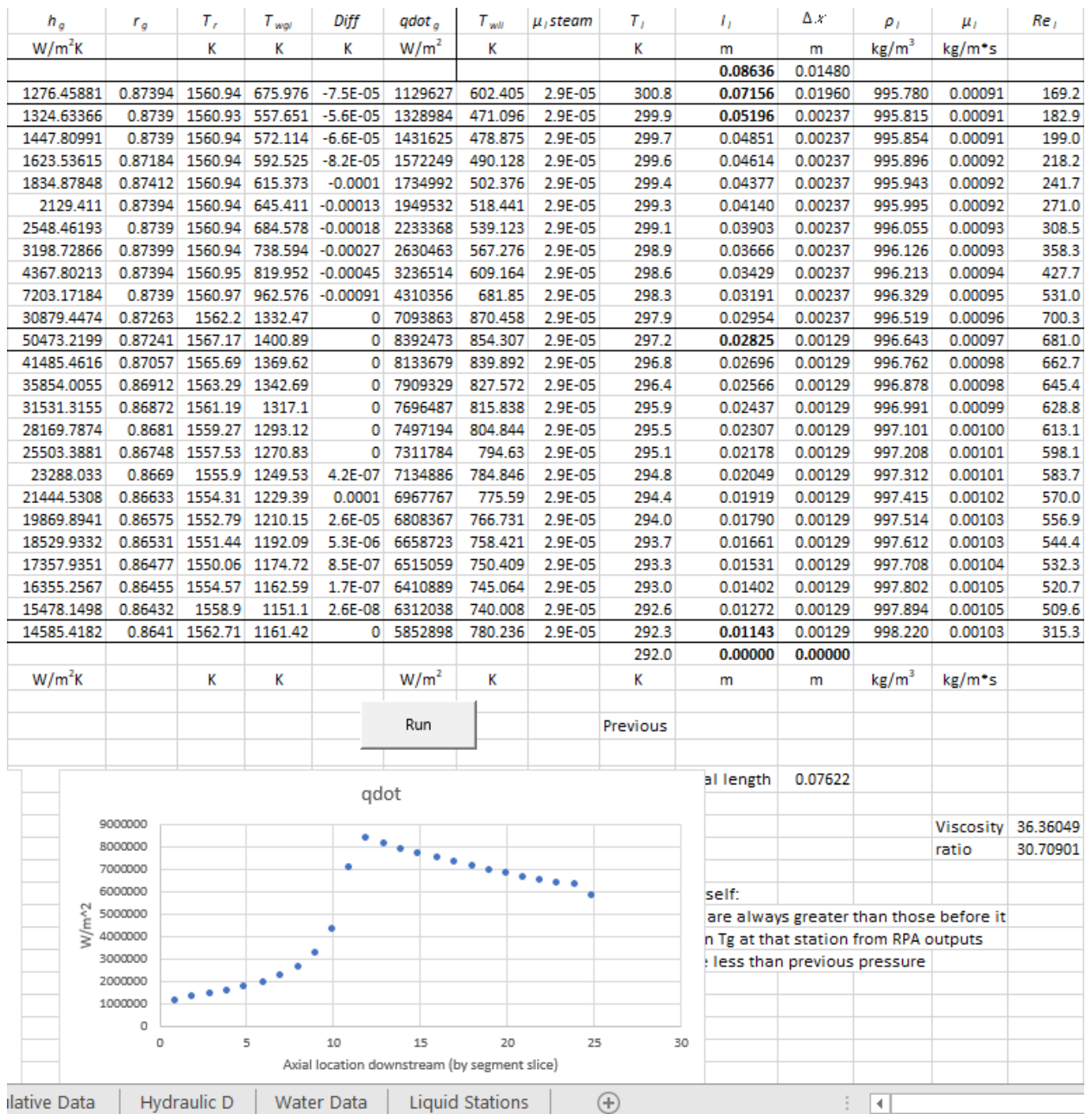


Figure 60: Analytical model - 1 channel part 2

$Pr_i$	$k_i$	$D_h$	$h_i$	$qdot_i$	$c_{p,i}$	$T_{(i+1)}$	$P_i$	$\rho_i$	$\mu_i$	$A_i$	$v_i$	$Re_i$	$c_f$	$P$	$T_m$
	W/m*K	m			J/kg*K	K	Pa	kg/m <sup>3</sup>	kg/m*s	m <sup>2</sup>	m/s			Pa	K
										0.000059					
6.30180	0.60892	0.00254	3733.72	1129627	4182.2	300.755		995.529	0.000891	0.000123979	0.06077	172.537	0.09273	1454.67	639.19
6.32104	0.60871	0.00254	7755.25	1328984	4182.2	299.858	1459.94	995.780	0.000908	0.000123979	0.06075	169.232	0.09454	1459.94	514.373
6.34176	0.60848	0.00254	7985.33	1431625	4182.2	299.731	1460.58	995.815	0.000910	0.000114417	0.06582	182.876	0.08749	1460.58	525.495
6.36452	0.60822	0.00254	8245.25	1572249	4182.3	299.593	1461.29	995.854	0.000913	0.000104856	0.07182	198.97	0.08041	1461.29	541.326
6.38964	0.60794	0.00254	8542.52	1734992	4182.3	299.442	1462.06	995.896	0.000916	9.52937E-05	0.07903	218.235	0.07332	1462.06	558.875
6.41786	0.60763	0.00254	8887.66	1949532	4182.3	299.276	1462.91	995.943	0.000919	8.5732E-05	0.08784	241.723	0.06619	1462.91	581.926
6.45019	0.60727	0.00254	9296.05	2233368	4182.4	299.088	1463.86	995.995	0.000923	7.61702E-05	0.09886	270.996	0.05904	1463.86	611.851
6.48827	0.60684	0.00254	9791.24	2630463	4182.5	298.874	1464.93	996.055	0.000927	6.66084E-05	0.11304	308.508	0.05186	1464.93	652.935
6.53512	0.60632	0.00254	10411.7	3236514	4182.5	298.622	1466.17	996.126	0.000932	5.70466E-05	0.13198	358.324	0.04465	1466.17	714.558
6.59751	0.60563	0.00254	11226.3	4310356	4182.6	298.311	1467.61	996.213	0.000938	4.74848E-05	0.15855	427.712	0.03741	1467.61	822.213
6.70019	0.60448	0.00254	12375	7093863	4182.8	297.897	1469.36	996.329	0.000946	3.7923E-05	0.1985	531.01	0.03013	1469.36	1101.46
6.76648	0.60374	0.00254	15052.9	8392473	4182.9	297.216	1471.57	996.519	0.000959	2.83612E-05	0.26537	700.258	0.02285	1471.57	1127.6
6.83073	0.60303	0.00254	14964.2	8133679	4183.0	296.777	1473.2	996.643	0.000968	2.89066E-05	0.26033	680.991	0.0235	1473.2	1104.76
6.89320	0.60233	0.00254	14877.4	7909329	4183.1	296.351	1474.82	996.762	0.000976	2.94521E-05	0.25548	662.721	0.02414	1474.82	1085.13
6.95398	0.60166	0.00254	14792.3	7696487	4183.2	295.936	1476.42	996.878	0.000984	2.99975E-05	0.2508	645.357	0.02479	1476.42	1066.47
7.01319	0.60100	0.00254	14708.9	7497194	4183.3	295.533	1478	996.991	0.000992	3.05429E-05	0.2463	628.836	0.02544	1478	1048.98
7.07094	0.60035	0.00254	14627.3	7311784	4183.4	295.141	1479.57	997.101	0.000999	3.10883E-05	0.24195	613.095	0.02544	1478	1032.73
7.12729	0.59973	0.00254	14547.3	7134886	4183.5	294.758	1481.12	997.208	0.001007	3.16337E-05	0.23775	598.079	0.02675	1481.12	1017.19
7.18232	0.59911	0.00254	14468.8	6967767	4183.6	294.384	1482.66	997.312	0.001014	3.21791E-05	0.2337	583.739	0.02741	1482.66	1002.49
7.23608	0.59851	0.00254	14391.9	6808367	4183.6	294.019	1484.18	997.415	0.001021	3.27245E-05	0.22978	570.032	0.02807	1484.18	988.439
7.28867	0.59793	0.00254	14316.5	6658723	4183.7	293.663	1485.69	997.514	0.001028	3.32699E-05	0.22599	556.915	0.02873	1485.69	975.257
7.34011	0.59735	0.00254	14242.6	6515059	4183.8	293.314	1487.18	997.612	0.001035	3.38153E-05	0.22232	544.351	0.02939	1487.18	962.566
7.39074	0.59679	0.00254	14170	6410889	4183.9	292.973	1488.65	997.708	0.001042	3.43607E-05	0.21877	532.306	0.03006	1488.65	953.829
7.44058	0.59623	0.00254	14098.8	6312038	4184.0	292.637	1490.12	997.802	0.001048	3.49061E-05	0.21534	520.732	0.03073	1490.12	945.553
7.48680	0.59572	0.002540	11987.9	5852898	4184.0	292.306	1491.57	997.894	0.001054	3.54515E-05	0.212	509.603	0.0314	1491.57	970.83
							1493			0.000059					
	W/m*K	m	W/m <sup>2</sup> K	W/m <sup>2</sup>	J/kg*K	K	Pa	kg/m <sup>3</sup>	kg/m*s	m <sup>2</sup>	m/s			Pa	
Table look		Table lookup		Table lookup		Table look		Table lookup		Table lookup					
						Previous									

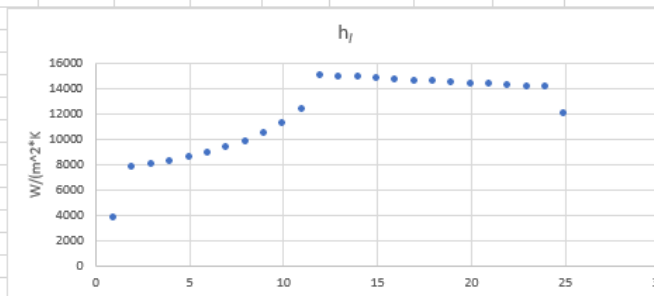


Figure 61: Analytical model - 1 channel part 3

### Analytical Model Results – 4 Channels

Station	Area Ratio	Name	$A_{chamber}$ m <sup>2</sup>	$D_{n, gas}$ m	$\mu_g$ kg/m*s	$c_p$ J/kg*K	$Pr_g$	$T_\infty$ K	$M_\infty$	$\gamma_g$	$\sigma$
26	N/A	Coolant Exit									
25	78	"Injector"	0.00057876	0.02715	6.10E-05	1874	0.6675	1560.94	0.01	1.1404	1.22091
24	78	Nozzle Inlet	0.00057876	0.02715	6.098E-05	1874	0.6674	1560.93	0.0076	1.1404	1.27618
23	70.3	Convergence (subsonic)	0.000521626	0.02578	6.098E-05	1874	0.6674	1560.93	0.0089	1.1404	1.2702
22	61.74		0.000458144	0.02416	6.098E-05	1874	0.6627	1560.93	0.0101	1.1404	1.2618
21	53.19		0.000394662	0.02242	6.098E-05	1874	0.6679	1560.92	0.0114	1.1404	1.25266
20	44.63		0.000331179	0.02054	6.098E-05	1874	0.6675	1560.92	0.0146	1.1404	1.24094
19	36.08		0.000267697	0.01847	6.098E-05	1874	0.6674	1560.91	0.0172	1.1404	1.22618
18	27.52		0.000204215	0.01613	6.098E-05	1874	0.6676	1560.89	0.0227	1.1404	1.20676
17	18.97		0.000140733	0.01339	6.098E-05	1874	0.6675	1560.85	0.032	1.1404	1.17931
16	10.41		7.72504E-05	0.00992	6.098E-05	1874	0.6674	1560.66	0.0575	1.1404	1.13574
15	1.86	1.37682E-05	0.00419	6.071E-05	1874	0.6645	1551.17	0.3418	1.1395	1.03868	
14	1	Throat	0.00000742	0.00307	5.871E-05	1871	0.664	1480.69	1	1.1339	0.98339
13	1.18	Divergence (supersonic)	8.73277E-06	0.00334	5.635E-05	1865	0.6598	1398.85	1.4529	1.1298	0.94184
12	1.35		1.00455E-05	0.00358	5.528E-05	1860	0.6565	1361.88	1.6255	1.1288	0.92569
11	1.53		1.13583E-05	0.00380	5.44E-05	1855	0.6556	1331.54	1.7585	1.1284	0.91304
10	1.71		1.26711E-05	0.00402	5.366E-05	1850	0.6542	1306.43	1.8642	1.1283	0.90307
9	1.88		1.39838E-05	0.00422	5.306E-05	1846	0.6528	1286	1.9479	1.1283	0.89557
8	2.06		1.52966E-05	0.00441	5.25E-05	1842	0.6515	1266.98	2.0242	1.1284	0.88866
7	2.24		1.66094E-05	0.00460	5.199E-05	1839	0.6502	1250.01	2.0913	1.1285	0.88277
6	2.42		1.79222E-05	0.00478	5.154E-05	1835	0.6489	1234.74	2.1511	1.1286	0.87774
5	2.59	1.92349E-05	0.00495	5.11E-05	1832	0.6479	1221.59	2.2021	1.1287	0.87379	
4	2.77	2.05477E-05	0.00512	5.076E-05	1829	0.6467	1208.8	2.2515	1.1288	0.86991	
3	2.95	2.18605E-05	0.00528	5.058E-05	1827	0.6462	1202.76	2.2885	1.1292	0.86736	
2	3.12	2.31732E-05	0.00543	5.042E-05	1826	0.6457	1197.52	2.3212	1.1296	0.86529	
1	3.3	Nozzle Exit	0.000024486	0.00559	5.026E-05	1825	0.6452	1192.19	2.3532	1.1299	0.85364
0		Coolant Inlet									
N	1 channels		m <sup>2</sup>	m	kg/m*s	J/kg*K		K			
mdot <sub>chan</sub>	0.0075 kg/s										
t <sub>w</sub>	0.00127 m										
k <sub>17.4 SS @ 500F</sub>	19.5 W/m*K										
Water velocity	0.128 m/s										
D <sub>t</sub>	0.003073 m										
p <sub>c</sub>	1207000 Pa										
g	9.81 m/s^2										
A <sub>t</sub>	0.000007417 m^2										
c*	1119 m/s										
R	0.00127 m										

Chart Area

Stations - 1 Channel	Stations - 4 Channels	Stations - 8 Channels	Stations - 12 Channels	Cur
----------------------	-----------------------	-----------------------	------------------------	-----

Figure 62: Analytical model - 4 channels part 1



$Pr_i$	$k_i$	$D_h$	$h_i$	$qdot_i$	$c_{p,i}$	$T_{(i+1)}$	$P_i$	$\rho_i$	$\mu_i$	$A_i$	$v_i$	$Re_i$	$c_f$	$P$	$T_m$
	W/m*K	m			J/kg*K	K	Pa	kg/m <sup>3</sup>	kg/m*s	m <sup>2</sup>	m/s			Pa	K
										0.000059					
6.45452	0.60722	0.00949	2443.67	986582	4182.4	299.628		995.844	0.000912	0.000118709	0.06344	657.265	0.02434	1488.99	734.702
6.47221	0.60702	0.00949	5053.72	1221900	4182.4	298.845	1489.4	996.063	0.000928	0.000118709	0.06343	646.503	0.02475	1489.4	580.3
6.49123	0.60681	0.00935	5234.72	1313994	4182.5	298.728	1489.45	996.096	0.000930	0.000109293	0.06889	689.824	0.02319	1489.45	592.406
6.51206	0.60658	0.00920	5438.84	1438939	4182.5	298.602	1489.5	996.131	0.000932	9.98759E-05	0.07538	741.244	0.02159	1489.5	609.889
6.53498	0.60632	0.00906	5671.98	1583272	4182.5	298.464	1489.56	996.170	0.000935	9.04592E-05	0.08323	803.248	0.01992	1489.56	629.009
6.56063	0.60604	0.00891	5942.56	1772149	4182.6	298.312	1489.64	996.213	0.000938	8.10424E-05	0.0929	879.506	0.01819	1489.64	654.063
6.58987	0.60571	0.00877	6262.98	2020221	4182.6	298.142	1489.72	996.260	0.000941	7.16257E-05	0.1051	975.572	0.0164	1489.72	686.3
6.62409	0.60533	0.00862	6652.62	2363960	4182.7	297.948	1489.82	996.315	0.000945	6.22089E-05	0.12101	1100.34	0.01454	1489.82	730.044
6.66580	0.60487	0.00848	7143.99	2881342	4182.7	297.721	1489.93	996.378	0.000949	5.27922E-05	0.14258	1268.98	0.01261	1489.93	794.597
6.72047	0.60426	0.00834	7797.31	3777049	4182.8	297.444	1490.08	996.456	0.000955	4.33754E-05	0.17352	1509.62	0.0106	1490.08	904.482
6.80682	0.60330	0.00819	8742.54	5965638	4183.0	297.082	1490.26	996.557	0.000962	3.39586E-05	0.22162	1880.96	0.00851	1490.26	1173.14
6.86331	0.60267	0.008047	10791.7	7151931	4183.0	296.509	1490.5	996.717	0.000973	2.45419E-05	0.30661	2527.59	0.00633	1490.5	1191.76
6.91826	0.60205	0.00807	10741.1	6958264	4183.1	296.135	1490.69	996.822	0.000980	2.48555E-05	0.30271	2482.95	0.00644	1490.69	1170.18
6.97188	0.60146	0.00808	10691	6788069	4183.2	295.770	1490.88	996.924	0.000987	2.51692E-05	0.2989	2440.1	0.00656	1490.88	1151.39
7.02420	0.60087	0.00810	10641.6	6625507	4183.3	295.415	1491.07	997.024	0.000994	2.54828E-05	0.29519	2398.88	0.00667	1491.07	1133.42
7.07532	0.60030	0.00812	10592.8	6472232	4183.4	295.068	1491.25	997.121	0.001001	2.57965E-05	0.29158	2359.21	0.00678	1491.25	1116.49
7.12530	0.59975	0.00814	10544.6	6328706	4183.5	294.729	1491.43	997.216	0.001007	2.61101E-05	0.28805	2321	0.00689	1491.43	1100.67
7.17419	0.59920	0.00816	10497	6190938	4183.5	294.397	1491.61	997.309	0.001014	2.64238E-05	0.2846	2284.14	0.007	1491.61	1085.46
7.22205	0.59867	0.00818	10450	6059986	4183.6	294.073	1491.79	997.400	0.001020	2.67374E-05	0.28124	2248.57	0.00712	1491.79	1071
7.26891	0.59815	0.00820	10403.5	5934409	4183.7	293.756	1491.97	997.488	0.001026	2.70511E-05	0.27795	2214.23	0.00723	1491.97	1057.12
7.31484	0.59764	0.00822	10357.7	5815932	4183.8	293.445	1492.15	997.575	0.001032	2.73647E-05	0.27474	2181.03	0.00734	1492.15	1044.04
7.35987	0.59713	0.00823	10312.3	5701595	4183.8	293.140	1492.32	997.661	0.001038	2.76784E-05	0.27161	2148.93	0.00745	1492.32	1031.4
7.40425	0.59664	0.00825	10267.5	5620545	4183.9	292.842	1492.49	997.744	0.001044	2.7992E-05	0.26854	2117.87	0.00755	1492.49	1022.98
7.44802	0.59615	0.00827	10223.3	5543202	4184.0	292.547	1492.66	997.827	0.001050	2.83057E-05	0.26554	2087.73	0.00766	1492.66	1014.98
7.48680	0.59572	0.008290	8081.6	4910945	4184.0	292.257	1492.83	997.908	0.001055	2.86193E-05	0.26261	2058.48	0.00777	1492.83	1009.59
							1493			0.000059					
	W/m*K	m	W/m <sup>2</sup> K	W/m <sup>2</sup>	J/kg*K	K	Pa	kg/m <sup>3</sup>	kg/m*s	m <sup>2</sup>	m/s			Pa	
Table loo	Table lookup				Table lookup					Table loo	Table lookup				
							Previous								

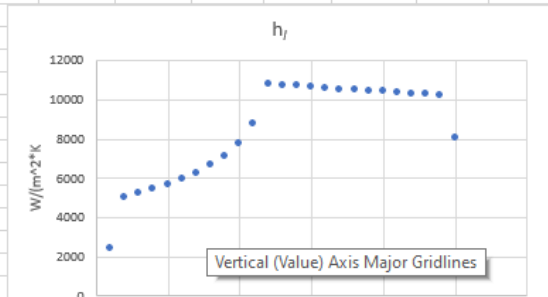


Figure 64: Analytical model - 4 channels part 3

### Analytical Model Results – 8 Channels

Station	Area Ratio	Name	$A_{chamber}$ m <sup>2</sup>	$D_{h, gas}$ m	$\mu_g$ kg/m*s	$c_p$ J/kg*K	$Pr_g$	$T_\infty$ K	$M_\infty$	$\gamma_g$	$\sigma$
26	N/A	Coolant Exit									
25	78	"Injector"	0.00057876	0.02715	6.10E-05	1874	0.6675	1560.94	0.01	1.1404	1.20295
24	78	Nozzle Inlet	0.00057876	0.02715	6.098E-05	1874	0.6674	1560.93	0.0076	1.1404	1.26109
23	70.3	Convergence (subsonic)	0.000521626	0.02578	6.098E-05	1874	0.6674	1560.93	0.0089	1.1404	1.25546
22	61.74		0.000458144	0.02416	6.098E-05	1874	0.6627	1560.93	0.0101	1.1404	1.24741
21	53.19		0.000394662	0.02242	6.098E-05	1874	0.6679	1560.92	0.0114	1.1404	1.23873
20	44.63		0.000331179	0.02054	6.098E-05	1874	0.6675	1560.92	0.0146	1.1404	1.22755
19	36.08		0.000267697	0.01847	6.098E-05	1874	0.6674	1560.91	0.0172	1.1404	1.2135
18	27.52		0.000204215	0.01613	6.098E-05	1874	0.6676	1560.89	0.0227	1.1404	1.19502
17	18.97		0.000140733	0.01339	6.098E-05	1874	0.6675	1560.85	0.032	1.1404	1.16895
16	10.41		7.72504E-05	0.00992	6.098E-05	1874	0.6674	1560.66	0.0575	1.1404	1.12766
15	1.86		1.37682E-05	0.00419	6.071E-05	1874	0.6645	1551.17	0.3418	1.1395	1.03578
14	1	Throat	0.00000742	0.00307	5.871E-05	1871	0.664	1480.69	1	1.1339	0.98165
13	1.18	Divergence (supersonic)	8.73277E-06	0.00334	5.635E-05	1865	0.6598	1398.85	1.4529	1.1298	0.93976
12	1.35		1.00455E-05	0.00358	5.528E-05	1860	0.6565	1361.88	1.6255	1.1288	0.92331
11	1.53		1.13583E-05	0.00380	5.44E-05	1855	0.6556	1331.54	1.7585	1.1284	0.91038
10	1.71		1.26711E-05	0.00402	5.366E-05	1850	0.6542	1306.43	1.8642	1.1283	0.90014
9	1.88		1.39838E-05	0.00422	5.306E-05	1846	0.6528	1286	1.9479	1.1283	0.89237
8	2.06		1.52966E-05	0.00441	5.25E-05	1842	0.6515	1266.98	2.0242	1.1284	0.88521
7	2.24		1.66094E-05	0.00460	5.199E-05	1839	0.6502	1250.01	2.0913	1.1285	0.87907
6	2.42		1.79222E-05	0.00478	5.154E-05	1835	0.6489	1234.74	2.1511	1.1286	0.8738
5	2.59		1.92349E-05	0.00495	5.11E-05	1832	0.6479	1221.59	2.2021	1.1287	0.86963
4	2.77		2.05477E-05	0.00512	5.076E-05	1829	0.6467	1208.8	2.2515	1.1288	0.86552
3	2.95	2.18605E-05	0.00528	5.058E-05	1827	0.6462	1202.76	2.2885	1.1292	0.86275	
2	3.12	2.31732E-05	0.00543	5.042E-05	1826	0.6457	1197.52	2.3212	1.1296	0.86047	
1	3.3	Nozzle Exit	0.000024486	0.00559	5.026E-05	1825	0.6452	1192.19	2.3532	1.1299	0.84691
0		Coolant Inlet									
			m <sup>2</sup>	m	kg/m*s	J/kg*K		K			
N	1	channels									
mdot <sub>chan</sub>	0.0075	kg/s									
t <sub>w</sub>	0.00127	m									
k <sub>17.4 SS @ 500F</sub>	19.5	W/m*K									
Water velocity	0.128	m/s									
D <sub>t</sub>	0.003073	m									
p <sub>c</sub>	1207000	Pa									
g	9.81	m/s <sup>2</sup>									
A <sub>t</sub>	0.000007417	m <sup>2</sup>									
c*	1119	m/s									
R	0.00127	m									

W <sub>i</sub> (m <sup>2</sup> *K)	0	50000
h <sub>g</sub>	0	30

Figure 65: Analytical model - 8 channels part 1





$Pr_i$	$k_i$	$D_h$	$h_i$	$qdot_i$	$c_{p,i}$	$T_{(i+1)}$	$P_i$	$\rho_i$	$\mu_i$	$A_i$	$v_i$	$Re_i$	$c_f$	$P$	$T_m$
	W/m <sup>2</sup> K	m			J/kg*K	K	Pa	kg/m <sup>3</sup>	kg/m*s	m <sup>2</sup>	m/s			Pa	K
										0.000059					
6.51143	0.60659	0.01824	1974.87	909287	4182.5	299.189		995.967	0.000921	0.000117161	0.06427	1267.94	0.01262	1491.36	788.507
6.52820	0.60640	0.01824	4066.23	1158057	4182.5	298.468	1491.47	996.169	0.000935	0.000117161	0.06426	1248.95	0.01281	1491.47	620.867
6.54623	0.60620	0.01768	4237.78	1245390	4182.5	298.357	1491.49	996.200	0.000937	0.000107571	0.06999	1315.36	0.01216	1491.49	632.67
6.56596	0.60598	0.01712	4432.21	1363205	4182.6	298.237	1491.5	996.234	0.000939	9.79817E-05	0.07683	1394.76	0.01147	1491.5	650.066
6.58767	0.60574	0.01656	4655.48	1499565	4182.6	298.106	1491.52	996.270	0.000942	8.83921E-05	0.08517	1491.31	0.01073	1491.52	668.902
6.61195	0.60547	0.01599	4916.2	1677616	4182.6	297.962	1491.54	996.311	0.000945	7.88024E-05	0.09553	1611.25	0.00993	1491.54	693.674
6.63961	0.60516	0.01543	5227.25	1911238	4182.7	297.801	1491.57	996.356	0.000948	6.92128E-05	0.10876	1764.22	0.00907	1491.57	725.486
6.67196	0.60480	0.01487	5609.16	2234524	4182.7	297.618	1491.6	996.407	0.000951	5.96231E-05	0.12624	1966.03	0.00814	1491.6	768.539
6.71133	0.60436	0.01431	6097.41	2720157	4182.8	297.403	1491.65	996.467	0.000956	5.00334E-05	0.15043	2244.53	0.00713	1491.65	831.839
6.76283	0.60379	0.01375	6760.8	3558054	4182.9	297.142	1491.7	996.540	0.000961	4.04438E-05	0.18609	2653.64	0.00603	1491.7	938.942
6.84364	0.60289	0.01318	7759.54	5583068	4183.0	296.801	1491.77	996.636	0.000967	3.08541E-05	0.2439	3313.4	0.00483	1491.77	1197.58
6.89714	0.60229	0.012623	9746.11	6772984	4183.1	296.265	1491.87	996.786	0.000978	2.12645E-05	0.35384	4553.85	0.00351	1491.87	1211.41
6.94919	0.60171	0.01269	9685.53	6591027	4183.2	295.910	1491.96	996.885	0.000985	2.15781E-05	0.34866	4478.39	0.00357	1491.96	1190.7
6.99998	0.60114	0.01275	9625.91	6430260	4183.3	295.565	1492.05	996.982	0.000991	2.18918E-05	0.34363	4406.04	0.00363	1492.05	1172.64
7.04955	0.60059	0.01281	9567.23	6276701	4183.3	295.228	1492.14	997.076	0.000998	2.22054E-05	0.33875	4336.56	0.00369	1492.14	1155.36
7.09798	0.60005	0.01287	9509.47	6131802	4183.4	294.900	1492.22	997.168	0.001004	2.25191E-05	0.334	4269.76	0.00375	1492.22	1139.07
7.14533	0.59952	0.01294	9452.6	5995974	4183.5	294.578	1492.31	997.258	0.001010	2.28327E-05	0.32938	4205.5	0.0038	1492.31	1123.84
7.19165	0.59901	0.01300	9396.61	5865579	4183.6	294.264	1492.39	997.346	0.001016	2.31464E-05	0.32489	4143.6	0.00386	1492.39	1109.19
7.23699	0.59850	0.01306	9341.48	5741550	4183.6	293.957	1492.47	997.432	0.001022	2.346E-05	0.32052	4083.95	0.00392	1492.47	1095.25
7.28140	0.59801	0.01312	9287.18	5622587	4183.7	293.657	1492.55	997.516	0.001028	2.37736E-05	0.31626	4026.42	0.00397	1492.55	1081.87
7.32491	0.59752	0.01319	9233.7	5510260	4183.8	293.362	1492.63	997.599	0.001034	2.40873E-05	0.31212	3970.89	0.00403	1492.63	1069.27
7.36757	0.59705	0.01325	9181.02	5401840	4183.9	293.074	1492.71	997.679	0.001040	2.44009E-05	0.30808	3917.25	0.00408	1492.71	1057.07
7.40961	0.59658	0.01331	9129.13	5324819	4183.9	292.791	1492.78	997.759	0.001045	2.47146E-05	0.30415	3865.4	0.00414	1492.78	1049.19
7.45108	0.59612	0.01337	9078	5251235	4184.0	292.512	1492.86	997.837	0.001050	2.50282E-05	0.30031	3815.16	0.00419	1492.86	1041.7
7.48680	0.59572	0.013437	6879.99	4523425	4184.0	292.237	1492.93	997.914	0.001056	2.53419E-05	0.29657	3766.46	0.00425	1492.93	1096.78
							1493			0.000059					
	W/m <sup>2</sup> K	m	W/m <sup>2</sup> K	W/m <sup>2</sup>	J/kg*K	K	Pa	kg/m <sup>3</sup>	kg/m*s	m <sup>2</sup>	m/s			Pa	
Table loo	Table lookup				Table lookup					Table loo	Table lookup				
							Previous								

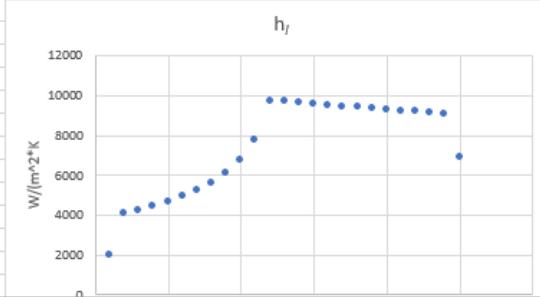


Figure 67: Analytical model - 8 channels part 3

### Analytical Model – 12 Channels

Station	Area Ratio	Name	$A_{chamber}$ m <sup>2</sup>	$D_{h, gas}$ m	$\mu_g$ kg/m*s	$c_p$ J/kg*K	$Pr_g$	$T_\infty$ K	$M_\infty$	$\gamma_g$	$\sigma$
26	N/A	Coolant Exit									
25	78	"Injector"	0.00057876	0.02715	6.10E-05	1874	0.6675	1560.94	0.01	1.1404	1.19367
24	78	Nozzle Inlet	0.00057876	0.02715	6.098E-05	1874	0.6674	1560.93	0.0076	1.1404	1.2528
23	70.3	Convergence (subsonic)	0.000521626	0.02578	6.098E-05	1874	0.6674	1560.93	0.0089	1.1404	1.24754
22	61.74		0.000458144	0.02416	6.098E-05	1874	0.6627	1560.93	0.0101	1.1404	1.23989
21	53.19		0.000394662	0.02242	6.098E-05	1874	0.6679	1560.92	0.0114	1.1404	1.23169
20	44.63		0.000331179	0.02054	6.098E-05	1874	0.6675	1560.92	0.0146	1.1404	1.22107
19	36.08		0.000267697	0.01847	6.098E-05	1874	0.6674	1560.91	0.0172	1.1404	1.20769
18	27.52		0.000204215	0.01613	6.098E-05	1874	0.6676	1560.89	0.0227	1.1404	1.19005
17	18.97		0.000140733	0.01339	6.098E-05	1874	0.6675	1560.85	0.032	1.1404	1.16508
16	10.41		7.72504E-05	0.00992	6.098E-05	1874	0.6674	1560.66	0.0575	1.1404	1.12527
15	1.86		1.37682E-05	0.00419	6.071E-05	1874	0.6645	1551.17	0.3418	1.1395	1.0354
14	1	Throat	0.00000742	0.00307	5.871E-05	1871	0.664	1480.69	1	1.1339	0.98174
13	1.18	Divergence (supersonic)	8.73277E-06	0.00334	5.635E-05	1865	0.6598	1398.85	1.4529	1.1298	0.93982
12	1.35		1.00455E-05	0.00358	5.528E-05	1860	0.6565	1361.88	1.6255	1.1288	0.92335
11	1.53		1.13583E-05	0.00380	5.44E-05	1855	0.6556	1331.54	1.7585	1.1284	0.91037
10	1.71		1.26711E-05	0.00402	5.366E-05	1850	0.6542	1306.43	1.8642	1.1283	0.90009
9	1.88		1.39838E-05	0.00422	5.306E-05	1846	0.6528	1286	1.9479	1.1283	0.89227
8	2.06		1.52966E-05	0.00441	5.25E-05	1842	0.6515	1266.98	2.0242	1.1284	0.88505
7	2.24		1.66094E-05	0.00460	5.199E-05	1839	0.6502	1250.01	2.0913	1.1285	0.87886
6	2.42		1.79222E-05	0.00478	5.154E-05	1835	0.6489	1234.74	2.1511	1.1286	0.87352
5	2.59		1.92349E-05	0.00495	5.11E-05	1832	0.6479	1221.59	2.2021	1.1287	0.86927
4	2.77	2.05477E-05	0.00512	5.076E-05	1829	0.6467	1208.8	2.2515	1.1288	0.8651	
3	2.95	2.18605E-05	0.00528	5.058E-05	1827	0.6462	1202.76	2.2885	1.1292	0.86226	
2	3.12	2.31732E-05	0.00543	5.042E-05	1826	0.6457	1197.52	2.3212	1.1296	0.8599	
1	3.3	Nozzle Exit	0.000024486	0.00559	5.026E-05	1825	0.6452	1192.19	2.3532	1.1299	0.84434
0		Coolant Inlet									
			m <sup>2</sup>	m	kg/m*s	J/kg*K		K			
N	1	channels									
mdot <sub>chan</sub>	0.0075	kg/s									
t <sub>w</sub>	0.00127	m									
k <sub>17.4 SS @ 500F</sub>	19.5	W/m*K									
Water velocity	0.128	m/s									
D <sub>t</sub>	0.003073	m									
p <sub>c</sub>	1207000	Pa									
g	9.81	m/s <sup>2</sup>									
A <sub>t</sub>	0.000007417	m <sup>2</sup>									
c*	1119	m/s									
R	0.00127	m									

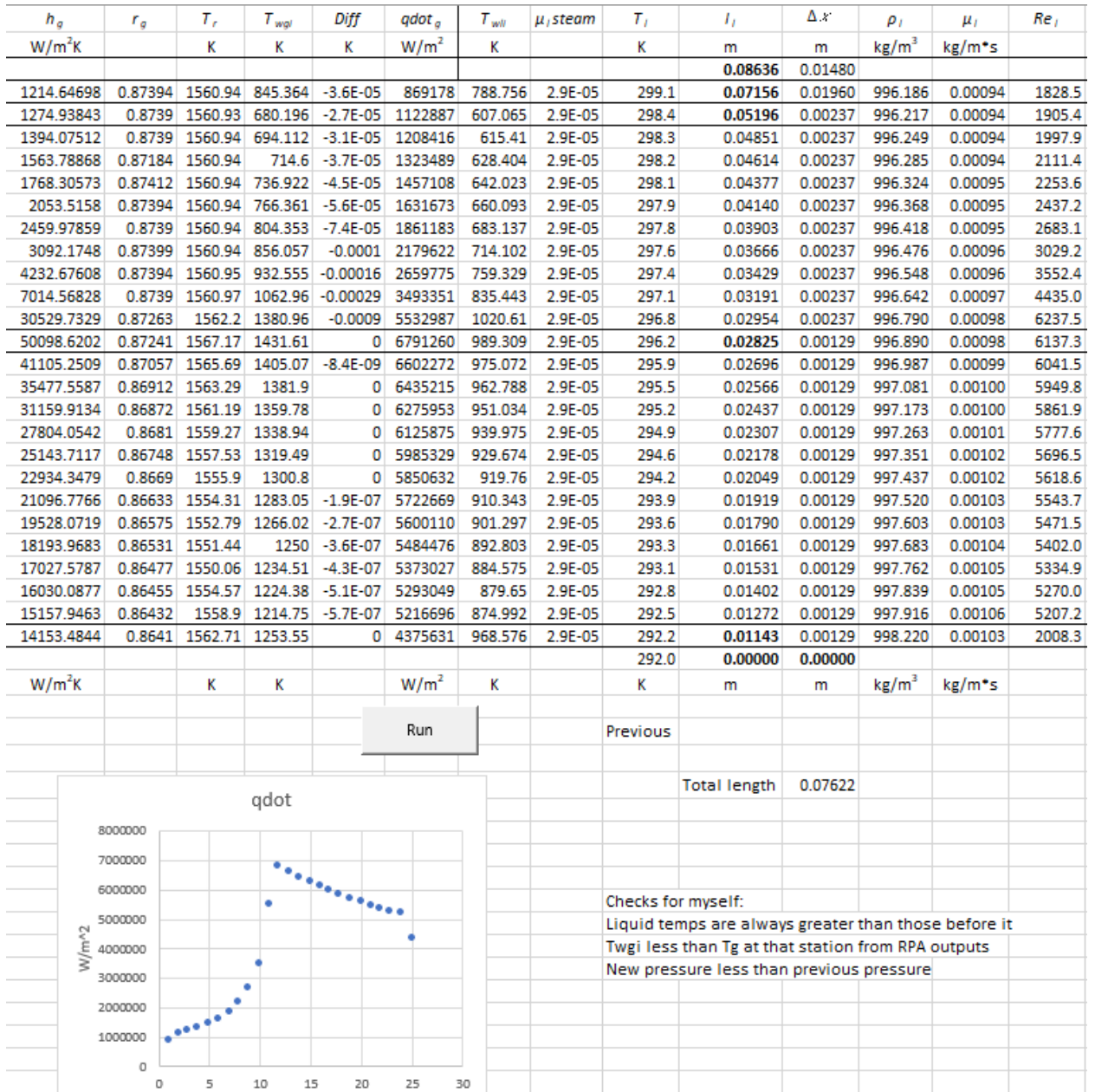
  

Chart Area | e) Axis Major Gridline

Stations - 1 Channel
Stations - 4 Channels
Stations - 8 Channels
Stations - 12 Channels
Cum

Figure 68: Analytical model - 12 channels part 1



**Figure 69: Analytical model - 12 channels part 2**

$Pr_i$	$k_i$	$D_h$	$h_i$	$qdot_i$	$c_{p,i}$	$T_{(i+1)}$	$P_i$	$\rho_i$	$\mu_i$	$A_i$	$v_i$	$Re_i$	$c_{\beta}$	$P$	$T_m$
	W/m <sup>2</sup> K	m			J/kg*K	K	Pa	kg/m <sup>3</sup>	kg/m*s	m <sup>2</sup>	m/s			Pa	K
										0.000059					
6.52082	0.60648	0.02597	1772.57	869178	4182.5	299.095		995.993	0.000923	0.000113806	0.06617	1855.05	0.00863	1491.74	817.06
6.53707	0.60630	0.02597	3636.68	1122887	4182.5	298.406	1491.8	996.186	0.000936	0.000113806	0.06615	1828.53	0.00875	1491.8	643.631
6.55457	0.60611	0.02484	3809.3	1208416	4182.6	298.298	1491.8	996.217	0.000938	0.000104229	0.07223	1905.41	0.0084	1491.8	654.761
6.57373	0.60589	0.02371	4006.34	1323489	4182.6	298.182	1491.81	996.249	0.000940	9.46527E-05	0.07954	1997.94	0.00801	1491.81	671.502
6.59482	0.60566	0.02258	4234.45	1457108	4182.6	298.055	1491.82	996.285	0.000943	8.57076E-05	0.08849	2111.37	0.00758	1491.82	689.473
6.61844	0.60539	0.02145	4503.22	1631673	4182.7	297.915	1491.83	996.324	0.000946	7.54992E-05	0.09971	2253.63	0.0071	1491.83	713.227
6.64538	0.60509	0.02032	4827.25	1861183	4182.7	297.758	1491.85	996.368	0.000949	6.59224E-05	0.11418	2437.21	0.00656	1491.85	743.745
6.67693	0.60474	0.01919	5230.28	2179622	4182.8	297.580	1491.87	996.418	0.000952	5.63457E-05	0.13359	2683.06	0.00596	1491.87	785.08
6.71543	0.60431	0.01806	5754.43	2659775	4182.8	297.371	1491.89	996.476	0.000956	4.67689E-05	0.16093	3029.19	0.00528	1491.89	845.942
6.76599	0.60375	0.01693	6485.22	3493351	4182.9	297.115	1491.93	996.548	0.000961	3.71922E-05	0.20235	3552.43	0.0045	1491.93	949.201
6.84607	0.60286	0.01580	7638.43	5532987	4183.0	296.780	1491.98	996.642	0.000968	2.76154E-05	0.2725	4435	0.00361	1491.98	1200.79
6.89971	0.60226	0.014672	9793.92	6791260	4183.1	296.249	1492.06	996.790	0.000978	1.80387E-05	0.41711	6237.5	0.00257	1492.06	1210.46
6.95186	0.60168	0.01479	9716.01	6602272	4183.2	295.893	1492.14	996.890	0.000985	1.83484E-05	0.41003	6137.31	0.00261	1492.14	1190.07
7.00268	0.60111	0.01490	9639.65	6435215	4183.3	295.547	1492.22	996.987	0.000992	1.8658E-05	0.40319	6041.54	0.00265	1492.22	1172.35
7.05225	0.60056	0.01502	9564.79	6275953	4183.3	295.210	1492.29	997.081	0.000998	1.89677E-05	0.39657	5949.83	0.00269	1492.29	1155.4
7.10063	0.60002	0.01513	9491.38	6125875	4183.4	294.882	1492.36	997.173	0.001004	1.92774E-05	0.39016	5861.92	0.00273	1492.36	1139.46
7.14790	0.59950	0.01525	9419.39	5985329	4183.5	294.561	1492.44	997.263	0.001011	1.95871E-05	0.38396	5777.57	0.00277	1492.44	1124.58
7.19410	0.59898	0.01537	9348.77	5850632	4183.6	294.247	1492.5	997.351	0.001017	1.98967E-05	0.37795	5696.54	0.00281	1492.5	1110.28
7.23929	0.59848	0.01548	9279.47	5722669	4183.6	293.941	1492.57	997.437	0.001023	2.02064E-05	0.37212	5618.65	0.00285	1492.57	1096.7
7.28352	0.59798	0.01560	9211.47	5600110	4183.7	293.641	1492.64	997.520	0.001029	2.05161E-05	0.36648	5543.7	0.00289	1492.64	1083.66
7.32683	0.59750	0.01571	9144.73	5484476	4183.8	293.348	1492.7	997.603	0.001034	2.08258E-05	0.361	5471.53	0.00292	1492.7	1071.4
7.36926	0.59703	0.01583	9079.19	5373027	4183.9	293.061	1492.76	997.683	0.001040	2.11354E-05	0.35568	5401.98	0.00296	1492.76	1059.54
7.41105	0.59656	0.01595	9014.85	5293049	4183.9	292.779	1492.83	997.762	0.001045	2.14451E-05	0.35051	5334.9	0.003	1492.83	1052.01
7.45225	0.59610	0.01606	8951.66	5216696	4184.0	292.502	1492.88	997.839	0.001051	2.17548E-05	0.3455	5270.02	0.00304	1492.88	1044.87
7.48680	0.59572	0.016177	8887.32	5145631	4184.0	292.229	1492.94	997.916	0.001056	2.20645E-05	0.34062	5207.24	0.00307	1492.94	1111.06
							1493			0.000059					
	W/m <sup>2</sup> K	m	W/m <sup>2</sup> K	W/m <sup>2</sup>	J/kg*K	K	Pa	kg/m <sup>3</sup>	kg/m*s	m <sup>2</sup>	m/s			Pa	
Table look		Table lookup		Table lookup		Table look		Table lookup		Table lookup					
						Previous									

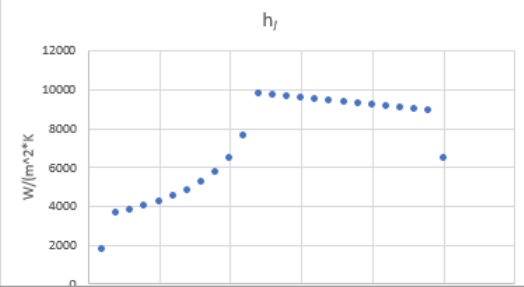


Figure 70: Analytical model - 12 channels part

VITA

Lucas Jay Utley

Candidate for the Degree of

Master of Science

Thesis: COOLANT PASSAGE SEGMENTATION INFLUCENCE ON  
REGENERATIVE COOLING EFFECTIVENESS FOR SMALL SATELLITE  
THRUSTERS

Major Field: Mechanical and Aerospace Engineering

Biographical:

Education:

Completed the requirements for the Master of Science in Mechanical and  
Aerospace Engineering at Oklahoma State University, Stillwater, Oklahoma in  
May, 2020.

Completed the requirements for the Bachelor of Science in Aerospace  
Engineering at Oklahoma State University, Stillwater, Oklahoma in 2018.

Completed the requirements for the Bachelor of Science in Mechanical  
Engineering at Oklahoma State University, Stillwater, Oklahoma in 2018.

Experience:

Graduate Research and Teaching Assistant, Oklahoma State University,  
Stillwater, OK in 2018-2020

Propulsion Research Intern, NASA Marshall Space Flight Center, Huntsville,  
AL in 2018

Engineering Technician Intern, 3M Little Rock, Little Rock, AR in 2016

Professional Memberships:

American Institute of Aeronautics and Astronautics (AIAA)